

2004

Nanotechnology: a systems and control approach

Abu Sebastian
Iowa State University

Follow this and additional works at: <https://lib.dr.iastate.edu/rtd>

 Part of the [Electrical and Electronics Commons](#)

Recommended Citation

Sebastian, Abu, "Nanotechnology: a systems and control approach " (2004). *Retrospective Theses and Dissertations*. 1928.
<https://lib.dr.iastate.edu/rtd/1928>

This Dissertation is brought to you for free and open access by the Iowa State University Capstones, Theses and Dissertations at Iowa State University Digital Repository. It has been accepted for inclusion in Retrospective Theses and Dissertations by an authorized administrator of Iowa State University Digital Repository. For more information, please contact digirep@iastate.edu.

Nanotechnology: A systems and control approach

by

Abu Sebastian

A dissertation submitted to the graduate faculty
in partial fulfillment of the requirements for the degree of
DOCTOR OF PHILOSOPHY

Major: Electrical Engineering (Control Systems)

Program of Study Committee:
Murti V. Salapaka, Major Professor
Degang J. Chen
Nicola Elia
Wolfgang Kliemann
Atul Kelkar
Jason P. Cleveland

Iowa State University

Ames, Iowa

2004

Copyright © Abu Sebastian, 2004. All rights reserved.

UMI Number: 3328093

INFORMATION TO USERS

The quality of this reproduction is dependent upon the quality of the copy submitted. Broken or indistinct print, colored or poor quality illustrations and photographs, print bleed-through, substandard margins, and improper alignment can adversely affect reproduction.

In the unlikely event that the author did not send a complete manuscript and there are missing pages, these will be noted. Also, if unauthorized copyright material had to be removed, a note will indicate the deletion.

UMI[®]

UMI Microform 3328093

Copyright 2008 by ProQuest LLC.

All rights reserved. This microform edition is protected against unauthorized copying under Title 17, United States Code.

ProQuest LLC
789 E. Eisenhower Parkway
PO Box 1346
Ann Arbor, MI 48106-1346

Graduate College
Iowa State University

This is to certify that the Doctoral dissertation of
Abu Sebastian
has met the dissertation requirements of Iowa State University

Signature was redacted for privacy.

Major Professor

Signature was redacted for privacy.

For the Major Program

DEDICATION

*To my parents, Sebastian and Mary Vattamattam and sister Lafia,
for their trust, support, encouragement, and love.*

TABLE OF CONTENTS

LIST OF FIGURES	vii
ACKNOWLEDGMENTS	xvi
ABSTRACT	xix
CHAPTER 1 Introduction	1
PART I: ANALYSIS OF TAPPING MODE AFM DYNAMICS	3
CHAPTER 2 Tapping mode AFM dynamics: A systems approach	5
2.1 Analysis	5
2.1.1 Frequency domain characterization of the nonlinear tip-sample interaction . . .	6
2.1.2 Existence and Stability of Periodic Solutions	9
2.1.3 Apriori bounds on the higher harmonics	12
2.2 Experimental results and discussion	16
2.3 Conclusions	22
CHAPTER 3 Harmonic and power balance tools for the identification of tapping mode AFM dynamics	23
3.1 Analysis	24
3.1.1 Harmonic and power balance tools	24
3.1.2 Cantilever and tip-sample interaction model	27
3.2 Experimental results and discussion	31
3.3 Conclusions	35

CHAPTER 4	The amplitude phase dynamics and fixed points in tapping mode AFM . . .	36
4.1	Analysis	37
4.1.1	Amplitude phase dynamics	38
4.1.2	Steady state behavior	40
4.1.3	Conditions for the stability of fixed points	40
4.2	Experimental results and discussion	42
4.3	Conclusions	46
 PART II: ROBUST BROADBAND NANOPositionING		47
CHAPTER 5	Design methodology for bandwidth and resolution	50
5.1	Device description	51
5.2	Identification	54
5.3	Control design	55
5.4	Characterization of the device	63
5.5	Conclusions	67
CHAPTER 6	Design methodology for robustness	69
6.1	Device description	70
6.2	Identification	71
6.3	Controller design and implementation	73
6.4	Characterization of the device	88
6.5	Conclusions	90
CHAPTER 7	Nanopositioning approach to contact mode AFM imaging	91
7.1	Device description	91
7.2	Formulation of the imaging problem	91
7.3	Control design	94
7.3.1	\mathcal{H}_∞ loop shaping design for robust imaging	95
7.3.2	Robust imaging as a stacked sensitivity problem	97
7.4	Conclusions	101

CHAPTER 8 Conclusion	102
BIBLIOGRAPHY	104

LIST OF FIGURES

Figure 1.1	A typical setup of an AFM. The chief components are the micro-cantilever, a sample positioning system, an optical detection system and a feedback controller.	4
Figure 2.1	The feedback perspective of dynamic mode AFM dynamics. G corresponds to the linear cantilever model. ϕ is a nonlinear model for the tip-sample interaction	6
Figure 2.2	(a) Sector bounds can be used to characterize the attractive regime of the tip-sample interaction. The region of the plot where the interaction forces are positive is not captured by the sector. However in dynamic mode operation at various tip sample separations l , only a part of the tip-sample potential is explored and under several operating conditions the tip can be assumed to be exploring the region captured by the sector (denoted by the shaded region). (b) A simple model was developed for the tip-sample interaction (presented in greater detail in Chapter 3). A negative spring is used to model the attractive forces and a positive spring is used to model the repulsive forces. The tip-sample separation l is defined to be distance between the tip and the beginning of the repulsive spring. The length of the attractive region, d is the separation between the attractive and repulsive springs. The damping in the sample is captured by the dampers.	7
Figure 2.3	The experimentally obtained thermal noise response and the frequency response of the identified model. A two mode approximation is used. The first and the second modal frequencies are at $f_0 = 69.1 \text{ kHz}$ and $f_1 = 403 \text{ kHz}$ respectively. The quality factor of the first mode is estimated to be 56.	17

Figure 2.4	The tip-sample interaction forces acting on the oscillating tip is estimated to be lying in sectors as shown in this figure. As the tip-sample separation reduces, the slope of the sector needed to characterize the nonlinearities increases. The sector slope in (b) is greater than the slope of the sector in (a).	18
Figure 2.5	The condition (2.9) translates to the function $-1 + \text{Re}((G(j\omega)(j\omega\eta + k_{sl}))$ being less than 0 for all ω . A plot of $-1 + \text{Re}((G(j\omega)(j\omega\eta + k_{sl}))$ versus ω is shown in the figure.	18
Figure 2.6	Theoretical upper bounds on the higher harmonics are obtained using an approximate characterization of tip-sample interaction forces for different tip-sample separations.	19
Figure 2.7	This figure depicts the 1st, 2nd, 5th and 6th harmonics of the cantilever oscillation during the approach and retract of the sample towards the tip.	19
Figure 2.8	(a) This figure shows the magnitude of the first seven higher harmonics as the sample approaches the cantilever for different values of tip-sample separation. For reducing tip-sample separations the magnitudes of the higher harmonics increase as the fraction of the period the oscillating tip interacts with the nonlinearity is increasing. This is also captured by the theoretical bounds on the harmonics shown in Figure 2.6. (b) For a tip-sample separation of 40.75 nm , the theoretical bounds on the harmonics are compared with the experimental values obtained.	20
Figure 2.9	The theoretical bounds on the higher harmonics are compared for the cases where the 1st and 2nd mode approximations of the cantilever dynamics are used. The bounds on the harmonics which are close to the 2nd modal frequency are particularly erroneous if only a first mode approximation is used.	21

Figure 2.10	(a) Spectral analysis of the deflection data when the tip is interacting with the repulsive as well as attractive regime of tip-sample interactions distinctly shows the presence of the the first subharmonic and its multiples indicating a $2/f_0$ periodic solution. (b) Theoretical bounds were obtained for the first subharmonic and its multiples except for the first harmonic. The bounds show a similar trend as that observed experimentally.	22
Figure 3.1	The magnitude plots of the Fourier transforms of $p(t)$ and $u(t)$ are shown first. The ratios between $ \hat{p}(jk\omega) $ and $ \hat{u}(jk\omega) $ for $k = 1$ to 10 are then compared with the corresponding points on the frequency response plot of G thus verifying the harmonic balance.	25
Figure 3.2	Model of the cantilever. F is the force on the cantilever due to the sample and b describes the displacement of the base of the cantilever.	27
Figure 3.3	Sketch of a typical cantilever-sample force as a function of position. It indicates long range attractive forces and short range strong repulsive forces. . . .	29
Figure 3.4	Model with the piecewise linear cantilever sample force interaction. When the mass is displaced in the negative direction, first it will encounter the attractive forces modeled by a damper and a negative spring. If the displacement of the mass exceeds l it will encounter repulsive forces modeled by a damper and a positive spring. The dampers account for the energy dissipation due to sample interaction.	30
Figure 3.5	Using the estimated parameter values simulations are performed and the plots thus obtained are compared with those obtained through experiments. In this figure the amplitude is plotted against the separation. There is remarkable agreement between the two plots.	34
Figure 3.6	In this figure, the phase is plotted against the separation ℓ . Here also the two plots show good matching.	34
Figure 3.7	In this figure $\sin \varphi$ is plotted against a/a_0 . It can be seen that the model captures the linearity of this plot and even the reduction in the slope from one.	35

Figure 4.1	(a) The first mode approximation of the cantilever dynamics. m is the mass, k is the spring constant, c is the damper, p is the position of the tip of the cantilever, b is the forcing signal and Φ is the nonlinear tip-sample interaction force which is a function of the position and velocity. (b) Typical tip-sample interaction forces consist of long range weak attractive forces and short range strong repulsive forces. In the model introduced, the oscillating cantilever encounters the tip-sample interaction forces during the negative cycle of its oscillation.	37
Figure 4.2	(a) The amplitude versus tip-sample separation curve is obtained using the interaction model and is compared with that obtained from experiments. There is remarkable agreement between the two. (b) To simplify the analysis, the sample is assumed to be conservative or non-dissipative. The simulation results still agree with the experimental results qualitatively and show the discontinuities.	43
Figure 4.3	For a tip-sample separation of $l = 23 \text{ nm}$, the multi-valued frequency response curve is shown. For a forcing frequency of f_0 , there are three possible fixed point amplitudes. From the stability criteria two of the three are stable. .	44
Figure 4.4	(a)-(e) For different tip-sample separations, the multi-valued frequency response curves are obtained by solving Equation (4.15) (f) The discontinuities in the amplitude versus separation plot can be explained using the multi-valued frequency response plots, the resulting multiple equilibrium amplitudes and their stability	45
Figure 5.1	A schematic block diagram of the device.	51
Figure 5.2	(a) The base plate of the flexure stage. (b) The exploded view of the flexure and evaluation stages.	52
Figure 5.3	A schematic to describe the serpentine design for supporting the flexure stage. This figure is illustrative and not drawn to scale.	52
Figure 5.4	The piezo actuation stage: (a) actuation of a piezo-stack. (b) arrangement of the piezo-stacks.	53

Figure 5.5	The detection stage: (a) working principle of LVDT. (b) demodulation of the amplitude modulated signal.	53
Figure 5.6	A schematic block diagram of the control system	54
Figure 5.7	A schematic block diagram of the closed loop system.	54
Figure 5.8	A comparison of experimentally obtained and simulated frequency responses of the plant.	55
Figure 5.9	The root-locus of the open loop transfer function, G	56
Figure 5.10	The bode plots of closed loop transfer function with different proportional controllers.	57
Figure 5.11	(a) The region in k_i - k_p plane that guarantees closed loop stability. The contour plots showing (b)the phase margins (c) the gain margins (d) the bandwidth of the closed loop systems corresponding to different points in the k_i - k_p plane.	58
Figure 5.12	Tracking of 1 Hz triangular signal with PI controller.	58
Figure 5.13	(a) The generalized plant framework. (b) The closed loop system with regulated outputs.	60
Figure 5.14	The weighting transfer functions	60
Figure 5.15	Closed loop transfer functions: (a)controller (b) sensitivity (c) complementary sensitivity (d) KS	62
Figure 5.16	A comparison of the performance of the closed loop system with (a) PI controller (b) \mathcal{H}_∞ controller.	62
Figure 5.17	Tracking of (a) 25 Hz (b) 50 Hz (c) 100 Hz triangular waves and (d)100 Hz sinusoidal wave using the \mathcal{H}_∞ controller.	63
Figure 5.18	Numerical quantification of hysteresis.	64
Figure 5.19	Hysteresis in (a) the open loop configuration, (b) its elimination in the closed loop configuration.	65
Figure 5.20	The elimination of creep using \mathcal{H}_∞ controller.	65

Figure 5.21	Evaluation stage results: (a),(c) mismatch in the position of grooves between the forward and the backward traverses in the open loop and the corresponding hysteresis cycle. (b),(d) a good match in the closed loop configuration and the corresponding hysteresis cycle.	66
Figure 5.22	(a) The reference (calibration sample) geometry. (b) The mismatch in the position of grooves between the forward and the backward traverses in the open loop. (c) a good match in the closed loop configuration.	66
Figure 5.23	(a) The calibration sample (top) (b) Its distorted image obtained by averaged data in the open loop configuration (bottom-left). (c) Its faithful image obtained by averaging in the closed loop (bottom-right).	67
Figure 6.1	A schematic of the nanopositioning device. There are two stages 'X' and 'Y' with 'X' sitting on top of 'Y'. Each stage is actuated by piezo-electric stacks and the resulting motion is sensed by LVDT sensors.	70
Figure 6.2	u_x is the input to the amplifier which drives the stack piezo. The motion of the stage is sensed using an LVDT sensor whose output is x	71
Figure 6.3	Experimental frequency response is compared with the response of the model $G_{xx}(s)$	72
Figure 6.4	Experimental frequency response is compared with the response of the nominal model $G_{yy}(s)$	73
Figure 6.5	The experimental step response is compared with the response of G_{xx}	74
Figure 6.6	Experimentally obtained frequency responses at different operating regions for the X stage.	75
Figure 6.7	A unity feedback configuration for G_{xx}	75
Figure 6.8	The bode plot of the sensitivity function is shown for a PII controller. The peaks in the magnitude plot indicate lack of robustness.	76
Figure 6.9	This figure shows the tracking of triangular reference signals using K_{pii} . (a) The tracking of a 1 Hz triangular signal is shown. (b) At 5 Hz, oscillatory behavior is observed. (c) This reduces the region of the trajectory which can be used for scanning purposes.	77

Figure 6.10	The shaping controller is denoted by K_s and the robustifying controller is denoted by K_r	79
Figure 6.11	This plot illustrates the reduction in $\ S\ _\infty$ value due to Glover McFarlane robustification.	80
Figure 6.12	(a) The control design can be viewed as shaping of the sensitivity function while satisfying the Bode integral formula. An increase in the gains of the PII controller results in two significant peaks appearing in the plot of $ S(j\omega) $. Without any model information, it is not possible to reduce the two peaks by varying the PII coefficients without compromising on the bandwidth significantly. The robustifying controller with its model information shapes S in such a way that both the peaks are reduced in magnitude at the expense of marginal performance (b) Experimentally obtained $S(j\omega)$ of K_{pvi} before and after robustification.	82
Figure 6.13	Experimentally obtained sensitivity function of an aggressive (high bandwidth) Glover McFarlane design	83
Figure 6.14	(a) Tracking of 5 Hz triangular signals using a Glover McFarlane controller. (b) Tracking of a 10 Hz signal using the Glover McFarlane controller. Except for the turn around regions, the tracking is very good. (c) For the 5 Hz triangular signals, almost 70% of the period is usable in this case.	84
Figure 6.15	a) The weighting function for the sensitivity function. The 40 dB roll off is to approximate a double integral action which enables steady state ramp tracking. b) The weighting function for the complimentary sensitivity function.	85
Figure 6.16	(a) Analytical S and T frequency responses for nominal and robust \mathcal{H}_∞ designs. (b) The experimentally obtained sensitivity and complementary sensitivity functions are compared for nominal and robust \mathcal{H}_∞ designs.	86
Figure 6.17	A schematic of the controller hardware.	87

Figure 6.18 The controllers were split into second order sections (biquads) and each of them was implemented in a direct form II IIR structure depicted above. The computational time for one biquad is $24ns$. $\tilde{b}_1 = b_1/b_0$, $\tilde{b}_2 = b_2/b_0$, $\tilde{a}_1 = -a_1$ and $\tilde{a}_2 = -a_2$ 87

Figure 6.19 The experimentally obtained frequency response of an implemented robust \mathcal{H}_∞ controller is compared with the analytical response. The minor difference in phase is attributed to delay in the circuitry. 88

Figure 6.20 a) LVDT measurement without the controller. b) LVDT measurement while a controller is stabilizing at 0V. 89

Figure 7.1 The principal components of the AFM are a micro-cantilever, an optical detection system, an X-Y sample positioner, a Z positioner and a feedback controller. The Z positioner is moved up and down to maintain a constant cantilever deflection while the sample is being scanned. 92

Figure 7.2 Systems perspective to AFM imaging. $v(t)$ is the output of the optical detector and the disturbance $d(t)$ is the sample profile. The control effort is $u(t)$ and the resulting motion of Z positioner is $z(t)$. The controller is trying to maintain a constant deflection in the presence of the disturbance entering the loop. 92

Figure 7.3 G_{zv} is the transfer function between the input to the Z positioner and the output of the optical detector. \tilde{d} is a scaled version of the sample profile. 93

Figure 7.4 Experimental frequency response of G_{zv} versus that of its model. This figure shows that the fourth order model captures the response accurately 93

Figure 7.5 This figure depicts the design of a Glover McFarlane \mathcal{H}_∞ loop shaping controller for imaging. K_s is an integral controller. A robustifying controller K_r is designed based on the model information. $\tilde{u}(t)$ is found to be a better measure of the sample profile $\tilde{d}(t)$ 95

Figure 7.6 The sensitivity function obtained using the integral controller is compared with that obtained using the Glover McFarlane design. There is remarkable improvement in the bandwidth and robustness. 96

Figure 7.7	This figure compares the transfer functions from the sample profile $\tilde{d}(t)$ to $u(t)$ of the integral controller, $u(t)$ of the Glover McFarlane controller and $\tilde{u}(t)$ of the Glover McFarlane controller. It is evident that the normalized transfer function between $\tilde{d}(t)$ and $\tilde{u}(t)$ is closer to unity which is needed for a faithful observation of $\tilde{d}(t)$	97
Figure 7.8	A calibration sample with triangular grooves of depth 250 nm and width 2 μm is imaged using the integral controller, K_i . There is significant error between the trace and retrace signals.	97
Figure 7.9	Imaging is done using the Glover McFarlane controller using $u(t)$ to observe the profile. There is an improvement in the quality of imaging compared to the integral controller.	98
Figure 7.10	Imaging is done using the Glover McFarlane controller using $\tilde{u}(t)$ to observe the profile. There is a significant improvement in the quality of imaging over both the integral controller and the case where $u(t)$ is used to observe the profile.	99
Figure 7.11	Weighting functions W_S , W_U and W_T are used to specify the requirements of imaging. This is followed by designing a stabilizing controller such that the \mathcal{H}_∞ norm of the operator between $v_r(t)$ and $z(t)$ is less than one.	99
Figure 7.12	The stacked \mathcal{H}_∞ controller K_∞ is split into two, $K_{1\infty}$ and $K_{2\infty}$ such that $K_{1\infty}$ resembles an integrator and $K_{2\infty}$ resembles an inverse of the plant G_{zv}	100
Figure 7.13	Imaging of the 2 μm grating is done using the \mathcal{H}_∞ controller K_∞ . The sample profile is estimated using $\tilde{u}(t)$	100
Figure 7.14	This figure compares the deflection signals for K_i , $K_s K_r$ and K_∞ while imaging. The error is significantly lower than that of K_i for both the Glover McFarlane and \mathcal{H}_∞ controllers.	101

ACKNOWLEDGMENTS

Many times I have tried to fathom the rationale behind why certain things happen the way they would. I must admit there is very little success in this respect. How did I end up being an undergrad in a school which in spite of its stellar reputation I came to know a mere weeks before the deadline for application? Why did I choose to major in engineering, a discipline I was the least aware of, growing up as a child? How did I end up spending more than five years in a small midwestern town even unknown to most Americans? In hindsight it looks like everything was for the good. Sure there were bumps in this ride. But nevertheless it was a pleasurable ride overall. I would like to thank that supreme power that continues to influence my life and work in a big way.

Life as a graduate student is intertwined in a big way with that of his advisor. It is all the more true if the graduate student is his first student. I was very fortunate to have Prof. Murti V. Salapaka as my advisor and mentor. He has varied interests which transcend the boundaries of control theory and he provides his students with the same latitude in research. I would like to thank him for the tremendous influence he had on me as a researcher and as a person.

I was also fortunate to have had other remarkable teachers like Prof. Mustafa Khammash, Prof. Nicola Elia, Prof. Timo Seppalainen and Prof. Bruce Wagner. Even though I could not take classes with Prof. Degang Chen, I had the pleasure of interacting with him a lot during my research on the Atomic Force Microscope dynamics. I would like to thank all of them for guiding me through the beautiful path of control theory and mathematics.

Dr. Jason Cleveland of *Asylum Research Inc.* has influenced me significantly as an outstanding researcher and as a brilliant experimentalist. I would like to thank him and his colleagues at *Asylum Research Inc.* for all the support.

I would like to particularly thank Prof. Wolfgang Kliemann and Prof. Atul Kelkar for being in my committee along with Prof. Salapaka, Prof. Chen, Prof. Elia and Dr. Cleveland.

I had the pleasure of having some terrific classmates and labmates. I would like to thank Hana El-Samad for her four long years of constant companionship. I would also like to thank Anil Gannepalli, Rajeev Rajaram, Deepak R. Sahoo, Tathagata De, Vikas Yadav and Hullas Sehgal. It is a pity Anil joined us only in the last two years of my PhD life. It was great being with him. Not to mention the calories I have lost climbing the steps instead of taking the elevator. Rajeev was my classmate from undergrad and even though we lost him to mathematics in the latter half of my stay at Ames, I did benefit a lot from our group study sessions. Deepak brought in a fresh boyish charm to the group and we had a very fruitful collaboration in the shape of a new transient signal based detection scheme for the AFM. It is pity I had to leave the group when Tatha and I were about to make some contributions in the biological front. Even though short, it was fun working with him. Vikas is a fun guy to be around with. If we do not lose him to Bollywood as a film producer I am sure he will make some outstanding scientific contributions in the near future. Hullas brings in a lot of fun and energy to the group. And ya I do love those arguments on cricket and IITians. I hope you win that much awaited Nobel prize with the optical tweezer. I would like to thank the rest of the control group, most notably Jialing Liu, Jinhua Jin, Jeff Eisenbeis, Xuezheng Wang, Xin Qi and Lin Zhe for all the support and encouragement. I particularly remember those interesting discussions on various topics which vary from control theory to Chinese foreign policy and German American history.

Five years is a long time to be confined just to the Lab. I would like to name all the friends I have made in these many years but due to space limitations let me focus on a few, first my roommates. My BITS Pilani stay was effectively prolonged by two more years by my roommates of the first two years. My BITSian batchmates, Arun Raghavan, Anil Kurian and Nishikant Reddy. It was fun filled two years where I still felt like an undergrad. Their graduation did leave a huge dent but I cannot complain much about the replacements I got. Murari, Nagaraj and Murali. Murari made sure the house enthu level never falls, Nagaraj brought in the spiritual element and Murali brought in the color (literally!). My stay at Preeti Seema with Pallab (Sethji) and Rakesh (Paji) was equally enjoyable. I would like to thank all of them for making my stay in Ames such a wonderful experience.

I would like to thank my friends from Chemical Engineering and Sankalp for all the nice Friday night parties and beer sessions (inevitably followed by philosophical and theological discussions). The post Sunday mass sessions with the *Keralights* was a lot of fun. The *Psycho* gang spearheaded by my

undergrad buddy Lux was another frequent refuge for me.

Finally I would like to thank my parents Sebastian and Mary Vattamattam and to my little sister Lafia for all the love, concern and constant support. To them I dedicate this thesis.

ABSTRACT

Recent years have seen significant advances in the fields of nanosciences and nanotechnology. A significant part of the research in nanotechnology deals with developing tools and devices to probe and manipulate matter at the atomic, molecular and macro-molecular levels. Surprisingly in spite of the potential for engineers to contribute substantially to this area, most of the contributions till date have come from physicists and biologists. Engineering ideas primarily from systems theory and control significantly complement the physical studies performed in this area of research. This thesis demonstrates this by the application of systems ideas and tools to address two of the most important goals of nanotechnology, interrogation and positioning of materials at the nanoscale. The atomic force microscope (AFM), a micro-cantilever based device is one of the foremost tools in the interrogation and manipulation of matter at the atomic scale. The AFM operating in the most common tapping-mode has a highly complex dynamics due to the nonlinear tip-sample interaction forces. A systems approach is proposed to analyze the tapping-mode dynamics. The systems perspective is further exploited to develop analytical tools for modeling and identifying tip sample interactions. Some of the distinctly nonlinear features of tapping-mode operation are explained using the asymptotic theory of weakly nonlinear oscillators developed by Bogoliubov and Mitropolski. In the nanopositioning front, through the design and implementation of nanopositioning devices, a new paradigm for the systematic design of nanopositioners with specific bandwidth, resolution and robustness requirements is presented. Many tools from modern robust control like nominal and robust \mathcal{H}_∞ designs and Glover McFarlane designs are exploited for this. The experimental results demonstrate the efficacy of these design schemes.

CHAPTER 1 Introduction

Systems ideas and control theory have a significant role to play in the technological revolution that is underway in the fields of nanosciences and nanotechnology. This thesis demonstrates this through the design and analysis of nanoscale devices based on systems concepts.

The recent advances in nanotechnology warrant devices which can probe nature at the atomic and molecular scales. Micro-cantilever based devices have contributed significantly to the control, manipulation and interrogation of matter at the nanoscale. Micro-cantilevers have been utilized in biological sciences in a variety of applications like sensing sequence-specific DNA [1], studying cell-cell interactions [2] and antigen/antibody interactions [3]. Another intriguing application is in the detection of single electron spin ([4, 5, 6]). Such research has significant ramifications for quantum computing technology and to the physics at atomic scales. Researchers at IBM are exploring the usefulness of micro-cantilevers in high density data storage ([7]). In spite of the vast underlying promise, considerable challenges need to be overcome to fully harness the potential of this technology. A key element of the micro-cantilever based technique is the manner in which the cantilever interacts with the matter it is investigating or manipulating. Although micro-cantilever based devices have been utilized ubiquitously in various applications, the dynamics of the cantilever-sample interaction is significantly complex and considerable research effort is being placed at deciphering this interaction. Most of the research effort is towards developing sophisticated and often involved physical models of the tip-sample interaction ([8], [9], [10]). This has helped provide insights into the various physical sources of the tip-sample interaction force. However these approaches do not lend themselves towards isolating the principal characteristics and limitations of micro-cantilever based devices. A systems based approach significantly complements the physical studies performed on the tip-sample interaction, provides new ways of interpreting data and indicates the fundamental limitations of micro-cantilever based devices. Further exploitation of the systems viewpoint has recently led to the development of certain new modes

of imaging (see [11], [12] and [13]). The Atomic Force Microscope (AFM) is arguably the foremost micro-cantilever based device used to manipulate and probe matter at the nanoscale. The AFM is so powerful primarily because of its versatility. Unlike other scanning probe techniques like the Scanning Tunnelling Microscope, the AFM can interrogate non-conducting samples in its natural environment making it particularly suitable for biological applications. In Chapter 2 the systems approach to the analysis of AFM dynamics is introduced. An identification scheme for tip-sample interaction forces based on these ideas is presented in Chapter 3. To explain some of the distinctly nonlinear features of the dynamic mode operation of the AFM, asymptotic theory developed by Bogoliubov and Mitropolski is employed. This is presented in Chapter 4.

Another pivotal requirement for harnessing the vast potential of nanotechnology is ultra-fast positioning. For high throughput high bandwidth positioning is imperative. Also in many applications, it is necessary to have fast positioning capability. For example, in the field of cell biology, attractive proposals on using nanotechnology have been presented where nano-probes track events in the cell. These events often have time-scales in the micro-second or nano-second regimes. Moreover precise positioning is needed while probing and manipulating samples at molecular and atomic scales. Scanners for high density data storage devices present another set of applications where high bandwidth, high resolution nanopositioners are needed. Current nanopositioning technology does not meet the needed high precision and bandwidth requirements. The modern robust control paradigm offers a powerful tool to address the challenges of broadband nanopositioning. We present a new paradigm for the systematic design of controllers for nanopositioning based on bandwidth, resolution and robustness demands. It consists of two design methodologies. A design for bandwidth and resolution and a design for robustness. In Chapters 5 and 6 we demonstrate this paradigm through the design and implementation of nanopositioning devices. The contact mode imaging problem in the Atomic Force Microscope can be viewed as a nanopositioning problem where the cantilever serves as the position sensor. In Chapter 7, the paradigm presented in Chapters 5 and 6 is applied to this specific problem.

PART I: ANALYSIS OF TAPPING MODE AFM DYNAMICS

In the first part of the thesis, systems concepts are used to analyze the dynamics of the Atomic Force Microscope (AFM). This analysis significantly complements the physical studies performed on the operation of the AFM and leads to a better understanding of the salient features and limitations of this instrument. A brief introduction to the operation of this device is provided next.

The schematic of a typical AFM is shown in Figure 1.1. It consists of a micro-cantilever, a sample positioning system, a detection system and a control system. The micro-cantilever is the most important component of the AFM. A typical cantilever is $100 - 200 \mu m$ long, $5 - 10 \mu m$ wide and has a tip of diameter of approximately $5 nm$. Most of the cantilevers are micro-fabricated from silicon oxide, silicon nitride or pure silicon using photolithographic techniques. The cantilever deflects under the influence of the sample and other forces. This deflection is registered by the laser incident on the cantilever tip which reflects into a split photodiode. This setup constitutes the detection system. The minimum detectable cantilever deflection is in the order of $0.1 nm$. Using the measured deflection signal, the control system moves the sample appropriately to achieve necessary objectives. Sample positioning is usually provided by a piezoelectric based positioning stage.

Since its invention in 1986 ([14]) a wide range of modes of operations have emerged. In contact mode or static mode operation, the cantilever deflection is primarily due to the tip-sample interaction. The deflection of the tip is used to interpret sample properties. In the contact mode operation, the tip moves over a short range of tip-sample interaction making linear approximations valid for analysis. In the tapping-mode or dynamic mode operation, the cantilever support is forced sinusoidally using a dither piezo. The changes in the oscillations introduced due to the sample are interpreted to obtain the sample properties [15]. The tapping-mode operation is the most common method of imaging primarily because it is less invasive on the sample and has higher signal to noise ratio. In this mode, due to the cantilever oscillation the tip moves over a long range of highly nonlinear tip-sample potential leading to

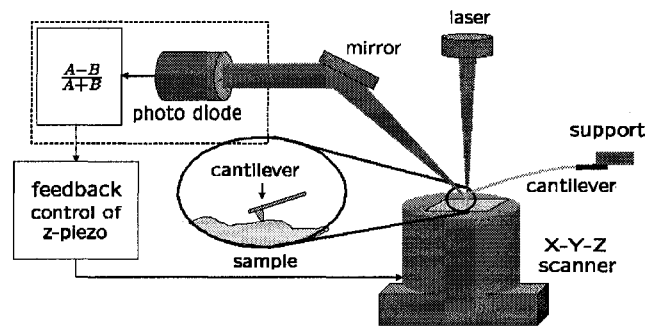


Figure 1.1 A typical setup of an AFM. The chief components are the micro-cantilever, a sample positioning system, an optical detection system and a feedback controller.

complex behavior. The complexity of the dynamics can be assessed by the experimental and theoretical studies that confirm the existence of chaotic behavior (see [16], [17] and [18]). However under normal operating conditions the cantilever is found to evolve into a stable periodic orbit with a period equal to the period of forcing. It is also experimentally observed that when the tip-sample separation is sufficiently large, the periodic orbit is near sinusoidal.

Much of the research on tapping-mode dynamics has revolved around solving nonlinear differential equations numerically (see [8] and [9]). As mentioned earlier even though they predict experimentally observed behavior, they fail to capture the limitations and important characteristics in the operation of tapping-mode AFM. Also the identification of model parameters is not straightforward due to their complexity. In Chapter 2, a systems approach to the analysis of AFM dynamics is presented. A frequency domain characterization of the nonlinear tip-sample interaction is presented, conditions are derived for the existence and stability of periodic solutions and bounds are obtained for the higher harmonics. Chapter 3 discusses harmonic and power balance tools developed to analyze the AFM dynamics and their use in identifying tip-sample interaction forces. In Chapter 4 some of the distinctly nonlinear features in the tapping-mode operation of the AFM are explained using averaging techniques and the amplitude phase dynamical equations are derived. Parts of the work presented in these chapters have appeared in [19], [20], [21], [22] and [23].

CHAPTER 2 Tapping mode AFM dynamics: A systems approach

As mentioned earlier, in the tapping mode operation of the AFM, the tip moves over a long range of tip-sample potential making a linear model of the interaction inadequate. Under these circumstances, the questions on the existence and stability of periodic solutions are very relevant. Moreover it is experimentally observed that when the tip-sample offset is relatively large, the periodic solution is almost sinusoidal. Thus along with the existence and stability, the questions on the near sinusoidal nature of the periodic solution become important. In this chapter a systems perspective is developed for the analysis of tapping mode dynamics. The subsequent analysis exploits a generalized frequency domain characterization of the nonlinear tip-sample interaction. This along with the frequency response of the cantilever is used to derive conditions for the existence and stability of periodic solutions. Bounds are obtained on the higher harmonics and the smallness of these bounds compared to the first harmonic proves the near sinusoidal nature of the periodic solutions. The conclusion reached is that point mass models are appropriate as the higher harmonics are small. This work provides important framework to assess the bounds on the higher harmonics and thereby provides a foundation to study the the fundamental limitations on what can be assessed using the dynamic-mode AFM. The experimental results are presented in Section 2.2.

2.1 Analysis

In the dynamic mode, the cantilever can be imagined to be a system that takes in as input the sum of the external forcing signal, $g(t)$ and the tip-sample interaction force, $h(t) = \phi(p(t))$. It produces the deflection signal, $p(t)$ as the output (see Figure 2.1). The forcing g is assumed to be sinusoidal with period T . The tip-sample interaction force now appears as a feedback block. In this perspective the instantaneous tip position is fed back to the cantilever system G through the tip-sample interaction system ϕ . In this way we view the AFM dynamics as an inter-connection of two systems, the system

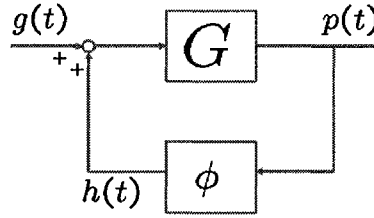


Figure 2.1 The feedback perspective of dynamic mode AFM dynamics. G corresponds to the linear cantilever model. ϕ is a nonlinear model for the tip-sample interaction

G that models the cantilever and the block ϕ that models the sample.

2.1.1 Frequency domain characterization of the nonlinear tip-sample interaction

Frequency domain characterizations of a system describe the manner in which the system maps the input frequency components to that of the output. They specify those frequency components of the input which get amplified and attenuated. Moreover they are measures of the input-output energy distribution over the frequencies. For a linear system like the cantilever, G , the frequency response, $G(j\omega)$ completely characterizes the input-output behavior. For such linear devices, a sinusoid of a certain frequency produces a sinusoid of the same frequency and there is no distribution of a certain frequency sinusoid to other frequencies. However a nonlinear system does distribute energy in a particular input frequency over other frequencies.

The tip-sample interaction being nonlinear does not admit a precise frequency domain characterization. However it is possible to obtain approximate frequency domain characterization for the nonlinear tip-sample interaction.

In a typical experimental scenario, it is possible to assume that the tip-sample interaction forces lie in a *sector*. In Figure 2.2(a) the characterization of the attractive interaction forces in terms of an appropriate sector is depicted. The tip-sample interaction force is assumed to lie in a sector $[0 \ b]$ if,

$$0 \leq p\phi(p) \leq bp^2 \quad (2.1)$$

for all p . Note that this is a rough characterization of the nonlinearities and a detailed understanding of the interaction forces is not necessary and typically not available. Such a characterization can be

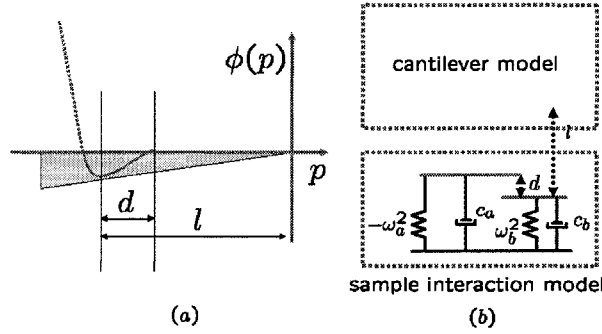


Figure 2.2 (a) Sector bounds can be used to characterize the attractive regime of the tip-sample interaction. The region of the plot where the interaction forces are positive is not captured by the sector. However in dynamic mode operation at various tip sample separations l , only a part of the tip-sample potential is explored and under several operating conditions the tip can be assumed to be exploring the region captured by the sector (denoted by the shaded region). (b) A simple model was developed for the tip-sample interaction (presented in greater detail in Chapter 3). A negative spring is used to model the attractive forces and a positive spring is used to model the repulsive forces. The tip-sample separation l is defined to be distance between the tip and the beginning of the repulsive spring. The length of the attractive region, d is the separation between the attractive and repulsive springs. The damping in the sample is captured by the dampers.

obtained by static force curve data. Thus the subsequent analysis holds for *any* nonlinearity in the sector. This provides robustness to the results obtained.

Knowing the sector bounds it is possible to obtain an approximate frequency domain characterization of the tip-sample interaction forces. In other words it is possible to partially describe ϕ in terms of how the nonlinearity distributes the input signal's energy over the various frequencies. For example, for a nonlinearity satisfying the sector condition $(bp - \phi(p))\phi(p) \geq 0$ (from (2.1)), it follows that,

$$\int_0^\infty (bp\phi(p) - \phi(p)^2) dt \geq 0.$$

Equivalently in the frequency domain,

$$\int_{-\infty}^\infty (b\hat{p}^* \widehat{\phi(p)} - \widehat{\phi(p)}^* \hat{\phi(p)}) d\omega \geq 0, \quad (2.2)$$

where \hat{x} denotes the Fourier transform of x . The inequality (2.2) can be written as,

$$\int_{-\infty}^{\infty} \begin{pmatrix} \hat{p}(j\omega) \\ \widehat{\phi(p)}(j\omega) \end{pmatrix}^* \Pi_c(j\omega) \begin{pmatrix} \hat{p}(j\omega) \\ \widehat{\phi(p)}(j\omega) \end{pmatrix} d\omega \geq 0 \quad (2.3)$$

where,

$$\Pi_c(j\omega) = \begin{bmatrix} 0 & b \\ b & -2 \end{bmatrix}. \quad (2.4)$$

The tip-sample interaction forces are then said to satisfy the Frequency Condition (FC) (also known the *Integral Quadratic Constraint* in systems theory) defined by Π_c . Π_c is known as the Circle FC. Note that (2.3) intricately links the input frequency component $\hat{p}(j\omega)$ to the output frequency component $\widehat{\phi(p)}(j\omega)$ of the nonlinearity ϕ . Such a relationship is the counterpart to the cantilever frequency response relationship $p(j\omega) = G(j\omega)u(j\omega)$ where u and p are the input and the output respectively of the cantilever characterization $G(j\omega)$.

More sophisticated frequency domain characterizations can be derived for the sector nonlinearity (see Ref. [24]). A more involved understanding of the tip-sample interactions, if known could lead to a better frequency domain characterization of the nonlinear tip-sample interactions. In other words a bigger class of FCs will be satisfied by ϕ . Indeed it can be shown that the FC defined by,

$$\Pi_p = \begin{pmatrix} 0 & b + j\eta\omega \\ b - j\eta\omega & -2 \end{pmatrix} \quad (2.5)$$

for different values of η are satisfied by the tip-sample interactions satisfying the sector condition (2.1). These FCs are called the Popov FCs. Note that for $\eta = 0$, the Popov FC reduces to a Circle FC.

The stability analysis of the interconnection between the two blocks, the cantilever and the tip-sample interaction depends on how they dissipate and generate energy in different regions of the frequency domain. In the interconnection of two systems, it is known that if both the systems are dissipative then the interconnection is stable. Similarly if both systems attenuate signals, then the interconnection is stable. These scenarios are intuitive at the same time conservative. For example, if all that is known about the tip-sample interaction is that it is passive or dissipative, then we can conclude stability only if the real part of the frequency response $G(j\omega)$ is strictly less than zero. This condition is difficult to satisfy for a typical cantilever. However it is possible that the frequency regions in which the systems generate and dissipate energy counterbalance each other that makes the interconnection stable.

A similar scenario could arise for signal amplification and attenuation. Hence a characterization of dissipation and attenuation as a function of the frequencies is essential that provided by the frequency domain characterization of the cantilever in terms of its frequency response and that of the tip-sample interaction in terms of the FCs. Such an approach is used to derive conditions for the existence and stability of periodic solutions for this case.

2.1.2 Existence and Stability of Periodic Solutions

We introduced a frequency domain characterization for the nonlinear tip-sample interaction forces using the notion of Frequency Constraints (FCs). There is also a notion of Incremental Frequency Constraint (IFC) as defined below,

Definition 2.1.1 ϕ is said to satisfy the Incremental Frequency Constraint defined by $\Pi = \begin{pmatrix} \Pi_{11} & \Pi_{12} \\ \Pi_{21} & \Pi_{22} \end{pmatrix}$ if

$$\int_{-\infty}^{\infty} \begin{pmatrix} \widehat{(y_1 - y_2)}(j\omega) \\ \widehat{(\phi(y_1) - \phi(y_2))}(j\omega) \end{pmatrix}^* \Pi(j\omega) \begin{pmatrix} \widehat{(y_1 - y_2)}(j\omega) \\ \widehat{(\phi(y_1) - \phi(y_2))}(j\omega) \end{pmatrix} d\omega \geq 0 \quad (2.6)$$

for all energy bounded signals $y_1 - y_2$.

If the tip-sample interaction ϕ satisfies the sector condition (2.1) and is also monotonic and slope restricted by b , then it also satisfies the IFC defined by Π_c , the circle FC (2.4).

For a finite set of N mode shapes, the state space description of the cantilever dynamics is given by,

$$\begin{aligned} \dot{x} &= Ax + B_1\eta + BF \\ p(t) &= \sum_{k=1}^N \xi_k q_k(t) = Cx \end{aligned} \quad (2.7)$$

where $x := \left(q_1 \ q_2 \ \dots \ q_N \ \dot{q}_1 \ \dot{q}_2 \ \dots \ \dot{q}_N \right)^T$ (the position and velocity corresponding to the N modes), η is the thermal noise forcing term. F describes all the external forces acting on the cantilever. A , B_1 and B are functions of the cantilever parameters.

By ignoring the noise and recognizing $F = g(t) + \phi(p(t))$ (the external forcing and tip-sample interaction force), from (2.7) we obtain,

$$\begin{aligned} \dot{x} &= Ax + B(\phi(p(t)) + g(t)) \\ p &= Cx \end{aligned} \quad (2.8)$$

As a first step towards establishing the existence and stability of periodic solutions we prove the global exponential stability of $x = 0$ for the dynamics described by Equation (2.8) with $g(t) = 0$. For a linear system, the input-output energy distribution over the entire frequency region is fully characterized by its frequency response. For the nonlinear tip-sample interaction forces, the FCs serve as generalized “frequency responses”. The following theorem states that knowing the frequency characterization of the linear cantilever system in terms of its frequency response and that of the tip-sample interactions in terms of the FCs, the stability of the feedback interconnection (the AFM) can be inferred. Note that the variations in attenuation and amplification of signals as a function of their frequency content is exploited to arrive at this condition for stability.

Let $\Pi = \begin{bmatrix} \Pi_{11} & \Pi_{12} \\ \Pi_{21} & \Pi_{22} \end{bmatrix}$. Assuming that $\Pi_{11} \geq 0$ and $\Pi_{22} \leq 0$, the global exponential stability can be concluded if ϕ satisfies the FC defined by Π and $\exists \epsilon > 0$ such that,

$$\begin{pmatrix} (j\omega I - A)^{-1}B \\ I \end{pmatrix}^* \tilde{\Pi}(j\omega) \begin{pmatrix} (j\omega I - A)^{-1}B \\ I \end{pmatrix} \leq -\epsilon I \quad \forall \omega \quad (2.9)$$

where $\tilde{\Pi} = \begin{pmatrix} C^T \Pi_{11} C & C^T \Pi_{12} \\ \Pi_{21} C & \Pi_{22} \end{pmatrix}$ (follows from Ref. [24]).

If $x = 0$ is proved to be a globally exponentially stable equilibrium point of the unforced (2.8), the converse Lyapunov theorem (see [25]) can be invoked to obtain a differentiable function W and constants $\alpha, \beta, \gamma, \mu > 0$ such that,

$$\alpha \|x\|^2 \leq W(x) \leq \beta \|x\|^2 \quad (2.10)$$

$$\left\| \frac{dW(x)}{dx} \right\| \leq \mu \|x\| \quad (2.11)$$

$$(2.12)$$

Also the converse Lyapunov theorem states that $W(x)$ when evaluated along the trajectories of the unforced (2.8) will satisfy,

$$\frac{d}{dt}W(x) = \frac{dW}{dx}(Ax + B\phi(Cx)) \leq -\gamma\|x\|^2 \quad (2.13)$$

$W(x)$ was obtained for the unforced system. The same $W(x)$ can be utilized for the forced system using the fact the periodic forcing is magnitude bounded. If $\dot{W}(x)$ is evaluated along the trajectories of (2.8) with $g(t) \neq 0$ and $g(t) \leq M < \infty$,

$$\begin{aligned} \frac{d}{dt}W(x) &= \frac{dW}{dx}(Ax + B\phi(Cx) + Bg(t)) \\ &= \frac{dW}{dx}(Ax + B\phi(Cx)) + \frac{dW}{dx}Bg(t) \\ &\leq -\gamma\|x\|^2 + \left|\frac{dW}{dx}\right|\|Bg(t)\| \\ &\leq -\gamma\|x\|^2 + \mu\|x\|\|B\|M \\ &= -\gamma a(x) \end{aligned}$$

where $a(x) = \|x\|^2 - \frac{\mu\|B\|M}{\gamma}\|x\|$. $a(x)$ is a continuous function of x . Also there exists $\xi > 0$ such that $a(x) > 0$ for $\|x\| \geq \xi$. From (2.10) as $\|x\| \rightarrow \infty$, $W(x) \rightarrow \infty$. In short we have found a function $W(x)$ for (2.8) such that

- $W(x) \rightarrow \infty$ as $\|x\| \rightarrow \infty$
- There exists $\xi > 0$ and a continuous function $a(x) > 0$ for $\|x\| \geq \xi$ such that for any solution $\|x(t)\| \geq \xi$, $\frac{d}{dt}(W(x(t))) \leq -a(x(t))$.

Hence there is a closed and bounded invariant set, F for (2.8), any solution of (2.8) reaches F and (2.8) has a solution $x_0(t) \in F$ bounded for $-\infty < t < \infty$ (see Lemma 1 and 2 in [26]).

Let $x(t)$ be another solution of (2.8). Let $\tilde{x}(t) = x(t) - x_0(t)$. From (2.8) we obtain,

$$\dot{\tilde{x}} = A\tilde{x} + B\tilde{\phi}(t, \tilde{y}), \quad \tilde{p} = C\tilde{x} \quad (2.14)$$

where $\tilde{\phi}(t, v) := \phi(v + p_0(t)) - \phi(p_0(t))$. The global exponential stability of (2.14) implies the stability of the solution $x_0(t)$ which can be established by searching for a Π such that $\tilde{\phi}$ satisfies the FC defined by Π and (2.9) is satisfied. However if ϕ satisfies the incremental FC defined by Π , then $\tilde{\phi}$ satisfies

the FC defined by Π . Hence the stability of the solution $x_0(t)$ can be concluded if ϕ satisfies the IFC defined by Π and Π satisfies (2.9).

Since the forcing is periodic with period T , $x_0(t + T)$ is also a solution of (2.8). But $x_0(t)$ defined over $-\infty$ to ∞ is a stable solution. Hence it is unique. So $x_0(t) = x_0(t + T)$. The results of this section are summarized in the following proposition.

Proposition 2.1.1 *For the system described by (2.8), assume that ϕ satisfies the FC defined by Π . If there exists $\epsilon > 0$ such that (2.9) is satisfied, then there exists a bounded solution $x_0(t)$ for (2.8). If ϕ also satisfies the IFC defined by Π , then this solution is stable and is periodic with the same period as that of $g(t)$.*

As a special case of Proposition 2.1.1 if the Popov FC (see 2.5) is used in the analysis, along with the existence of a bounded solution $x_0(t)$, the T periodicity of $x_0(t)$ can be shown ([26]).

2.1.3 Apriori bounds on the higher harmonics

The linear cantilever when forced sinusoidally generates an output of the same frequency. However, the nonlinear tip-sample interaction could generate other harmonics and even subharmonics of the forcing frequency. The frequency characterization in terms of the FCs give a quantitative measure of the generation of these harmonics. With this added information it is possible to obtain bounds on the higher output harmonics of the linear block. This idea was initially introduced by Megretski and Rantzer in Ref. [27]. In this approach we do not make any prior assumptions on the smallness of the higher harmonics. This approach betters other approaches where the interaction forces only for the first harmonic is evaluated which is equivalent to making a prior assumption on the sinusoidal nature of the periodic solution.

For the cantilever dynamics let the sinusoidal forcing signal $g(t) = g_1 e^{j\omega_0 t} + g_{-1} e^{-j\omega_0 t}$ and $G(j\omega)$ be the frequency response. Let the periodic deflection signal, $p(t) = \sum p_k e^{jk\omega_0 t}$ and the periodic interaction force signal, $h(t) = \sum h_k e^{jk\omega_0 t}$ ($h(t) = \phi(p(t))$). From the linearity and time invariance of G the following harmonic balance equations are satisfied. For $|k| \neq 1$,

$$\begin{pmatrix} p_k \\ h_k \end{pmatrix} = \begin{pmatrix} 1 \\ G^{-1}(jk\omega_0) \end{pmatrix} p_k \quad (2.15)$$

and for $|k| = 1$,

$$\begin{pmatrix} p_k \\ h_k \end{pmatrix} = \begin{pmatrix} 1 & 0 \\ G^{-1}(jk\omega_0) & -1 \end{pmatrix} \begin{pmatrix} p_k \\ g_k \end{pmatrix}. \quad (2.16)$$

Assume that the tip-sample interaction force ϕ satisfies the FC defined by II. From this FC as $p(t)$ and $\phi(p(t))$ are periodic with Fourier coefficients p_k and h_k respectively one can obtain the relation

$$\sum_k \begin{pmatrix} p_k \\ h_k \end{pmatrix}^* \Pi(jk\omega_0) \begin{pmatrix} p_k \\ h_k \end{pmatrix} \leq 0. \quad (2.17)$$

Assume that the following condition is satisfied,

$$\begin{pmatrix} G(jk\omega_0) \\ 1 \end{pmatrix}^* \Pi(jk\omega_0) \begin{pmatrix} G(jk\omega_0) \\ 1 \end{pmatrix} \leq -\epsilon \text{ for all } |k| \neq 1 \quad (2.18)$$

Note that this condition is satisfied if the condition for global exponential stability (2.9) is satisfied (however it is less conservative than the condition for global exponential stability as (2.18) is obtained from (2.9) by substituting $k\omega_0$ for ω). Using the three algebraic relations described by (2.16) (the frequency response of the cantilever), (2.17) (the FCs of the tip-sample interaction) and (2.18) (a *stability condition*) one can establish bounds on the higher harmonics as described by the following proposition.

Proposition 2.1.2 *For the system described by (2.8), let $G(j\omega)$ be the frequency response of the cantilever. Assume that the tip-sample interaction forces satisfy the FC defined by $\Pi(j\omega)$ and*

$$\begin{pmatrix} G(jk\omega_0) \\ 1 \end{pmatrix}^* \Pi(jk\omega_0) \begin{pmatrix} G(jk\omega_0) \\ 1 \end{pmatrix} \leq -\epsilon \text{ for all } |k| \neq 1.$$

Suppose there exists a $\tau > 0$ and β such that,

$$\begin{pmatrix} 0 & 0 & 0 \\ 0 & -\beta^2 & 0 \\ 0 & 0 & 1 \end{pmatrix} + \tau \begin{pmatrix} K_1 & L_1 & 0 \\ L_1^* & M_1 & 0 \\ 0 & 0 & K_{k_0} \end{pmatrix} < 0 \quad (2.19)$$

where $\begin{pmatrix} K_k & L_k \\ L_k^* & M_k \end{pmatrix} = \begin{pmatrix} 1 & 0 \\ G^{-1}(jk\omega_0) & -1 \end{pmatrix}^* \Pi(jk\omega_0) \begin{pmatrix} 1 & 0 \\ G^{-1}(jk\omega_0) & -1 \end{pmatrix}$. Then β multiplied by the magnitude of the first Fourier coefficient of $g(t)$ will give an upper bound on the magnitude of the k_0^{th} Fourier coefficient of periodic orbit of the cantilever $p(t)$.

Most of the proof of this proposition follows from the work of Megretski and Rantzer (see [27]). The following Lemma can be proved using (2.18).

Lemma 2.1.1 $\begin{pmatrix} p_k \\ h_k \end{pmatrix}^* \Pi(jk\omega_0) \begin{pmatrix} p_k \\ h_k \end{pmatrix} \leq 0$ for all $|k| \neq 1$.

Proof of Lemma 2.1.1: From 2.18,

$$\begin{aligned} \begin{pmatrix} G(jk\omega_0) \\ 1 \end{pmatrix}^* \Pi(jk\omega_0) \begin{pmatrix} G(jk\omega_0) \\ 1 \end{pmatrix} &\leq -\epsilon \\ h_k^* \begin{pmatrix} G(jk\omega_0) \\ 1 \end{pmatrix}^* \Pi(jk\omega_0) \begin{pmatrix} G(jk\omega_0) \\ 1 \end{pmatrix} h_k &\leq -\epsilon|h_k|^2 \\ \begin{pmatrix} G(jk\omega_0)h_k \\ h_k \end{pmatrix}^* \Pi(jk\omega_0) \begin{pmatrix} G(jk\omega_0)h_k \\ h_k \end{pmatrix} &\leq -\epsilon|h_k|^2 \\ \begin{pmatrix} p_k \\ h_k \end{pmatrix}^* \Pi(jk\omega_0) \begin{pmatrix} p_k \\ h_k \end{pmatrix} &\leq 0 \end{aligned}$$

■

Lemma 2.1.2 For $|k_0| \neq 1$, $\begin{pmatrix} p_1 \\ g_1 \\ p_{k_0} \end{pmatrix}^* \begin{pmatrix} K_1 & L_1 & 0 \\ L_1^* & M_1 & 0 \\ 0 & 0 & K_{k_0} \end{pmatrix} \begin{pmatrix} p_1 \\ g_1 \\ p_{k_0} \end{pmatrix} \geq 0$, where $\begin{pmatrix} K_k & L_k \\ L_k^* & M_k \end{pmatrix} =$

$$\begin{pmatrix} 1 & 0 \\ G^{-1}(jk\omega_0) & -1 \end{pmatrix}^* \Pi(jk\omega_0) \begin{pmatrix} 1 & 0 \\ G^{-1}(jk\omega_0) & -1 \end{pmatrix}$$

Proof of Lemma 2.1.2: From the fact that ϕ satisfies the FC defined by Π ,

$$\begin{aligned}
0 &\leq \sum \begin{pmatrix} p_k \\ h_k \end{pmatrix}^* \Pi(jk\omega_0) \begin{pmatrix} p_k \\ h_k \end{pmatrix}. \\
0 &\leq 2 \begin{pmatrix} p_1 \\ h_1 \end{pmatrix}^* \Pi(j\omega_0) \begin{pmatrix} p_1 \\ h_1 \end{pmatrix} + 2 \begin{pmatrix} p_{k_0} \\ h_{k_0} \end{pmatrix}^* \Pi(jk_0\omega_0) \begin{pmatrix} p_{k_0} \\ h_{k_0} \end{pmatrix} \\
0 &\leq \begin{pmatrix} p_1 \\ g_1 \end{pmatrix}^* \begin{pmatrix} 1 & 0 \\ G^{-1}(j\omega_0) & -1 \end{pmatrix}^* \Pi(j\omega_0) \begin{pmatrix} 1 & 0 \\ G^{-1}(j\omega_0) & -1 \end{pmatrix} \begin{pmatrix} 1 & 0 \\ G^{-1}(j\omega_0) & -1 \end{pmatrix} \begin{pmatrix} p_1 \\ g_1 \end{pmatrix} + \\
&\quad \begin{pmatrix} p_{k_0} \\ g_{k_0} \end{pmatrix}^* \begin{pmatrix} 1 \\ G^{-1}(jk_0\omega_0) \end{pmatrix}^* \Pi(jk_0\omega_0) \begin{pmatrix} 1 \\ G^{-1}(jk_0\omega_0) \end{pmatrix} \begin{pmatrix} p_{k_0} \\ g_{k_0} \end{pmatrix} \\
0 &\leq \begin{pmatrix} p_1 \\ g_1 \\ p_{k_0} \end{pmatrix}^* \begin{pmatrix} K_1 & L_1 & 0 \\ L_1^* & M_1 & 0 \\ 0 & 0 & K_{k_0} \end{pmatrix} \begin{pmatrix} p_1 \\ g_1 \\ p_{k_0} \end{pmatrix}
\end{aligned}$$

Note that in the second step of the proof, lemma 2.1.1 is used. ■

Using Lemma 2.1.2, the problem of obtaining bounds on the higher harmonics is translated to the problem of solving a linear matrix inequality. Suppose there exists a $\tau > 0$ and β such that,

$$\begin{pmatrix} 0 & 0 & 0 \\ 0 & -\beta^2 & 0 \\ 0 & 0 & 1 \end{pmatrix} + \tau \begin{pmatrix} K_1 & L_1 & 0 \\ L_1^* & M_1 & 0 \\ 0 & 0 & K_{k_0} \end{pmatrix} < 0 \quad (2.20)$$

Then,

$$\begin{aligned}
&\Rightarrow \begin{pmatrix} p_1 \\ g_1 \\ p_{k_0} \end{pmatrix}^* \begin{pmatrix} 0 & 0 & 0 \\ 0 & -\beta^2 & 0 \\ 0 & 0 & 1 \end{pmatrix} \begin{pmatrix} p_1 \\ g_1 \\ p_{k_0} \end{pmatrix} + \tau \begin{pmatrix} p_1 \\ g_1 \\ p_{k_0} \end{pmatrix}^* \begin{pmatrix} K_1 & L_1 & 0 \\ L_1^* & M_1 & 0 \\ 0 & 0 & K_{k_0} \end{pmatrix} \begin{pmatrix} p_1 \\ g_1 \\ p_{k_0} \end{pmatrix} < 0 \\
&\Rightarrow \begin{pmatrix} p_1 \\ g_1 \\ p_{k_0} \end{pmatrix}^* \begin{pmatrix} 0 & 0 & 0 \\ 0 & -\beta^2 & 0 \\ 0 & 0 & 1 \end{pmatrix} \begin{pmatrix} p_1 \\ g_1 \\ p_{k_0} \end{pmatrix} < 0 \\
&\Rightarrow \begin{pmatrix} g_1 \\ p_{k_0} \end{pmatrix}^* \begin{pmatrix} -\beta^2 & 0 \\ 0 & 1 \end{pmatrix} \begin{pmatrix} g_1 \\ p_{k_0} \end{pmatrix} < 0 \\
&\Rightarrow -\beta^2 |g_1|^2 + |p_{k_0}|^2 < 0
\end{aligned}$$

That $|p_{k_0}| < \beta|g_1|$ follows directly. Note that Lemma 2.1.2 is used in the second step.

For each higher harmonic, k_0 of $p(t)$, the smallest β is obtained such that the Linear Matrix Inequality (LMI) given by (2.19) is satisfied with that β and some $\tau > 0$. This problem can be solved as an optimization problem with linear matrix inequality constraints. Efficient software is readily available to solve such problems. Note that the bounds on the higher harmonics can also be used to assess the limitations on how well the tip-sample potential can be probed using the micro-cantilever. The harmonic balance equations which were used in the previous section to obtain bounds on the higher harmonics can be further used to identify a model for the tip-sample interaction as shown in Chapter 3. As will be seen in the section on experimental results this framework accurately predicts the magnitude of the higher harmonics.

2.2 Experimental results and discussion

An AFM was operated in the dynamic-mode using a silicon cantilever of length $240\mu m$ and spring constant $2 N/m$. The model parameters were evaluated by analyzing the response to thermal noise as described in Ref. [28]. A two-mode model was identified (see Figure 2.3). In order to analyze this behavior a simple model is developed for the tip-sample interaction force which is presented in greater detail in Chapter 3. Figure 2.2(b) depicts the model for the tip-sample interaction force. The tip-sample interaction force has long range attractive and short range repulsive components. The long range attractive component is modeled by a negative spring denoted by $-\omega_a^2$. The repulsive component is modeled by a positive spring denoted by ω_b^2 . The dissipation in the sample is captured by a damper denoted by c_a . l is a good measure of the tip-sample interaction forces and is the distance between the tip and the beginning of the repulsive regime. d is the length of the attractive regime.

The tip-sample interaction forces acting on the oscillating tip is estimated to be lying in a sector (see Figure 2.4) with slope $k_{sl} := d\omega_a^2/l$, where ω_a is estimated to be $0.3 \mu s^{-1}$ and the length of the attractive region d is estimated to be $3 nm$. l corresponds to the tip-sample separation. Note that a reduction in the separation l corresponds to a higher slope for the sector characterizing the tip-sample interaction as depicted in Figure 2.4.

For the analysis the tip-sample separation is assumed to vary over a span of $40 nm$ to $75 nm$ in accordance with experiments. If ϑ belongs to a sector, $[0 k_{sl}]$, ϑ satisfies the Popov FC defined by

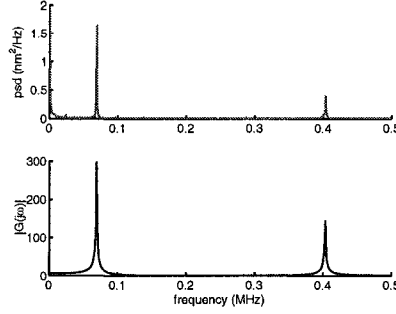


Figure 2.3 The experimentally obtained thermal noise response and the frequency response of the identified model. A two mode approximation is used. The first and the second modal frequencies are at $f_0 = 69.1 \text{ kHz}$ and $f_1 = 403 \text{ kHz}$ respectively. The quality factor of the first mode is estimated to be 56.

$\Pi(\eta) = \begin{pmatrix} 0 & j\omega\eta + k_{sl} \\ j\omega\eta + k_{sl} & -2 \end{pmatrix}$, where η is any real number. For $\eta = 0.015$ it can be shown that condition (2.9) is satisfied by $\Pi(\eta)$ for all the slopes given by l varying from 40 nm to 75 nm . This is graphically illustrated in Figure 2.5 for the case $l = 40.75 \text{ nm}$. The condition (2.9) for the above Π translates to the condition that $-1 + \text{Re}((G(j\omega)(j\omega\eta + k_{sl}))$ should be less than 0 for all ω where Re denotes the real part. This proves the existence of a $\frac{2\pi}{\omega_0}$ periodic solution.

To analyze the global exponential stability of the periodic solution, the circle FC can be used. The stability condition holds only if the slope of the attractive region is assumed to be less than 0.01. Such a condition is satisfied only if the tip encounters mild attractive forces that is when the tip sample separation is relatively large. For most tip-sample separations, there are more than one fixed point solution for the AFM operating in the dynamic-mode and thus it is not expected that the condition for a globally stable T periodic solution is met (indeed it is possible that under certain operating conditions subharmonics are present; see Ref. [18]).

As the next step bounds are obtained for the higher harmonics for different values of tip-sample separation l . For each higher harmonic, an optimization problem is solved using *MATLAB Linear Matrix Inequality toolbox*. The smallest possible β is obtained such that for that beta and a positive τ the linear matrix inequality (2.19) in Section 2.1.3 is satisfied. The FC chosen for this is $\Pi(\eta) =$

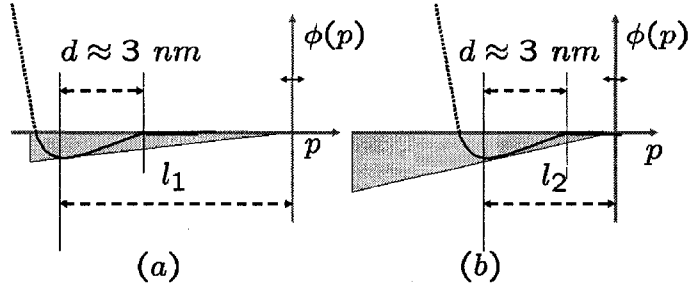


Figure 2.4 The tip-sample interaction forces acting on the oscillating tip is estimated to be lying in sectors as shown in this figure. As the tip-sample separation reduces, the slope of the sector needed to characterize the nonlinearities increases. The sector slope in (b) is greater than the slope of the sector in (a).

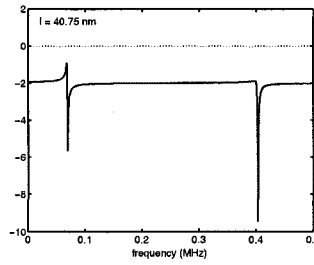


Figure 2.5 The condition (2.9) translates to the function $-1 + \text{Re}((G(j\omega)(j\omega\eta + k_{sl}))$ being less than 0 for all ω . A plot of $-1 + \text{Re}((G(j\omega)(j\omega\eta + k_{sl}))$ versus ω is shown in the figure.

$$\begin{pmatrix} 0 & j\omega\eta + k_{sl} \\ j\omega\eta + k_{sl} & -2 \end{pmatrix}$$
 with $\eta = 0.015$. From the gain β , bounds on the higher harmonics are obtained for different tip-sample separations (See Figure 2.6). A two mode model of the cantilever is employed. It is seen that the theoretical bounds on the harmonics increase as the tip-sample separation reduces. The reduction in the tip-sample separation is captured by an increase in the slope of the sector used to characterize the nonlinear interactions.

The theory developed for obtaining the harmonic bounds can be extended in a straightforward manner to obtain bounds on the subharmonics of the first modal frequency. Note that Proposition 2.1.2 needs only the assumption of the solution being periodic. This has the potential of being used

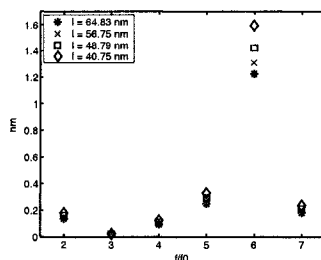


Figure 2.6 Theoretical upper bounds on the higher harmonics are obtained using an approximate characterization of tip-sample interaction forces for different tip-sample separations.

to analyze cases where subharmonics arise in an AFM operation. The theoretical bounds obtained for the subharmonics are found to be very small compared to the tip-sample separation. Hence there is a prospect of events like period doubling occurring in the usual AFM operation, however they may not be easily observed due to the smallness of the subharmonics.

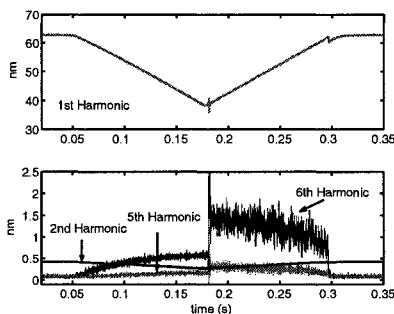


Figure 2.7 This figure depicts the 1st, 2nd, 5th and 6th harmonics of the cantilever oscillation during the approach and retract of the sample towards the tip.

Tapping mode experiments were conducted to study the validity of the bounds obtained on the higher harmonics. The sample (Highly Oriented Pyrolytic Graphite) was sufficiently far from the cantilever initially. The sample is then progressively moved towards the cantilever and then away from the sample. During this process the deflection signal is recorded at a sampling frequency of 1 MHz. From the deflection data the magnitudes of the harmonics of the cantilever oscillation are obtained as a function

of time. The variation of the first, second, fifth and sixth harmonic is depicted in Figure 2.7. While approaching the sample surface, the magnitude of the first harmonic reduces with a reduction in the tip-sample separation. It is seen in Figure 2.7 that for a certain tip-sample separation the first harmonic exhibits a discontinuous jump to a higher value and stays there till it jumps back to a lower value for a larger tip-sample separation. This is the region where the tip traverses the attractive and repulsive regimes of the tip-sample interaction potential. In the rest of the region it can be assumed that the tip traverses the attractive regime. This assumption is also validated by numerical simulations and results from Ref. [29]. The higher harmonics increase with reducing tip-sample separation possibly since the fraction of the period the cantilever interacts with the nonlinearity increases with reducing tip-sample separation. Of particular interest is the harmonics close to the modal frequencies of the cantilever. As Figure 2.7 shows, the 5th and 6th harmonics are particularly sensitive to the reducing tip-sample separation. Another interesting aspect is the sudden increase in the magnitude of the 5th and 6th harmonic when the cantilever starts interacting with the repulsive regime of the interaction forces.

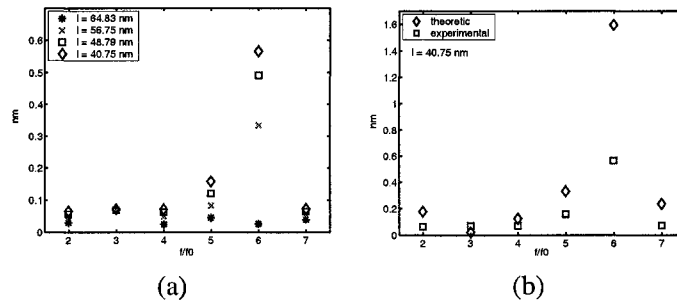


Figure 2.8 (a) This figure shows the magnitude of the first seven higher harmonics as the sample approaches the cantilever for different values of tip-sample separation. For reducing tip-sample separations the magnitudes of the higher harmonics increase as the fraction of the period the oscillating tip interacts with the nonlinearity is increasing. This is also captured by the theoretical bounds on the harmonics shown in Figure 2.6. (b) For a tip-sample separation of 40.75 nm , the theoretical bounds on the harmonics are compared with the experimental values obtained.

From the sampled deflection data, the magnitudes of the first seven higher harmonics are obtained for different tip-sample separations in the region where the tip does not interact with the repulsive

forces (see 2.8(a)). This ensures that the nonlinearities satisfy the sector condition which was used to derive the theoretical bounds. As in the case of the theoretical bounds, the magnitudes of the higher harmonics increase for smaller values of tip-sample separation. Figure 2.8(b) compares the theoretic bounds on the harmonics with those measured experimentally for a representative tip-sample separation of 40.75 nm . The theoretical bounds serve as a good upper bound for the experimental values obtained.

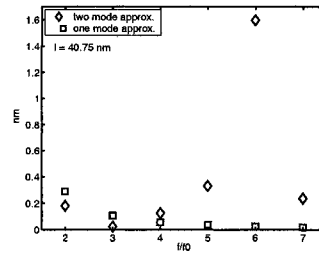


Figure 2.9 The theoretical bounds on the higher harmonics are compared for the cases where the 1st and 2nd mode approximations of the cantilever dynamics are used. The bounds on the harmonics which are close to the 2nd modal frequency are particularly erroneous if only a first mode approximation is used.

The theoretical bounds on the higher harmonics were also obtained using a one mode approximation of the cantilever. As Figure 2.9 shows, if a single mode approximation is used there is a significant error especially in the calculation of bounds for the harmonics which are close to the modal frequencies of the cantilever. The prominence of the higher harmonics close to the frequency of the eigenmodes confirms the observations made in Ref. [29] through numerical simulations. Spectral analysis of the deflection data shows the presence of the first subharmonic and its multiples particularly in the case where the tip interacts with both the attractive and repulsive regimes of the interaction potential (see Figure 2.10).

The analytical and experimental results confirm that the study can be effectively utilized for obtaining quantitative bounds on the higher harmonics. This in turn can play a significant role in imaging and assessing the limitations of the tapping mode operation. Another important study that can be conducted is determining the number of modes of the cantilever that need to be included in any particular analysis. As indicated earlier, a single mode model has a very small upper bound on the sixth harmonic where

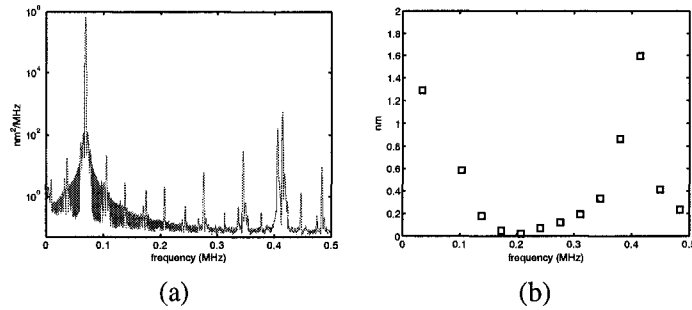


Figure 2.10 (a) Spectral analysis of the deflection data when the tip is interacting with the repulsive as well as attractive regime of tip-sample interactions distinctly shows the presence of the the first subharmonic and its multiples indicating a $2/f_0$ periodic solution. (b) Theoretical bounds were obtained for the first subharmonic and its multiples except for the first harmonic. The bounds show a similar trend as that observed experimentally.

as the second mode approximation brings out the importance of the sixth harmonic. The possibility of studying subharmonics is another interesting direction suggested by the presented work.

2.3 Conclusions

The feedback perspective with the cantilever viewed as a linear system and the tip-sample interaction appearing as a nonlinear feedback is useful in analyzing the Atomic Force Microscope dynamics. Conditions for the existence and stability of periodic solutions for such a system when forced sinusoidally are obtained. These results are applied to the case where the AFM is operated in the tapping mode. The near sinusoidal nature of periodic solutions is established by obtaining bounds on the higher harmonics. In the next chapter, the systems perspective combined with harmonic balance and power balance tools are employed to identify the cantilever tip-sample interaction forces.

CHAPTER 3 Harmonic and power balance tools for the identification of tapping mode AFM dynamics

As mentioned earlier, much of the research on tapping mode AFM has centered around numerically solving nonlinear differential equations that include terms to account for the tip-sample interaction. These models were successful in capturing many of the intricate details present in most experimental data. However due to their complexity, the numerical models preclude identification of model parameters in a straightforward manner. Indeed the set of existing tools to identify a given model of the interaction from experimental data is inadequate. Another void in this area is a systematic methodology for the purposes of identification (some studies in this direction are pursued in Ref. [30]). Of particular interest is a set of common tools that can be applied over a wide range of tapping mode AFM applications. Such tools are particularly relevant because of the diverse variety of materials and properties that the tapping mode AFM is used for imaging.

In this chapter the feedback perspective of the tapping mode dynamics introduced in the Chapter 2 is further exploited to develop a set of principles that can be used for identifying the tip-sample interaction forces. These general tools can be utilized for a wide range of tapping mode applications. We develop a tractable parametric model of the tapping mode dynamics and apply the developed identification tools to estimate the parameters of the proposed model. It is shown that the identification paradigm developed is powerful and that a simple model can match experimental data remarkably well. The tools also elucidate the limitations of tapping mode AFM in identifying the tip-sample potential.

This chapter is organized as follows. In Section 3.1.1 we develop the analytical principles for identification purposes. In Section 3.1.2 we present the model of the cantilever and the tip-sample interaction used in this paper. We then specialize the identification tools for this model. In Section 3.2 we present the experimental results.

3.1 Analysis

3.1.1 Harmonic and power balance tools

Similar to the analysis in Chapter 2, we assume that a linear time-invariant model G of the cantilever suffices to predict its behavior. Thus G is a linear time-invariant operator which takes in the sample and the drive force as its input and provides the tip-displacement as its output. Note that G includes the effect of the air damping force. Also note that efficient techniques exist in the literature to obtain a precise model of G (see for example Ref. [28]).

In this analysis we assume that $p(t)$ is a T periodic solution. Because the nonlinear force on the cantilever due to the sample is assumed to be time-invariant it follows that $h(p, \dot{p})$ is also periodic with period T . Thus p , $h(p, \dot{p})$ and $g(t)$ all admit expansions of the form $p(t) = \sum_{k=-\infty}^{\infty} p_k e^{jk\omega t}$, $h(p(t), \dot{p}(t)) = \sum_{k=-\infty}^{\infty} h_k e^{jk\omega t}$ and $g(t) = \sum_{k=-\infty}^{\infty} g_k e^{jk\omega t}$, where $x_k = x_{kr} + jx_{ki}$ are the exponential Fourier coefficients of x and $\omega = 2\pi/T$.

Since the cantilever model G is a linear time-invariant system, it follows from the Fourier series properties of linear time-invariant systems that the input and output harmonics of the system are related by

$$G(jk\omega)(-g_k + h_k) + p_k = 0, \text{ for all } k = 0, \pm 1, \pm 2, \dots \quad (3.1)$$

If the cantilever dynamics (in the sense described above) is linear time-invariant and the tip-sample interaction is time-invariant then the Fourier coefficients g_k , h_k and p_k of the forcing $g(t)$, tip-sample interaction force on the periodic orbit $h(p(t))$ and the tip displacement $p(t)$ respectively have to obey the harmonic balance equations given by (3.1).

In order to verify the harmonic balance equations, data from Ref. [8] was used where advanced models for tip-sample interaction were employed. The tip-sample interaction model given in Ref. [8] captures most of the features seen in experimental data. The simulation data used corresponds to a sinusoidal forcing at a frequency of $\omega = 300 \text{ kHz}$ which is same as the resonant frequency of the cantilever. Let $u(t) = g(t) - h(p, \dot{p})$. The magnitude of the Fourier transforms of the simulation data $p(t)$ and $u(t)$ given by $|\hat{p}(j\omega)|$ and $|\hat{u}(j\omega)|$ respectively are shown in Figure 3.1. Next the ratios between $|\hat{p}(jk\omega)|$ and $|\hat{u}(jk\omega)|$ for $k = 1$ to 10 are compared with the corresponding points on the frequency response plot of G . The remarkable agreement between the two verifies Equation (3.1).

The only assumption made for Equation (3.1) to be true is that the cantilever dynamics is linear time-invariant and that the tip-sample interaction is time-invariant. We will now utilize (3.1) to develop schemes for identifying the tip-sample interaction.

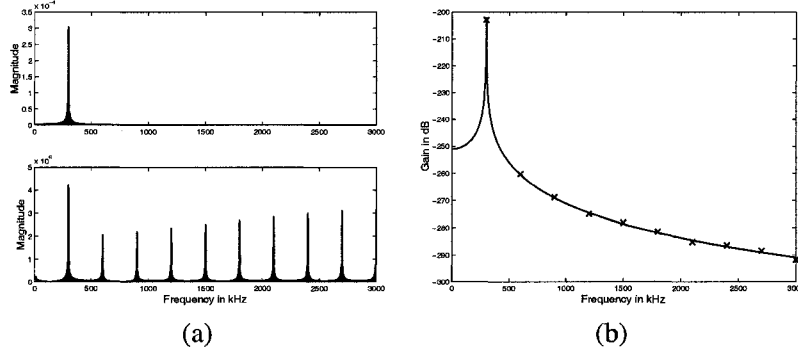


Figure 3.1 The magnitude plots of the Fourier transforms of $p(t)$ and $u(t)$ are shown first. The ratios between $|\hat{p}(jk\omega)|$ and $|\hat{u}(jk\omega)|$ for $k = 1$ to 10 are then compared with the corresponding points on the frequency response plot of G thus verifying the harmonic balance.

Note that in Equation (3.1), thermal noise response plots can be used to identify $G(jk\omega)$ (see Ref. [28]). In Equation (3.1) the Fourier coefficients of the forcing g_k are known and the Fourier coefficients p_k of the cantilever oscillations can be found by performing a Fourier analysis on the measured cantilever-tip oscillations. Equation (3.1) can then be used to evaluate h_k . Indeed Equation (3.1) can be rewritten as

$$h_k = g_k - \frac{p_k}{G(jk\omega)}, \quad (3.2)$$

where h_k are the unknowns and the right hand side of the above equation can be obtained from experimental data. Note that h_k are the Fourier coefficients of $h(p(t))$ where $p(t)$ is the steady state cantilever oscillation. The steady state periodic orbit of the cantilever depends on the forcing frequency ω , the magnitude of the forcing γ , and the tip-sample offset ℓ . Thus h_k , g_k and p_k are functions of ω , γ and ℓ . By varying each one of these parameters we can evaluate $h_k(\omega, \gamma, \ell)$ for different values of ω , γ and ℓ . The Fourier coefficients h_k can be processed to provide information about the sample properties that can be used to identify various parameters in a given model of the interaction between the tip and the sample.

Note that any time-invariant model of the tip-sample interaction has to satisfy (3.2) if we account for any noise in the detection of $p(t)$. An approach to identifying the tip-sample interaction is to assume a parametric model of the tip-sample interaction which takes in as input the tip-displacement and velocity and provides the force on the cantilever due to the sample as its output. Let $H(\Theta)$ denote such a model where Θ is a finite set of parameters. Thus we have $h(p(t)) = H(\Theta)(p(t))$. The corresponding minimization problem is

$$\min_{\Theta} \sum_{k=0}^{\infty} |H_k - h_k|^2, \quad (3.3)$$

where H_k are the Fourier coefficients of $H(\Theta)(p(t))$. Note that the tractability of the problem (3.3) depends on the parametric model H and thus care should be taken so that the resulting minimization problem is solvable. We will follow this approach for identification in the next section. A limitation of the tapping mode AFM in identifying the tip-sample interaction is also indicated by the above discussion. Note that the cantilever tip oscillation (which is the measured signal) contains negligible information on the high frequency content of $h(p(t))$, because such information is filtered out by the cantilever. Thus the tapping mode AFM can be utilized to identify the tip-sample interaction only up to the first harmonic of $h(p(t))$.

Now we introduce power balance technique for tapping mode AFM. This technique is based on the fact that at steady state the average rate at which energy is fed into the cantilever must equal the average rate at which energy is dissipated by the cantilever. The instantaneous power delivered by the driver is the force on the driver (f_{drive}) times the velocity of the driver as given by

$$P_{in} = \frac{1}{m} f_{drive} \dot{b}(t). \quad (3.4)$$

Similarly P_d and P_t are given by

$$P_d = \frac{1}{m} f_{damp} \dot{p}(t) \quad (3.5)$$

$$P_t = \frac{1}{m} f_{int} \dot{p}(t), \quad (3.6)$$

where f_{damp} is the damping force and f_{int} is the tip-sample interaction force respectively. $\overline{P_{in}}$, $\overline{P_d}$ and $\overline{P_t}$ are obtained by averaging P_{in} , P_d and P_t over one cycle of the cantilever oscillation respectively. The fact that energy is conserved results in

$$\overline{P_{in}} = \overline{P_d} + \overline{P_t}. \quad (3.7)$$

From the knowledge of the tip motion $p(t)$ and the cantilever model $G(j\omega)$ we can evaluate $\overline{P_{in}}$ and $\overline{P_d}$. Using Equation (3.7) we can evaluate $\overline{P_t}$. As will be seen later, this forms another tool to identify the parameters of the tip-sample interaction.

3.1.2 Cantilever and tip-sample interaction model

We now apply the harmonic and power balance tools to the tapping mode dynamics assuming a model for the cantilever and a model for the tip-sample interaction. For most applications the dynamical equation for the displacement of the cantilever is well modeled by

$$\ddot{p} + 2\xi\omega_0\dot{p} + \omega_0^2 p + h(p, \dot{p}) = g(t), \quad (3.8)$$

where $\omega_0 = \sqrt{\frac{k}{m}}$, $2\xi\omega_0 = \frac{c}{m}$ and $g(t) = \frac{kb(t)}{m}$ and h is the force due to the sample per unit mass that is assumed to be dependent only on the position and velocity of the cantilever-tip. The cantilever model dynamics are described by Figure 3.2. Assuming the second-order model described by Equation (3.8) and that the tip-displacement is sinusoidal in nature, the harmonic balance equations (3.1) reduce to

$$h_0 - g_0 + \omega_0^2 p_0 = 0 \quad (3.9)$$

$$h_{1r}(a, \varphi, p_0) - g_{1r} + \Omega \frac{a}{2} \cos \varphi - 2\xi\omega\omega_0 \frac{a}{2} \sin \varphi = 0 \quad (3.10)$$

$$h_{1i}(a, \varphi, p_0) - g_{1i} + 2\xi\omega\omega_0 \frac{a}{2} \cos \varphi + \Omega \frac{a}{2} \sin \varphi = 0. \quad (3.11)$$

where $\Omega = \omega_0^2 - \omega^2$. Note that $p_{1r} = \frac{a}{2} \cos \varphi$ and $p_{1i} = \frac{a}{2} \sin \varphi$. Also, for the second order model of the cantilever given by Equation (3.8), $G(j\omega) = 1/(-\omega^2 + j2\xi\omega\omega_0 + \omega_0^2)$.

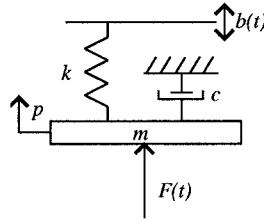


Figure 3.2 Model of the cantilever. F is the force on the cantilever due to the sample and b describes the displacement of the base of the cantilever.

Let the dither forcing function be given by $b(t) = a_d \cos(\omega t)$ (note that $a_d = \frac{\gamma}{\omega_0^2}$) and the steady state sinusoidal orbit be given by $p(t) = a \cos(\omega t + \varphi) + p_0$ where a is the amplitude of the cantilever,

φ is the phase difference between $p(t)$ and $b(t)$ and p_0 is the DC offset. Averaging Equation (3.4) over a complete cycle we obtain $\overline{P_{in}}$ to be

$$\overline{P_{in}} = -\frac{1}{2} \frac{k}{m} a_d a \omega \sin(\varphi). \quad (3.12)$$

Similarly $\overline{P_{air}}$ is given by

$$\overline{P_{air}} = \frac{1}{2} \frac{c}{m} a^2 \omega^2. \quad (3.13)$$

From Equation (3.7)

$$\overline{P_{tip}} = -\frac{1}{2m} \frac{k a^2 \omega}{Q} \left(\frac{Q a_d \sin(\varphi)}{a} + \frac{\omega}{\omega_0} \right). \quad (3.14)$$

If the drive frequency is chosen to be ω_0 , Equation (3.14) reduces to

$$\overline{P_{tip}} = -\frac{1}{2m} \frac{k a^2 \omega_0}{Q} \left(\frac{a_0}{a} \sin(\varphi) + 1 \right), \quad (3.15)$$

where $a_0 = Q a_d$ is the resonance amplitude of the cantilever when not subjected to the sample influence with $\omega = \omega_0$ and

$$Q = \frac{k}{c \omega_0} = \frac{1}{2\xi} = \frac{\sqrt{km}}{c}. \quad (3.16)$$

For a conservative system, $\overline{P_{tip}}$ is equal to zero since there is no dissipation in the sample. Thus Equation (3.15) shows that the plot of $-\sin \varphi$ against a/a_0 will have a slope of one for a conservative system (see Ref. [31] for more details). Hence a deviation from a slope of one is likely to indicate power dissipation in the sample. In most experiments $-\sin \varphi$ Vs a/a_0 plot is still linear and has a slope considerably less than one indicating significant energy dissipation.

A model for the nonlinear tip-sample interaction force (denoted by h) is developed next. Experimental data has indicated that a force curve of the form shown in Figure 3.3 well characterizes the force on the cantilever due to the sample. It indicates long range attractive forces and short range strong repulsive forces. We assume a piecewise linear cantilever tip-sample force curve. The additional assumption that the interaction force is also a function of the velocity of the cantilever tip is made.

The model of the tapping mode dynamics with the piecewise linear interaction is described by Figure 3.4. The negative spring accounts for long range attractive forces and the positive spring accounts for the short range strong repulsive forces. The dampers will account for the energy dissipation in the

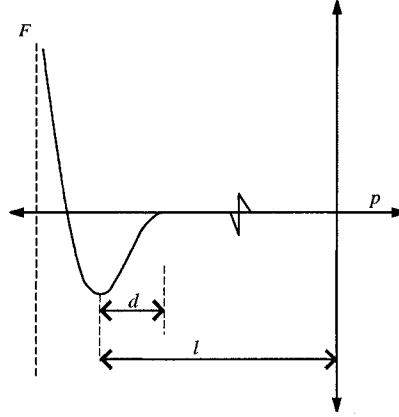


Figure 3.3 Sketch of a typical cantilever-sample force as a function of position. It indicates long range attractive forces and short range strong repulsive forces.

sample. The variable l will characterize the tip-sample separation. Specifically we assume that

$$h(p, \dot{p}) = 0 \text{ if } p \geq -l + d \quad (3.17)$$

$$= -\omega_a^2(p + l - d) + c_a \dot{p} \text{ if } -l \leq p < -(l - d) \quad (3.18)$$

$$= \omega_b^2(p + l) - \omega_a^2(p + l - d) + c_a \dot{p} + c_b \dot{p} \text{ if } p < -l. \quad (3.19)$$

When p is periodic, h is periodic and the Fourier coefficients h_0 and h_1 of the periodic function $h(p, \dot{p})$ when $p(t) = a \cos(\omega t + \varphi) + p_0$ are given by

$$\begin{aligned} h_0(a, p_0) &= 0 \text{ if } p_0 - a \geq -l + d & (3.20) \\ &= \frac{a\omega_a^2}{\pi} (\sqrt{1 - s_1^2} - |s_1| \cos^{-1}(|s_1|)) \text{ if } -l \leq p_0 - a < -l + d \\ &= \frac{a\omega_a^2}{\pi} (\sqrt{1 - s_1^2} - |s_1| \cos^{-1}(|s_1|)) \\ &\quad - \frac{a\omega_b^2}{\pi} (\sqrt{1 - s_2^2} - |s_2| \cos^{-1}(|s_2|)) \text{ if } p_0 - a < -l. \end{aligned}$$

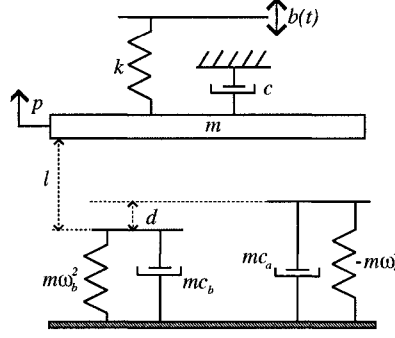


Figure 3.4 Model with the piecewise linear cantilever sample force interaction. When the mass is displaced in the negative direction, first it will encounter the attractive forces modeled by a damper and a negative spring. If the displacement of the mass exceeds l it will encounter repulsive forces modeled by a damper and a positive spring. The dampers account for the energy dissipation due to sample interaction.

$$\begin{aligned}
 h_{1r}(a, p_0, \varphi) &= 0 \text{ if } p_0 - a \geq -\ell + d & (3.21) \\
 &= \frac{a \cos \varphi \omega_a^2}{2 \pi} c_1 + \frac{a \sin \varphi \omega c_a}{2 \pi} c_1 \text{ if } -\ell \leq p_0 - a < -\ell + d \\
 &= \frac{a \cos \varphi \omega_a^2}{2 \pi} c_1 - \frac{a \cos \varphi \omega_b^2}{2 \pi} c_2 + \frac{a \sin \varphi \omega c_a}{2 \pi} c_1 + \frac{a \sin \varphi \omega c_b}{2 \pi} c_2 \\
 &\text{if } p_0 - a < -\ell.
 \end{aligned}$$

$$\begin{aligned}
 h_{1i}(a, p_0, \varphi) &= 0 \text{ if } p_0 - a \geq -\ell + d & (3.22) \\
 &= \frac{a \sin \varphi \omega_a^2}{2 \pi} c_1 - \frac{a \cos \varphi \omega c_a}{2 \pi} c_1 \text{ if } -\ell \leq p_0 - a < -\ell + d \\
 &= \frac{a \sin \varphi \omega_a^2}{2 \pi} c_1 - \frac{a \sin \varphi \omega_b^2}{2 \pi} c_2 - \frac{a \cos \varphi \omega c_a}{2 \pi} c_1 - \frac{a \cos \varphi \omega c_b}{2 \pi} c_2 \\
 &\text{if } p_0 - a < -\ell.
 \end{aligned}$$

with $c_1 = |s_1| \sqrt{(1 - s_1^2)} - \cos^{-1}(|s_1|)$, $c_2 = |s_2| \sqrt{(1 - s_2^2)} - \cos^{-1}(|s_2|)$, $s_1 = \frac{-\ell + d - p_0}{a}$, $s_2 = \frac{-\ell - p_0}{a}$.

Note that in the above identities ω_a^2 , ω_b^2 , c_a and c_b are the parameters of the model which appear linearly. This results in a tractable optimization problem (3.3). Also using the piecewise linear model for the non-linear interaction, closed-form expressions were obtained for the various power components involved in the power balance equation given by Equation (3.7). Note that we can split $\overline{P_{tip}}$ into the

average power dissipated due to the damper mc_a , $\overline{P_{att}}$ and the power dissipated due to the damper mc_b , $\overline{P_{rep}}$. $\overline{P_{att}}$ and $\overline{P_{rep}}$ are evaluated to be,

$$\begin{aligned}\overline{P_{att}} &= \frac{1}{2}c_a a^2 \omega^2 \left(\frac{\cos^{-1}(|s_1| - |s_1| \sqrt{1-s_1^2})}{\pi} \right), \\ \overline{P_{rep}} &= \frac{1}{2}c_b a^2 \omega^2 \left(\frac{\cos^{-1}(|s_2| - |s_2| \sqrt{1-s_2^2})}{\pi} \right).\end{aligned}\quad (3.23)$$

The power balance equation can be rewritten as

$$\overline{P_{in}} - \overline{P_{air}} = \overline{P_{att}} + \overline{P_{rep}}. \quad (3.24)$$

If the amplitude, phase and p_0 are measured experimentally, the zeroth and the first order Fourier coefficients h_0 and h_1 of the tip-sample interaction force h can be evaluated by solving the harmonic balance equations (Equations (3.9), (3.10) and (3.11)). This process can be repeated at various tip-sample separations. The values of h_0 and h_1 thus obtained together with Equations (3.20), (3.21) and (3.22) provide a tool for the estimation of the tip-sample interaction model parameters. Also $\overline{P_{in}}$ and $\overline{P_{air}}$ can be evaluated using Equations (3.12) and (3.13). Hence Equations (3.23) and (3.24) will form another set of tools for the analysis of experimental data.

3.2 Experimental results and discussion

Experiments were performed on silicon, mica, high density polyethylene and low density polyethylene. A Multi-Mode scanning probe microscope from Digital Instruments was used for experiments. Here one of the experiments performed on silicon is presented.

An atomic force microscope (Multi-Mode, Digital Instruments, Santa Barbara, CA) was operated in the tapping mode. A silicon cantilever of length 225 microns was used. The model parameters were evaluated by analyzing the cantilever response to thermal noise (see Ref. [28]). The parameters were identified to be, $\xi = 0.0038$, $\omega_0 = 2\pi \times 73881$ rad/sec, and $k = 4$ N/m. A sinusoidal voltage with its frequency equal to ω_0 was applied to the dither piezo. The sample (silicon wafer) initially was sufficiently far from the cantilever so that it did not affect the cantilever motion. Once the cantilever reached its steady state, the sample was slowly moved towards the vibrating cantilever by extending

the piezo. The motion of the cantilever tip at various values of the piezo extension, was recorded using HP 89410 Vector Signal Analyzer.

For the piece-wise tip-sample interaction model there are five parameters to be estimated namely the length of the attractive region d (the attractive region is where the phase difference is less than -90 degrees), the attractive and repulsive spring constants per unit mass, ω_a^2 and ω_b^2 and the damper values per unit mass, c_a and c_b . The estimation is based on data obtained by varying ℓ and by fixing the magnitude of forcing a_d and the frequency of the forcing at the first resonant frequency of the cantilever.

The first parameter estimated is the length of the attractive region, d . Note that the absolute tip-sample separation is not available experimentally. What can be measured is the photodiode output in volts (denoted by V_a) which is a measure of the vibration amplitude, a and the differential motion, Δl of the piezo-actuator which positions the sample. The assumption that the amplitude equals the tip-sample separation in the repulsive region is made. This is justified because the penetration of the tip into this region is small due to the very strong repulsive forces in most samples. From this assumption, $\frac{\Delta a}{\Delta l}$ equals one in the repulsive region where Δa is the change in amplitude and Δl is the change in the separation. Hence,

$$\frac{dV_a}{dl} \frac{da}{dV_a} = \frac{da}{dl} = 1. \quad (3.25)$$

Since $\frac{dV_a}{dl}$, which is the slope of the photodiode output Vs. the separation curve, can be obtained experimentally, $\frac{da}{dV_a}$ which is the sensitivity denoted by S can be calculated from Equation (3.25). Using S and the experimentally obtained value V_a , the amplitude a is obtained in nanometers. Again by the assumption that the tip extension into the repulsive region is negligible, the absolute tip-sample separation l is obtained from the relative separation by making the tip-sample separation and amplitude values to coincide in the repulsive region. The next step is to identify the minimum separation possible to keep the cantilever freely oscillating. Let this separation be l_0 . The freely vibrating amplitude a_0 when subtracted from l_0 gives d . The estimated value from the experimental data is 1.695nm.

The data points from the attractive region are used to estimate c_a using the power balance equation (3.7). Equation (3.7) is first used to obtain the value of $\overline{P_{tip}}$ which is equal to $\overline{P_{att}}$. The assumption that p_0 values are negligible compared to the amount by which the tip penetrates into the attractive region is made which is justified by the simulation data from Ref. [8]. Note that due to the small magnitude

of p_0 in typical tapping mode applications, it is difficult to measure p_0 . The linear relationship between the $\overline{P_{att}}$ and the c_a evident from Equation (3.23) is exploited to obtain a least square estimate of c_a . A value of $3e - 7\mu s^{-1}$ was obtained which is approximated by $0\mu s^{-1}$. Even though for this experimental data a c_a value of approximately zero was obtained, in other experiments on softer samples, higher values for the attractive region damper were obtained.

Once the parameter c_a has been estimated the harmonic balance equations can be used to estimate ω_a . There is a linear relationship between the real and imaginary parts of the Fourier coefficients of $h(p, \dot{p})$ and ω_a^2 (3.21) and (3.22). For the estimation of this parameter data points were chosen from the attractive region. p_0 is assumed to be zero. The harmonic balance equations given by Equations (3.10) and (3.11) were used to evaluate h_{1r} and h_{1i} directly from the amplitude and phase data. h_0 was not used for estimation since it is very sensitive to p_0 values. The problem is setup in the framework of least square estimation (see Equation (3.3) and Ref. [32]). The value of ω_a was estimated to be $0.31\mu s^{-1}$.

The estimation of attractive region related parameters is fairly robust since the effect of p_0 on them is negligible. However the strong dependence of c_b and ω_b on p_0 values makes the estimation of repulsive region parameters difficult. This dependence is due to the fact that the amount of penetration of the tip into the repulsive region is of the order of p_0 unlike in the attractive region.

A reasonable estimate for c_b can be obtained by observing the slope of the $\sin \varphi$ vs. a/a_0 plot in the repulsive region. The c_b value of $1.45\mu s^{-1}$ was fixed by comparing the slope of the simulation plots with that of the experimental plot.

Once c_b is fixed, the p_0 dependent term in the expression for P_{rep} can be estimated for each amplitude and phase value using the power balance equations ((3.7) and (3.23)). Now a similar procedure as that for the estimation of ω_a can be employed. The difference being that the estimation is done using data from the repulsive region. ω_b was obtained to be $2.7\mu s^{-1}$. Simulations show that a higher ω_b value is desirable. A value of $3.03\mu s^{-1}$ was found to be a good choice.

As mentioned earlier, the strong dependence of c_b and ω_b on p_0 makes their estimation more difficult. Moreover, c_b and ω_b values themselves are inter-related. Therefore trial and error iterations on the estimated values may be required for the repulsive region parameters. Also the assumption made that the amplitude equals l in the repulsive region may have an effect on the estimation of the repulsive region parameters. Hence the procedure outlined here is more suitable for the estimation of the attractive

region parameters.

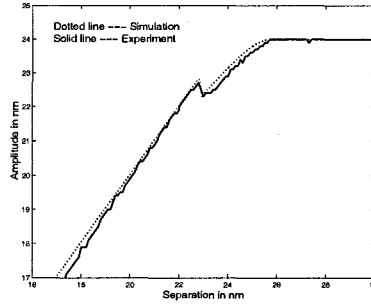


Figure 3.5 Using the estimated parameter values simulations are performed and the plots thus obtained are compared with those obtained through experiments. In this figure the amplitude is plotted against the separation. There is remarkable agreement between the two plots.

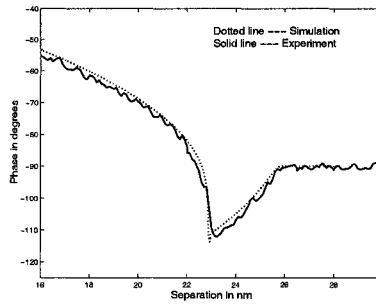


Figure 3.6 In this figure, the phase is plotted against the separation ℓ . Here also the two plots show good matching.

The estimated parameters were used to simulate the AFM operating in tapping mode. The corresponding results were compared with those obtained experimentally. The values of the various parameters used for simulations are $\omega_a = 0.31$ (attractive spring constant of 1.78 N/m), $\omega_b = 3.03$ (repulsive spring constant of 170.42 N/m), $c_a = 0\mu s^{-1}$ and $c_b = 1.45\mu s^{-1}$. The corresponding plots are shown in Figures 3.5, 3.6 and 3.7. It is evident from the plots that the model agrees with the experimental data. The most remarkable feature is that a simple model can capture the behavior of the tapping mode AFM. The fact that a piecewise linear model for tip-sample interaction suffices to predict the essential

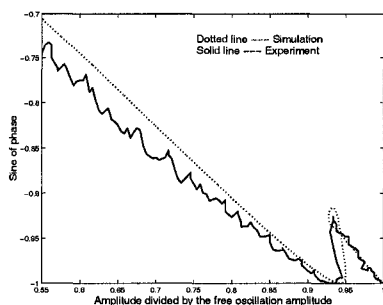


Figure 3.7 In this figure $\sin \varphi$ is plotted against a/a_0 . It can be seen that the model captures the linearity of this plot and even the reduction in the slope from one.

features of the tapping mode AFM also indicates the limitation of using tapping mode AFM to identify tip-sample interaction. As mentioned before the high frequency content of the tip-sample interaction force is filtered out by the cantilever thus making it unsuitable for identifying the finer features of the tip-sample potential curve.

3.3 Conclusions

The feedback perspective together with the harmonic and power balance tools provide an effective method to identify the tip-sample interaction. The feedback perspective with the cantilever viewed as a filter explains the sinusoidal nature of the steady state oscillations of the cantilever tip. The harmonic and power balance principles are applicable to a diverse range of tapping mode operating conditions. Note that in identifying the model used in this paper it was assumed that the tip oscillations are sinusoidal. Only the first harmonic data was utilized in identifying the model parameters. However, if it is possible to measure the higher harmonics of the cantilever oscillations then this data can be easily incorporated into the modeling process by utilizing (3.1) and (3.7). Note also that the harmonic and power balance methods are general tools which can be applied to a different model than provided here.

CHAPTER 4 The amplitude phase dynamics and fixed points in tapping mode AFM

In Chapters 2 and 3, a systems approach to the analysis of tapping-mode AFM dynamics was introduced where the tapping-mode operation was viewed as a feedback interconnection of a linear system (cantilever) with a nonlinear system (tip-sample interaction) which is forced sinusoidally. This analysis provided insights as to why in most operating conditions the cantilever settles down to a near sinusoidal periodic solution. Bounds were obtained for the higher harmonics in the steady state. But this analysis is not suitable to analyze the transient behavior of the tapping-mode dynamics and cannot explain the experimentally observed discontinuous jumps in the amplitude and phase at different values of cantilever-sample separation. Some of the early analytical efforts to explain these distinctly nonlinear phenomena are presented in [33], [34] and [35]. In one of the earliest attempts to characterize the transient behavior of tapping-mode operation, resorting to the averaging theorem, the amplitude phase dynamics were obtained (see [19]). Further the connection between the fixed points of the amplitude phase dynamics and those obtained using harmonic balance equations is presented.

In this chapter we provide new insights into the transient and nonlinear behavior of tapping-mode AFM. The emphasis is on tractable analytical methods and interaction models with an eye on potential applications in controller design based on amplitude dynamics and new modes of imaging. The focus of this work is different from the significant efforts to analyze the tapping-mode behavior in an elaborate manner using detailed descriptions for the forcing and interaction models (see [10]). In this chapter the oscillating cantilever influenced by the tip-sample interaction force is treated as a weakly nonlinear harmonic oscillator. Methods suggested by Bogoliubov and Mitropolskii (see [36] and [37]) are used to arrive at approximate solutions for the differential equations characterizing the cantilever dynamics. The amplitude and phase dynamic equations are derived. The multi-valued frequency response curves are obtained and a simple stability criterion is derived to analyze the stability of various fixed points. Insights are obtained on the regions of tip-sample potential probed during tapping-mode operation.

This study further demonstrates that a simple lumped parameter model captures the transient as well as steady state behavior.

4.1 Analysis

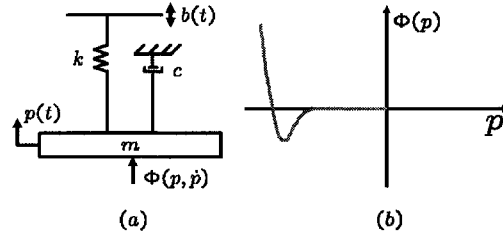


Figure 4.1 (a) The first mode approximation of the cantilever dynamics. m is the mass, k is the spring constant, c is the damper, p is the position of the tip of the cantilever, b is the forcing signal and Φ is the nonlinear tip-sample interaction force which is a function of the position and velocity. (b) Typical tip-sample interaction forces consist of long range weak attractive forces and short range strong repulsive forces. In the model introduced, the oscillating cantilever encounters the tip-sample interaction forces during the negative cycle of its oscillation.

A first mode approximation is typically sufficient to analyze the first harmonic of the cantilever oscillation. The first mode approximation model of the cantilever is depicted in Figure 4.1(a). A typical plot of the nonlinear tip-sample interaction force is shown in Figure 4.1(b). The dynamical equation of the tip of the cantilever, $p(t)$ is given by,

$$m\ddot{p} + c\dot{p} + kp = kb(t) + \Phi(p, \dot{p}) \quad (4.1)$$

where Φ is the force on the cantilever due to the sample and b describes the displacement of the base of the cantilever. m is the mass of the cantilever, k , the spring constant and c the damping coefficient. The tip encounters the tip-sample interaction forces towards the end of the negative cycle of the oscillation. Thus during most part of the oscillation cycle the tip does not interact with the sample. This motivates the analysis of tapping-mode dynamics using the asymptotic methods developed for weakly nonlinear systems. In the case of tapping-mode operation the nonlinear forces are significantly higher than the non-contact mode of operation of the AFM, another dynamic mode operation where the tip probes

only the attractive regime of the tip sample interaction. However the experimental results presented later validates the assumption that the cantilever sample system can be modeled as a weakly nonlinear oscillator even for the tapping-mode operation.

From Equation 4.1 it can be observed that in free air the cantilever oscillation is characterized by the parameters k and c since $\Phi = 0$. It is intuitive to assume that due to the tip sample interaction (when Φ is nonzero), the cantilever can still be thought of as a harmonic oscillator with a new effective k denoted by k_e and an effective c denoted by c_e which themselves are functions of the amplitude of oscillation. Furthermore intuitively an attractive tip-sample interaction should result in a lower k_e and a repulsive tip-sample interaction should result in a higher k_e compared to the original k . This process of approximating the original nonlinear dynamical equation by a second order linear differential equation in terms of $k_e(a)$ and $c_e(a)$ is called equivalent linearization. (See [37]).

4.1.1 Amplitude phase dynamics

Equation (4.1) can be recast as,

$$m\ddot{p} + kp = \epsilon \left(\frac{-c\dot{p} + \Phi(p, \dot{p})}{\epsilon} \right) + \epsilon \frac{mg(t)}{\epsilon} \quad (4.2)$$

where $g(t) = \frac{kb(t)}{m}$. This can be written as,

$$m\ddot{p} + kp = \epsilon f(p, \dot{p}) + \epsilon E \cos(\omega t) \quad (4.3)$$

where

$$f(p, \dot{p}) = \frac{-c\dot{p} + \Phi(p, \dot{p})}{\epsilon} \quad (4.4)$$

$$E \cos(\omega t) = \frac{mg(t)}{\epsilon} \quad (4.5)$$

Also if $g(t) = \gamma \cos \omega t$ (γ is the forcing amplitude), then $E = \frac{m\gamma}{\epsilon}$.

Assume that $p(t)$ is sinusoidal with an ‘‘amplitude’’, a and ‘‘phase’’, ϕ denoted by,

$$p(t) = a \cos(\omega t + \phi). \quad (4.6)$$

where

$$\dot{a} = -\delta_e(a)a - \epsilon \frac{E \sin \phi}{m(\omega_0 + \omega)} \quad (4.7)$$

$$\dot{\phi} = \omega_e(a) - \omega - \epsilon \frac{E \cos \phi}{ma(\omega_0 + \omega)}. \quad (4.8)$$

where,

$$\begin{aligned} \omega_e(a)^2 &= \frac{k_e(a)}{m} \\ &= \omega_0^2 + \frac{2}{a} \bar{\Phi}_c, \end{aligned} \quad (4.9)$$

$$\bar{\Phi}_c = \frac{1}{2\pi} \int_0^{2\pi} \frac{\Phi(a \cos \psi, -a\omega \sin \psi)}{m} \cos \psi d\psi$$

and

$$\begin{aligned} \delta_e(a) &= \frac{c_e(a)}{2m} \\ &= \xi\omega_0 + \frac{1}{a\omega} \bar{\Phi}_d, \end{aligned} \quad (4.10)$$

$$\bar{\Phi}_d = \frac{1}{2\pi} \int_0^{2\pi} \frac{\Phi(a \cos \psi, -a\omega \sin \psi)}{m} \sin \psi d\psi$$

Note that a and ϕ are the amplitude and phase typically referred to in the tapping-mode literature. It could be shown that Equation (4.6) satisfies Equation (4.3) with an accuracy of the order ϵ^2 when the forcing frequency ω is chosen such that $\omega_0^2 - \omega^2$ is of order ϵ (See [36]). The solution is equivalent to that of a linear system with damping coefficient $c_e(a)$ and spring constant $k_e(a)$ forced by a sinusoidal input at frequency ω . Correspondingly the equivalent resonant frequency is given by $\omega_e(a)$.

Let $\Delta\omega^2 = \frac{2}{a} \bar{\Phi}_c$ and $\Delta c_m = \frac{2}{a\omega} \bar{\Phi}_d$. Δc_m is a measure of the dissipative component of the tip-sample interaction since the energy dissipation in a harmonic oscillator is a function of the damping coefficient. Similarly $\Delta\omega^2$ is a measure of the conservative interaction and could take positive or negative values depending on $\bar{\Phi}_c$. If the sample is conservative, the dissipative component of the tip-sample interaction, $\bar{\Phi}_d = 0$ and $\bar{\Phi}_c$ does not depend on the phase ϕ .

For a fixed tip-sample separation and a fixed forcing frequency, in the transient state the amplitude and phase of the first harmonic of the cantilever oscillation evolve according to (4.7) and (4.8) which are nonlinear differential equations unlike in the absence of tip-sample interaction forces.

4.1.2 Steady state behavior

In the steady state the amplitude and phase of the first harmonic settles down to one of the fixed points of (4.7) and (4.8). The fixed points are given by,

$$-\delta_e(a)a - \epsilon \frac{E \sin \phi}{m(\omega_0 + \omega)} = 0 \quad (4.11)$$

$$\omega_e(a) - \omega - \epsilon \frac{E \cos \phi}{ma(\omega_0 + \omega)} = 0 \quad (4.12)$$

We obtain with an accuracy of ϵ^2 ,

$$2m\omega\delta_e(a)a = -\epsilon E \sin \phi \quad (4.13)$$

$$ma(\omega_e(a)^2 - \omega^2) = \epsilon E \cos \phi \quad (4.14)$$

From (4.13) and (4.14), we get

$$m^2 a^2 \{(\omega_e(a)^2 - \omega^2)^2 + 4\omega^2 \delta_e(a)^2\} = \epsilon^2 E^2 \quad (4.15)$$

Equation (4.15) gives the equilibrium points for the amplitude and phase dynamics. For each fixed l (hence a fixed tip-sample interaction potential) and ω , there could be more than one equilibrium point. This is an inherent feature of the nonlinear nature of tapping-mode operation. A purely linear analysis will not be able to explain experimental behavior which is due to this inherent nonlinear behavior. This is in contrast with the contact mode operation where the local nature of the tip-sample interaction forces permits a linear approximation.

Moreover let (a_0, ϕ_0) be an equilibrium point of the dynamical equations (4.7) and (4.8). Then the tip sample interaction force signal, $\Phi(t) = \Phi(a_0 \cos(\omega t + \phi_0), -a_0 \omega \sin(\omega t + \phi_0))$. Let Φ_1 be the first Fourier coefficient of the signal $\frac{\Phi(t)}{m}$. Then it can be shown that $\bar{\Phi}_c = \Phi_{1r} \cos \phi_0 + \Phi_{1i} \sin \phi_0$ and $\bar{\Phi}_d = \Phi_{1r} \sin \phi_0 - \Phi_{1i} \cos \phi_0$ where Φ_{1r} and Φ_{1i} are the real and imaginary parts of Φ_1 . This connects the conservative and dissipative components of the interaction force during steady state to the Fourier coefficients of the periodic tip-sample interaction force signal.

4.1.3 Conditions for the stability of fixed points

Due to the multiple equilibria, there are chances for discontinuous jumps in amplitude and phase when either the tip-sample separation l is varied for a fixed forcing frequency or when the forcing

frequency is varied for a fixed tip sample separation. These discontinuities are frequently observed in experiments and can be explained by analyzing the stability of the fixed points given by equation (4.15).

Let,

$$R(a, \phi) = -2\omega a \delta_e(a) - \frac{\epsilon E}{m} \sin \phi \quad (4.16)$$

$$S(a, \phi) = (\omega_e(a)^2 - \omega^2)a - \frac{\epsilon E}{m} \cos \phi \quad (4.17)$$

From equation (4.13) and (4.14), the fixed points are given by $R(a, \phi) = 0$ and $S(a, \phi) = 0$. If (a_0, ϕ_0) denote an equilibrium point, then the stability of the equilibrium point is given by the following two conditions,

$$a_0 R'_a(a_0, \phi_0) + S'_\phi(a_0, \phi_0) < 0 \quad (4.18)$$

$$R'_a(a_0, \phi_0) S'_\phi(a_0, \phi_0) - S'_a(a_0, \phi_0) R'_\phi(a_0, \phi_0) > 0 \quad (4.19)$$

Condition (4.18) is typically satisfied under usual laws of friction. Hence it suffices to see if (4.19) is satisfied.

From equation 4.16, if $R(a, \phi) = 0$, then

$$R'_a \frac{da}{d\omega} + R'_\phi \frac{d\phi}{d\omega} = -R'_\omega \quad (4.20)$$

Similarly from equation 4.17, if $S(a, \phi) = 0$, then

$$S'_a \frac{da}{d\omega} + S'_\phi \frac{d\phi}{d\omega} = -S'_\omega \quad (4.21)$$

From the above two equation,

$$(R'_a S'_\phi - S'_a R'_\phi) \frac{da}{d\omega} = S'_\omega R'_\phi - R'_\omega S'_\phi \quad (4.22)$$

Also from (4.16) and (4.17),

$$R'_\phi = \frac{-\epsilon E}{m} \cos \phi$$

$$R'_\omega = -2a \delta_e(a)$$

$$S'_\phi = \frac{\epsilon E}{m} \sin \phi$$

$$S'_\omega = -2\omega a$$

Hence the right hand side of equation (4.22) is given by

$$\begin{aligned} S'_\omega R'_\phi - R'_\omega S'_\phi &= (-2\omega a) \frac{-\epsilon E}{m} \cos \phi - (-2a\delta_e(a)) \frac{\epsilon E}{m} \sin \phi \\ &= 2a^2\omega\{(\omega_e(a))^2 - \omega^2\} - 2\delta_e(a)^2 \end{aligned}$$

From the above discussion we get,

$$(R'_a S'_\phi - S'_a R'_\phi) \frac{da}{d\omega} = 2a^2\omega\{\omega_e(a)^2 - (\omega^2 + 2\delta_e(a)^2)\} \quad (4.23)$$

Note that $R'_a S'_\phi - S'_a R'_\phi$ when evaluated at a fixed point (a_0, ϕ_0) is the quantity which should be always positive under the second stability condition given by equation 4.19. So (4.23) can be interpreted as the following. If one has a plot of the fixed point amplitudes versus the frequency of forcing, then a particular fixed point amplitude a_0 is stable if $\frac{da}{d\omega}|_{a=a_0}$ is greater than zero when $\omega_e(a)^2 > \omega^2 + 2\delta_e(a)^2$ and $\frac{da}{d\omega}|_{a=a_0}$ is less than zero when $\omega_e(a)^2 < \omega^2 + 2\delta_e(a)^2$. If the damping is very small, then a fixed point amplitude is stable if the slope at the point is positive for forcing frequencies below the equivalent resonant frequency and the slope is negative for forcing frequencies above the resonant frequency.

4.2 Experimental results and discussion

To verify the predictions of the theory presented in the previous section, experiments were performed on a *Digital Instruments* Multimode AFM. A silicon cantilever with natural frequency 335.4 kHz was chosen. The deflection signal was sampled at 5 MHz . The cantilever parameters were identified from the thermal noise response of the cantilever (see Ref. [28]). The quality factor was obtained to be 170.

The cantilever was oscillated at the frequency $f_0 = 335.4 \text{ kHz}$ to an amplitude of 24.25 nm . The sample (Highly Oriented Pyrolytic Graphite (HOPG)) was moved towards the freely oscillating cantilever and then away. If the position of the tip $p(t)$ is assumed to be $a \cos(\omega t + \vartheta)$ where $\omega = \omega_0 = 2\pi f_0$, then the resulting amplitude, a is plotted against the tip-sample separation l (see Figure 4.4(f)). The approach and retraction of the sample is performed sufficiently slow so that the amplitude and phase evolving according to (4.7) and (4.8) settle to an equilibrium amplitude and phase for a particular tip-sample separation. Note that there is some ambiguity about the absolute tip-sample separation which will be addressed when a model is introduced for the tip-sample interaction.

Using the identification schemes described in Chapter 3, ω_a , ω_b , c_a and d were estimated for the experimental data. $\omega_a = 0.765 \mu s^{-1}$, $\omega_b = 3 \mu s^{-1}$, $c_a = 0.017 \mu s^{-1}$ and $d = 2.55 \text{ nm}$. Using these parameters simulation were performed and the resulting amplitude versus separation data is compared with the experimental results in Figure 4.2(a).

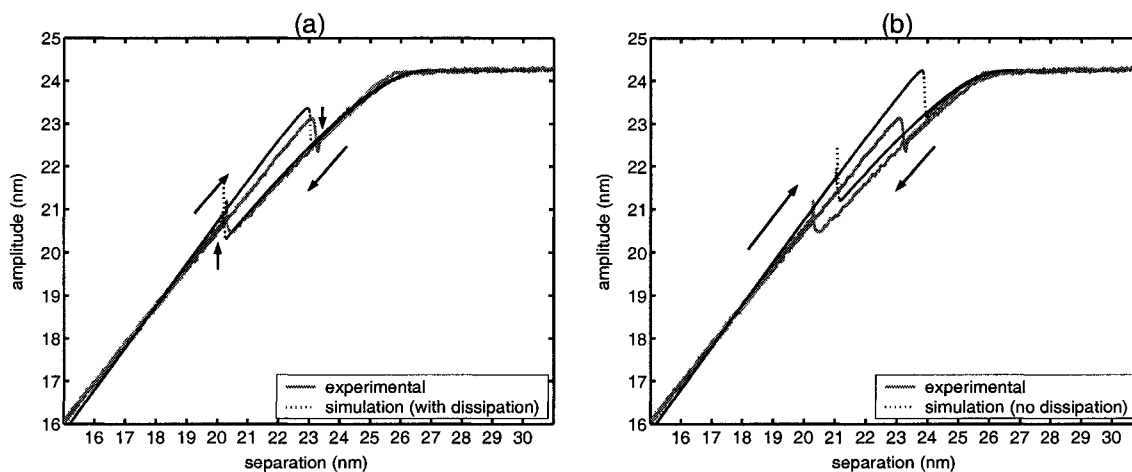


Figure 4.2 (a) The amplitude versus tip-sample separation curve is obtained using the interaction model and is compared with that obtained from experiments. There is remarkable agreement between the two. (b) To simplify the analysis, the sample is assumed to be conservative or non-dissipative. The simulation results still agree with the experimental results qualitatively and show the discontinuities.

Note that there is remarkable similarity between the experimental data and those obtained through simulations. For simplifying the future discussion, the damping term c_a is assumed to be zero in the model. This brings about some discrepancy with the experimental data as shown in Figure 4.2(b). However there is excellent qualitative match showing the discontinuous jumps. This assumption on conservativeness is to simplify the analysis and a similar analysis could be performed for the non conservative case.

Figure 4.3 depicts the multi-valued frequency response plot for a tip-sample separation of 23 nm . It also shows the equivalent resonant frequency $\omega_e(a)$ plotted as a function of the amplitude. For the forcing frequency which is equal to the free resonant frequency of the cantilever, there are three fixed points **X**, **Y** and **Z**. From the stability criteria developed earlier, the fixed points amplitudes, **X** and **Z**

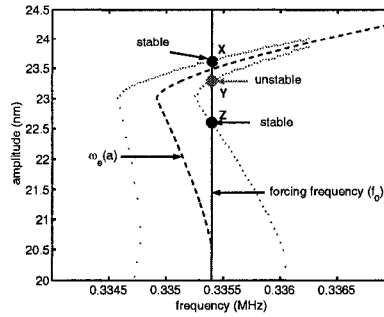


Figure 4.3 For a tip-sample separation of $l = 23 \text{ nm}$, the multi-valued frequency response curve is shown. For a forcing frequency of f_0 , there are three possible fixed point amplitudes. From the stability criteria two of the three are stable.

are stable whereas **Y** is unstable.

The amplitude versus separation plot can be explained in terms of the multi-valued frequency response plots, the resulting multiple equilibrium amplitudes and their stability.

Figure 4.4(a)-(e) depict the multi-valued amplitude-frequency plots for various tip-sample separations characterized by l . In these plots The forcing frequency is depicted by the vertical line at 335.4 KHz and the value of l that denotes the distance at which the repulsive region begins is indicated by the horizontal line. In Figure 4.4(f) the amplitude-separation curve is shown. In Figure 4.4(a) the cantilever is freely oscillating with $l = 30 \text{ nm}$. In the approach phase the cantilever is brought closer to the sample. As l is reduced to 24.5 nm (see Figure 4.4(b)), there is only one possible fixed point denoted by the point **B**. Its also evident that the cantilever does not explore the repulsive region as the amplitude is smaller than l . As the separation is further reduced with $l = 23.9 \text{ nm}$ there are two possible fixed points **C** and **J**. However, the amplitude takes the value corresponding to **C** as the operating region is in its basin of attraction. With further reduction of l to 23 nm and later to 21.1 nm , the amplitude takes the value corresponding to **D** and **E** respectively. Any further reduction of the tip-sample separation leads to the scenario where there is only one intersection point of the vertical line with the amplitude-frequency plot. Thus the amplitude jumps to **F**. Note that throughout the traversal **ABCDE** the tip does not interact with the repulsive part of the regime (l is greater than the amplitude). At **F** the amplitude is bigger than l and thus the tip does explore the repulsive part at this operating condition.

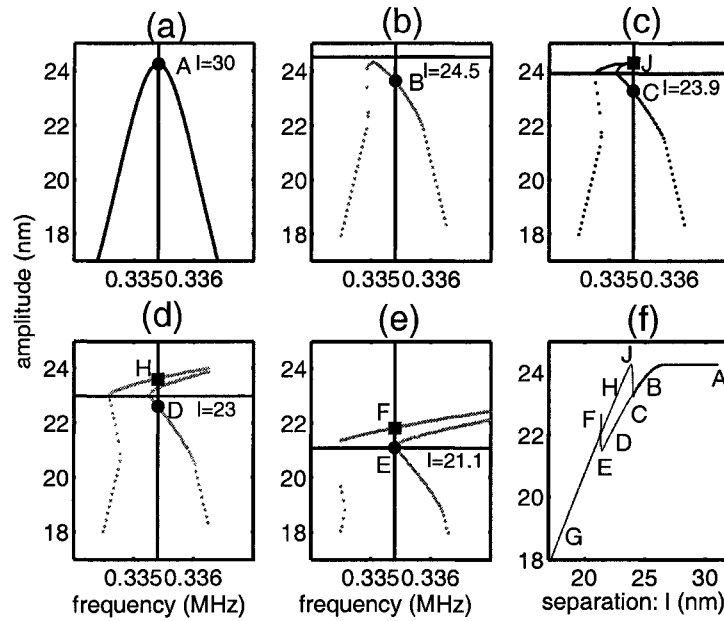


Figure 4.4 (a)-(e) For different tip-sample separations, the multi-valued frequency response curves are obtained by solving Equation (4.15) (f) The discontinuities in the amplitude versus separation plot can be explained using the multi-valued frequency response plots, the resulting multiple equilibrium amplitudes and their stability

Any further reduction of l leads to a single fixed point scenario and the path FG is traversed by the tip (see Figure 4.4(f)).

In the retract phase, first the path GF is traversed. In this phase at $l = 23nm$ and $23.9nm$ the amplitude settles to the value corresponding to points H and J respectively. As the tip is further retracted to a value slightly greater than $l = 23.9nm$ the tip has to take the value close to the one marked by C. Throughout the traversal GFHJ the tip explores the repulsive part of the interaction. Thus in the approach phase the path traversed is ABCDEFG where during ABCDE the tip does not interact with the repulsive region and in the retract phase the tip traverses the path GFHJCBA where during CBA the tip again does not interact with the repulsive part.

Thus we have obtained a detailed explanation of the amplitude-separation behavior typically observed and these observations validate the theory developed in the earlier sections.

4.3 Conclusions

In the tapping-mode operation of the AFM, the cantilever tip traverses a wide regime of the non-linear tip-sample interaction forces and hence a linear analysis is not sufficient to delineate the salient features. However since the oscillating tip encounters the nonlinear sample interaction forces only for a small fraction of the total oscillation time, averaging methods can be used to analyze the tapping-mode dynamics. Correspondingly an approximate solution is obtained for the cantilever oscillation where the amplitude and phase of the first harmonic evolve according to a nonlinear differential equation. The transient behavior of tapping-mode operation is captured by these equations. The steady state values for amplitude and phase are given by the fixed points of these amplitude phase dynamical equations. With a simple tip-sample interaction model and the stability of these fixed points some of the experimentally observed behavior of tapping-mode operation is explained. It is surprising that a piecewise linear interaction and an analysis which assumes the tip-sample system to be weakly nonlinear (which appears to be simplistic for tapping-mode operation where the interaction forces are quite significant) explains the experimental behavior in a remarkable manner.

PART II: ROBUST BROADBAND NANOPositionING

The growth of research in the areas of nanotechnology and nanoscience has imposed new demands on nanopositioning where the needs for higher precision at increasing bandwidth is presenting new challenges. The primary requirements of nanopositioning are ultra high precision, high bandwidth and good robustness. In the current applications of nanotechnology, the specifications for positioning are in the nano and angstrom regime. In scanning probe technologies molecular and atomic forces are routinely probed that warrants positioning in the molecular and atomic dimensions. High bandwidth is essential for high throughput primarily when nanopositioners serve as scanners or sample positioners in imaging applications. High bandwidth is also essential while probing short time scale events. The uncertainty in the device parameters and operating conditions warrants high robustness for these devices.

This part of the thesis presents a new control design paradigm for robust broadband nanopositioning. It consists of two design methodologies. A design for bandwidth and resolution and a design for robustness. A procedure for a systematic design, analysis and development of nanopositioning devices is prescribed. In this effort we have used many tools from modern control theory to model devices and to quantify device resolution, bandwidth and robustness. The merits of the paradigm are demonstrated through the design and implementation of two nanopositioning stages.

The nanopositioning devices presented here are actuated by piezoelectric materials. The crystal lattices of these materials deform on application of an electric field. These deformations are used for accurate positioning. The advantages of these actuators are several: they provide repeatable sub-nanometer motion, do not have backlash, do not suffer from wear and tear, require very little maintenance, have fast response times, can generate large forces, are operable in a wide range of temperatures, and are not affected by magnetic fields. However, their use is hindered by nonlinear effects like hysteresis and creep. Hysteretic effects, in which the piezo motion does not vary linearly with the applied voltage

are prominent especially in large traversals and can be as high as 10-15% of the path covered. Creep, in which the piezo drifts independent of the applied voltage, becomes noticeable when positioning is required over long time periods. There have been many efforts to counter the nonlinear effects which include design changes in the open-loop implementation such as: using 'harder' piezo ceramics which have smaller nonlinear effects at the cost of travel range (see Ref. [38]); replacing voltage control by charge control (see Ref. [39]) which achieves lower hysteresis but leads to more creep, lesser travel and lower positioning bandwidth; post processing data obtained from actuations designed for pre-specified trajectories (see Ref. [40]), which are not useful for applications that need real time compensations; and compensating for the adverse nonlinear effects by a careful modeling of the nonlinearities which achieves good results but is sensitive to the precision of the model used (see Ref. [41]). In comparison to the open loop architecture there are fewer feedback design schemes for nanopositioning. In Ref. [42], the design of a feedback controller using an optical sensor attachment to enhance the performance of an Atomic Force Microscope scanner is described. Similar efforts to improve the imaging speeds of the AFM are made in Ref. [43].

In Chapter 5, through the design and implementation of a one-dimensional nanopositioner, the design for high bandwidth and resolution is demonstrated. In this design, robustness aspects are not explicitly addressed. However in large range nanopositioners nonlinear effects are significant. Moreover they are operated in diverse operating conditions. Hence robustness is a critical criterion in the design of controllers for these nanopositioners. Moreover there are specific tracking requirements like zero steady state error ramp tracking which is one of the primary needs in many modes of the nanopositioner operation. Designs which emphasize on robustness are demonstrated using the design and implementation of a two dimensional nanopositioner in Chapter 6. Tools from modern robust control like Glover-McFarlane \mathcal{H}_∞ loop shaping techniques and robust \mathcal{H}_∞ designs are utilized in achieving these objectives. The Glover-McFarlane loop shaping scheme provides a framework to robustify any existing design with a quantifiable compromise on the performance. In this methodology it is possible to separate the designing task of meeting performance specifications (like bandwidth and resolution) and robustness into two modular steps. Such a framework is appropriate for the nanopositioning system design as is evident from the comparative results with the existing designs that are presented.

An immediate application of these design schemes is in the two dimensional positioning of sample

in scanning probe microscopes like the Atomic Force Microscope (AFM). These design methodologies are further applied to the control of the atomic force microscope operating in the contact mode. The imaging problem is essentially a nanopositioning problem where the micro-cantilever serves as the position sensor. This is presented in Chapter 7. Parts of the research presented in these chapters have appeared in [44], [45] and [46].

CHAPTER 5 Design methodology for bandwidth and resolution

The controller design paradigm for robust broadband nanopositioning consists of two methodologies. In this chapter through the design and implementation of a one dimensional nanopositioning device the design methodology for bandwidth and resolution is presented. This work illustrates the ineffectiveness of the traditional proportional-integral architecture used predominantly by the nanopositioning community and provides a basis for such a judgement. In contrast we show how the modern control framework allows for translating the performance specifications like bandwidth and resolution into an optimization problem that can be solved to obtain a controller meeting the specifications (if such a controller exists) in a methodical and streamlined manner. The implemented controller and the resulting nanopositioning device has considerably higher bandwidth (130 Hz , in contrast to less than 3 Hz with the optimized PI control law).

The nanopositioning device has a piezoelectric actuator and a Linear Variable Differential Transformer (LVDT) as the position sensor. The device described here is an independent unit, and is not a modification or an enhancement of an already existing device. The piezo-actuator used here is a stack-piezo, in contrast to the piezoelectric tube commonly used as scanners in most commercial scanning probe microscopes. The stack piezos are cheaper and yield much larger forces and displacements when compared to tube piezos. In contrast to the tube piezo nanopositioner, the stack piezo based design has less coupling in the different directions of positioning. However the nonlinear effects which are associated with piezo electric actuation are considerably more pronounced for the stack piezos. This along with the positioner dynamics which has non-minimum phase zeros pose the primary challenges for controller design.

This chapter is organized as follows. The description of the device and its design is presented in Section 5.1. The identification of this model and the design of the feedback controllers are presented in Sections 5.2 and 5.3 respectively. The resulting improvement in the performance of the device and its

complete characterization in terms of its bandwidth, resolution, linearity and travel range is presented in Section 5.4. The comparison of performances with and without controllers is also presented in this section.

5.1 Device description

A schematic of the device is shown in Figure 5.1. It consists of a flexure stage with a sample holder, an Atomic Force Microscope (AFM) head, an actuation system, a detection system and a control system. The base plate (see Figure 5.2(a)) is $20\text{ cm} \times 20\text{ cm} \times 5\text{ cm}$ and is made of steel. From its center protrudes a cylindrical block for holding the sample. This part of the base plate that seats the sample holder executes the motion relative to its periphery. This motion is obtained by the serpentine spring design (see Figure 5.3) where design grooves (about $150\mu\text{m}$ wide) are cut in the base plate, making it possible for the flexure stage to move relative to the frame. The top plate sits on the base plate and is of similar dimensions as the base plate. It provides support for an Atomic Force Microscope (AFM) head above the sample (see Figure 5.2(b)). The AFM could be used for calibration and imaging purposes as illustrated later in this chapter. Note that there is no actuation in the vertical direction; so the AFM is operating in what is known as “constant-height” mode.

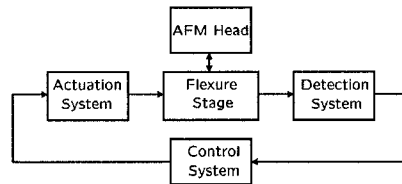


Figure 5.1 A schematic block diagram of the device.

The actuation system consists of a voltage amplifier and a piezo-stack arrangement shown in Figure 5.4(a). This arrangement sits in the slot adjacent to the flexure stage (see Figure 5.2(a)). The amplified voltage signal applied across the piezo-stack leads to its deformation which imparts the motion to the flexure stage. The input to the amplifier (which has a gain of -15) is restricted to be negative and to be less than 10 V in magnitude since the piezo-stack saturates beyond this limit. The piezo stacks are at an angle $\alpha \approx 7.5$ degrees (see Figure 5.4(b)). This arrangement, besides providing sufficient force

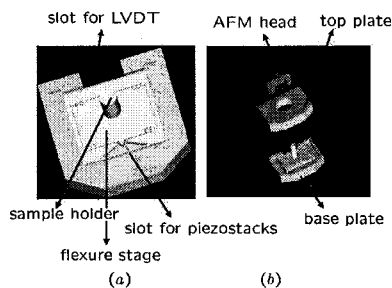


Figure 5.2 (a) The base plate of the flexure stage. (b) The exploded view of the flexure and evaluation stages.

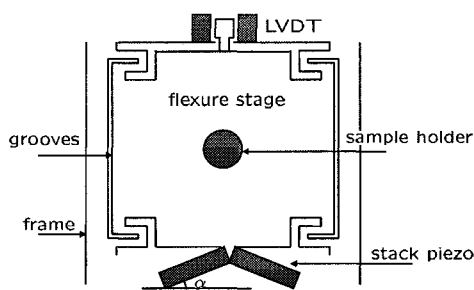


Figure 5.3 A schematic to describe the serpentine design for supporting the flexure stage. This figure is illustrative and not drawn to scale.

to the flexure stage, also achieves a mechanical gain of $1/\sin(\alpha)$. If the piezo-stacks have different gains, there is a possibility that the flexure stage is pushed out of the plane. The out-of-plane motion of the plate can however be detected by the AFM head. Experiments show that there was no appreciable out-of-plane motion.

The detection system consists of an LVDT and associated demodulation circuit. It has a resolution of 2 \AA over 1 kHz bandwidth. The working principle of the LVDT is shown in Figure 5.5(a). The excitation signal is a sinusoidal voltage with 14 V amplitude and 10 kHz frequency. It induces in the two secondary coils a sinusoidal voltage having the same frequency as excitation; however, the amplitude of the output varies with the position of the core. The core is attached to the moving flexure stage and the coils are attached to the stationary frame (see Fig 5.3). When the secondaries are connected

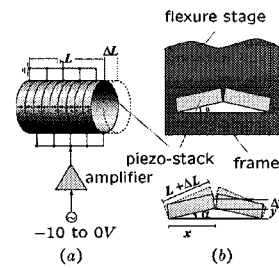


Figure 5.4 The piezo actuation stage: (a) actuation of a piezo-stack. (b) arrangement of the piezo-stacks.

in opposition, there is a null position whose corresponding output is zero. In the apparatus, this null position has been adjusted so that it corresponds to the position of the flexure stage when an input of -5 V is given to the actuation system. Motion of the core from this null causes a larger mutual inductance on one coil and smaller on the other coil and the amplitude of the resulting output signal is a linear function of the core position for a considerable range on either side of the null. This amplitude modulated voltage signal is passed through a demodulation circuit to retrieve its amplitude. Thus, the output signal from the demodulation circuit is proportional to the motion of the flexure stage.

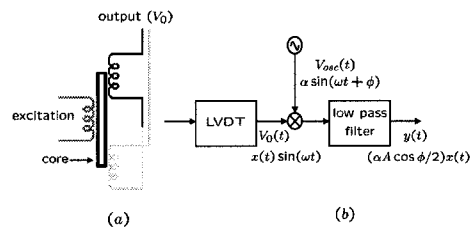


Figure 5.5 The detection stage: (a) working principle of LVDT. (b) demodulation of the amplitude modulated signal.

A block diagram of the control system is shown in Figure 5.6. In the control algorithm, a reference signal (or the command signal) to be tracked is modified by a pre-filter to regulate the bandwidth of the device by removing the high frequency content in the signal, and/or appropriately shaping the signal to achieve better tracking. The design of the pre-filters and control laws is described in Section 5.3. These

laws were implemented on a Texas Instruments C44 digital signal processor.

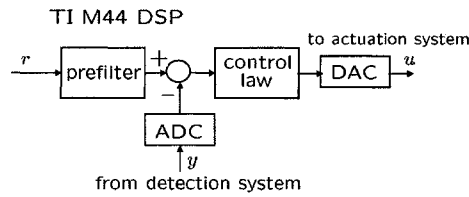


Figure 5.6 A schematic block diagram of the control system

We denote the input to the actuation system by u , the demodulated output signal from the LVDT by y and the system comprising the actuation, flexure and detection stages by G . Also, we refer to u as the piezo-input, y as the LVDT-output and G as the plant. Figure 5.7 is a block diagram of the closed loop system. Here r represents the reference or the command signal; e denotes the error signal, the difference between the reference and the output signals; and K stands for the controller transfer function. Also, we represent the open loop transfer function GK by L ; the sensitivity function (the transfer function from r to e) by S ; and the complimentary sensitivity function (the transfer function from n to y) by T .

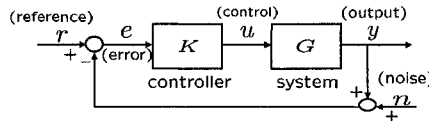


Figure 5.7 A schematic block diagram of the closed loop system.

5.2 Identification

The modeling of the device was done using a black-box identification technique where a specific point in the operating range of the device was chosen (where its behavior is approximately linear) and a model of the device is obtained at this point by studying its frequency response over a pre-specified bandwidth. For this purpose, we used a HP 3563A signal analyzer, which gave a series of sinusoidal inputs, $u = -5 + A \sin(\omega t)$ (V), with frequencies spanning a bandwidth of 2 kHz. An offset of -5 V

was given to operate the device about the null position. The amplitude, A , of the signals was chosen to be less than 50 mV so that the piezo response was approximately linear. The frequency response of the device at this operating point is shown by the Bode plot (dashed lines) in Figure 5.8. A fourth order non minimum phase transfer function:

$$G(s) = \frac{9.7 \times 10^4 (s - (7.2 \pm 7.4i) \times 10^3)}{(s + (1.9 \pm 4.5i) \times 10^3)(s + (1.2 \pm 15.2i) \times 10^2)}$$

yielded a good fit to this data. Figure 5.8 shows the comparison between the frequency response data and the one simulated from the model, $G(s)$. The right hand plane (RHP) zeros of $G(s)$ need to be noted as they pose limitations on performance as described later.

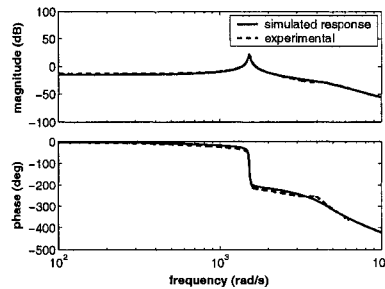


Figure 5.8 A comparison of experimentally obtained and simulated frequency responses of the plant.

5.3 Control design

The model inferred for the device at the null operating point was employed to design the feedback laws. The primary objective of the control design is to achieve precise tracking of arbitrary input signals with high bandwidth. The feedback laws were constrained to provide control signals that were negative and within actuator saturation limits (-10 V to 0 V). Besides these implementation constraints, the presence of RHP zeros impose fundamental constraints. From classical root locus analysis (see [47, 48]) we know that as the feedback gain increases, the closed loop poles migrate to open loop zeroes, which implies high gain instability of the system. Hence high gain feedback laws are not applicable. They also impose a fundamental limit on the achievable bandwidth of the closed loop system. A complex pair of RHP zeroes, $z_{1,2} = x \pm iy$ (as in this case $z_{1,2} = (1.72 \pm 7.36i) \times 10^3$), the “ideal”

controller leads to the following sensitivity function (see [49, 48]),

$$S = \frac{4xs}{(s+x+jy)(s+x-jy)}.$$

By the above criteria the achievable bandwidth (the frequency at which $|S(j\omega)|$ crosses $-3dB$ from below) is approximately 415 Hz for the system. This controller is “ideal” in the sense, for a unit step reference $r(t)$, it generates an input $u(t)$ which minimizes the integral square tracking error:

$$\int_0^{\infty} |y(t) - r(t)|^2 dt.$$

Note that such a controller might not be realizable (see [49, 48]).

In industry, it is a common practice to design proportional (P) or proportional-integral (PI) controllers. In the next part of the chapter we show that this architecture is not suitable for the nanopositioning device presented.

Traditional control architecture: Proportional (P) and Proportional-Integral (PI) controller design

From the analysis of the root-locus plot of the open loop system, it is seen that the closed loop system is unstable for feedback gains greater than 0.1674 (see Figure 5.9). As is evident in Figure 5.10, the gains at low frequency of the closed loop transfer function (for different proportional controllers ($0 < k < 0.1674$)) are very low and hence the performance of the device is far from satisfactory.

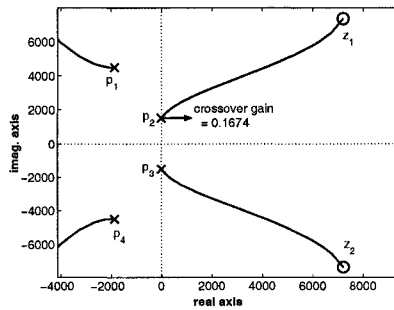


Figure 5.9 The root-locus of the open loop transfer function, G .

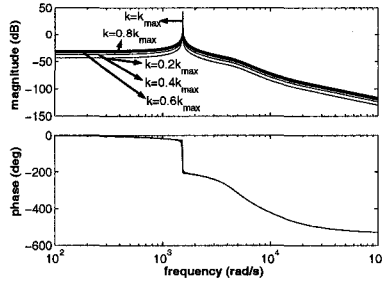


Figure 5.10 The bode plots of closed loop transfer function with different proportional controllers.

If we assume a PI architecture ($k_p + k_i/s$) for the controller, we can determine the regions in the k_p - k_i plane which guarantee closed loop stability (see Figure 5.11(a)). It should be noted that the region (in the k_p - k_i plane) that gives high bandwidth (see plot (d)) is the region with low gain margin (see plot (c)). Thus a trade-off between robustness and performance has to be decided. We chose $k_p = 0.01$ and $k_i = 75$, which guarantee a gain margin of 1.57 and a phase margin of 89° and the corresponding bandwidth of the closed loop transfer function is 2.12 Hz . Note that the selection of the controller parameters requires extensive tuning over the parameter space to achieve higher bandwidth with reasonable robustness margins. This controller was implemented and Figure 5.12 shows tracking of a 1 Hz triangular wave. We see that there is good agreement between the reference and the LVDT-output signals for this input although the system has problems accurately tracking the sharp turn-around.

It should be noted that the bandwidth ($< 3 \text{ Hz}$) attained with the PI architecture (the bandwidth can be slightly improved at the expense of robustness) is much less than the “ideal” bandwidth ($\approx 415 \text{ Hz}$) as described in the previous section. This low bandwidth can be explained from the following simplified analysis. We approximate the plant G by considering only its slow modes $x + iy = (0.12 \pm 15.2i) \times 10^2$ and ignoring the fast modes ($s + (1.9 \pm 4.5i) \times 10^3$). This results in a third order closed loop system whose characteristic polynomial is given by

$$s^3 + 2\delta\omega_n s^2 + (k_p + \omega_n^2)s + k_i,$$

where $\omega_n \triangleq \sqrt{x^2 + y^2} = 15.2 \text{ rad/s}$ and $\delta \triangleq x/\omega_n = 8 \times 10^{-3}$. For this system it can be shown that the bandwidth is in the order of $\delta\omega_n = 12 \text{ rad/s} = 1.9 \text{ Hz}$. This is in close agreement with the

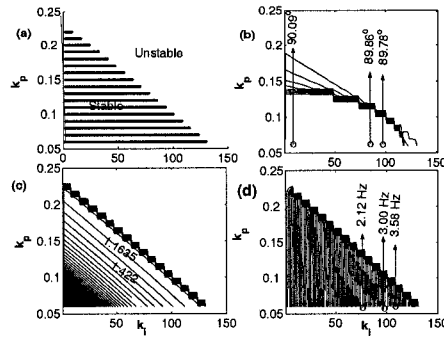


Figure 5.11 (a) The region in k_i - k_p plane that guarantees closed loop stability. The contour plots showing (b) the phase margins (c) the gain margins (d) the bandwidth of the closed loop systems corresponding to different points in the k_i - k_p plane.

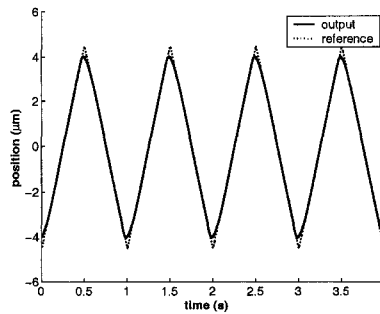


Figure 5.12 Tracking of 1 Hz triangular signal with PI controller.

numerical analysis presented above.

The main reason for the failure of the PI design is that the poles of the closed loop system (even for the third order system) cannot be placed arbitrarily by choosing k_p and k_i . A higher order controller is needed to have full freedom in the placement of poles. Design of a higher order controller requires tuning over a larger set of parameters. Significant effort and technical expertise is needed for this.

\mathcal{H}_∞ controller design

The main advantage of using this design is that it includes the objectives of tracking bandwidth and resolution in the problem formulation. More precisely, the control law is obtained as a solution to an

optimization problem which incorporates the performance objectives like bandwidth and resolution in its cost function. This eliminates the tedious task of tuning the gains in the PI architecture (as illustrated later even the optimally tuned gains fail to yield acceptable performance).

The first step towards \mathcal{H}_∞ control design is to form the generalized plant, P . In the system (see Figure 5.13 (a)), the exogenous input w is the reference signal r , the control input is u and the measured output z is the error signal e . In order to reflect the performance objectives and physical constraints, the regulated outputs were chosen to be the weighted transfer function, $z_1 = W_1 e$, the weighted system output, $z_2 = W_2 y$ and the weighted control input, $z_3 = W_3 u$. The transfer function from w to z_1 is the weighted sensitivity function, $W_1 S$, which characterizes the performance objective of good tracking; the transfer function from $w = n$ to z_2 is the complementary sensitivity function, whose minimization ensures low control gains at high frequencies, and the transfer function from w to z_3 is KS , which measures the control effort. It is also used to impose the control signals to be within saturation limits. The weighting functions W_i , $i = 1, 2$ and 3 are used to scale these closed loop transfer functions to specify the frequency information of the performance objectives and system limitations. The inverse of the weighting functions is an upper bound (up to a constant scaling factor) on the transfer function it is used to scale [48]. The transfer function, W_1 , is chosen such that it has high gains at low frequencies and low gains at high frequencies (see Figure 5.14). This scaling ensures that the optimal feedback law is such that the sensitivity function is small at low frequencies, thus guaranteeing good tracking at the concerned frequencies. More precisely, W_1 was chosen to be a first order transfer function,

$$W_1(s) = \frac{0.1667s + 2827}{s + 2.827}.$$

This transfer function is designed so that its inverse (an approximate upper bound on the sensitivity function) has a gain of 0.1% at low frequencies ($< 1 \text{ Hz}$) and a gain of $\approx 5\%$ around 200 Hz .

The weighting function W_1 puts a lower bound on the bandwidth of the closed loop system but does not allow us to specify the roll off of the open loop system to prevent high frequency noise amplification and to limit the bandwidth to be below Nyquist frequency. As already mentioned, piezo-actuators do not have any backlash or friction and therefore have very fine resolution. The resolution of the device, therefore, depends on the experimental environment and it is limited by thermal and electronic noise. In any closed loop framework the high resolution of the piezo-actuators may be compromised due the introduction of the sensor noise (in this case the LVDT) into the system. Clearly this effect is absent

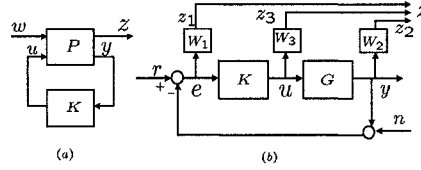


Figure 5.13 (a) The generalized plant framework. (b) The closed loop system with regulated outputs.

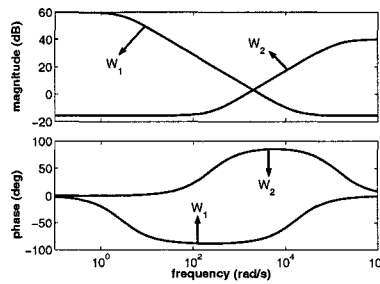


Figure 5.14 The weighting transfer functions

in the open loop case. In the \mathcal{H}_∞ paradigm these concerns of sensor noise rejection are reflected by introducing a weighted measure of the complementary sensitivity function, T , (which is the transfer function between the noise and the position y). In this case this weight was chosen to be

$$W_2 = \frac{s + 235.6}{0.01s + 1414}$$

which has high gains at high frequencies (note that noise is in the high frequency region). There is another interesting interpretation of this weighting function. It decides the resolution of the device. Resolution is defined as the variance of the output signal y , when the device is solely driven by the noise n ; i.e., resolution is equal to the variance of Tn . Thus, W_2 that guarantees lower roll off frequencies gives finer resolutions. In this way, the trade-off between conflicting design requirements of high bandwidth tracking (characterized by low S , $T \approx 1$) and fine resolutions (characterized by low T) are translated to the design of weighting transfer functions W_1 and W_2 . The transfer function, KS was scaled by a constant weighting $W_3 = 0.1$, to restrict the magnitude of the input signals such that they are within the saturation limits. This weighting constant gives control signals that are at most six times

the reference signals.

In summary, the regulated outputs are given by

$$z = \begin{bmatrix} z_1 \\ z_2 \\ z_3 \end{bmatrix} = \begin{bmatrix} W_1(r - Gu) \\ W_2Gu \\ W_3u \end{bmatrix},$$

and the generalized plant, P is described by

$$\begin{bmatrix} z \\ v \end{bmatrix} = \underbrace{\begin{bmatrix} \begin{bmatrix} W_1 & -W_1G \\ 0 & W_2G \\ 0 & W_3 \end{bmatrix} \\ \begin{bmatrix} I & -G \end{bmatrix} \end{bmatrix}}_{=P} \begin{bmatrix} r \\ u \end{bmatrix}.$$

In practice it is computationally simpler to design a suboptimal controller (i.e. one that is close to the optimal with respect to the \mathcal{H}_∞ norm). In particular, for any $\gamma > \gamma_{opt} > 0$ we can find a controller transfer function K such that

$$\left\| \begin{bmatrix} W_1S \\ W_2T \\ W_3KS \end{bmatrix} \right\|_\infty < \gamma$$

where γ_{opt} is the optimal value. The controller was designed (using the function, *hinfsyn* in Matlab) for $\gamma = 2.415$ and the weighting functions described above. The following sixth order controller transfer function, $K(s)$ was obtained with a DC gain of 2.2599×10^3 , its poles at -1.14959×10^7 , -1.4137×10^5 , -5.6432×10^3 , -2.8274 and $(-1.5676 \pm 5.8438i) \times 10^3$, and its zeroes at -1.4137×10^5 , $(-1.8647 \pm 4.4958i) \times 10^3$ and $-1.1713 \times 10^1 \pm 1.5205i \times 10^3$.

The controller, the sensitivity, the complementary sensitivity function and KS transfer functions are shown in Figure 5.15. The bandwidth of the system (from the sensitivity transfer function) is found to be 138 Hz. It should be noted that this is an enormous improvement over the PI controller. Also, this controller provides a gain margin of 2.57 and a phase margin of 62.3° as opposed to the values of 1.57 and 89° in the PI controller. This shows that the robustness is considerably better with \mathcal{H}_∞ controller. Note that in this design methodology unlike the one described in Chapter 6, robustness is not explicitly addressed in the design formulation.

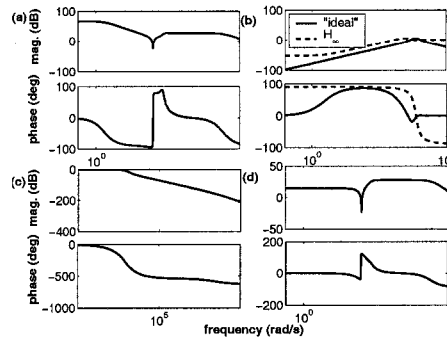


Figure 5.15 Closed loop transfer functions: (a)controller (b) sensitivity (c) complementary sensitivity (d) KS

The designed \mathcal{H}_∞ controller was implemented and the resulting closed loop bandwidth was similar to that obtained theoretically. The performance of the \mathcal{H}_∞ controller is significantly better than the PI controller (see Figure 5.16).

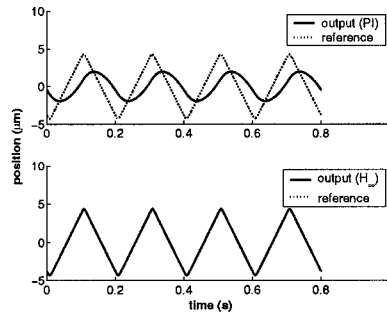


Figure 5.16 A comparison of the performance of the closed loop system with (a) PI controller (b) \mathcal{H}_∞ controller.

Figure 5.17 shows the performance of this controller for a 25, 50 and 100 Hz triangular and 100 Hz reference signals. It can be seen that the closed loop system tracks well the 25 Hz and 50 Hz signals (see plots (a) and (b)). The mismatch in the case of the 100 Hz (in (c)) signal is due to the accentuation of higher modes of the triangular wave. In contrast, the 100 Hz sinusoidal signal shown in (d) does not have higher harmonics and the closed loop system shows much improvement in its tracking. In addition to the above advantages the design process was capable of incorporating

the engineering specifications in a streamlined manner in contrast to the often ad-hoc way of tuning parameters in the PI design.

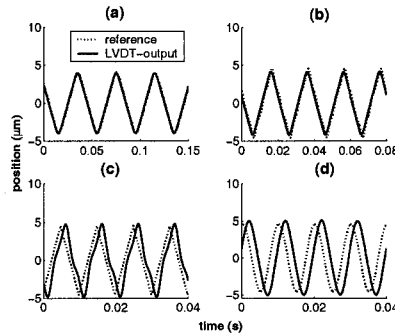


Figure 5.17 Tracking of (a) 25 Hz (b) 50 Hz (c) 100 Hz triangular waves and (d) 100 Hz sinusoidal wave using the \mathcal{H}_∞ controller.

5.4 Characterization of the device

In this section, we characterize the closed loop and the open loop device in terms of its resolution, bandwidth, and range. We also provide the comparison between PI and \mathcal{H}_∞ designs. First, the device was calibrated using a calibration sample which had 180 nm high grooves every 5 μm . This grid was placed on the sample holder and probed by the AFM head. A triangular input of amplitude 2 V was given and the resulting LVDT output showed the presence of 7.26 grooves. This implies the device has a static sensitivity of 18.15 $\mu m/V$. It was seen that the input voltage of approximately 4 V can be given without reaching the limits of the actuator. This guarantees a travel range of 70 μm .

Elimination of nonlinear effects

The positioning precision of the piezo-actuators is significantly reduced due to nonlinear effects such as hysteresis, drift and creep. Hysteresis effects are significant when the sensors are used for relatively long ranges. Therefore open loop piezo-actuators are typically operated in linear ranges to avoid positioning effects. However, with \mathcal{H}_∞ design, these nonlinear effects are compensated and thus the closed loop device shows minimal hysteresis. To study this, we first plotted hysteresis curves by operating the device in open loop configuration and then compared them with the curves obtained by

repeating the experiment in the closed loop configuration. Input signals (less than 1 Hz triangular pulses) of increasing amplitudes (1 V to 4 V) were given in open loop configuration and the corresponding output signals recorded. The output vs reference plots are given in (see Figure 5.19(a)). It is observed that the hysteresis effects are dominant at higher amplitudes (longer travels). The hysteresis is quantified numerically in terms of maximum input (or output) hysteresis given as a percentage of the full scale (see Figure 5.18). The maximum output hysteresis varies from $0.74\mu\text{m}$ to $4.93\mu\text{m}$ (7.2% to 10% of corresponding travels) and the maximum input hysteresis varies from 0.14 V to 0.73 V (5.8% to 7.6% of drive inputs). A similar plot (see Figure 5.19(b)) obtained for the closed loop configuration shows that the \mathcal{H}_∞ design virtually eliminates all hysteretic effects. In this case, the travel length is $45\mu\text{m}$ and the maximum output hysteresis was significantly reduced to 62.3 nm (0.14%) and the corresponding maximum input hysteresis was reduced to 2 mV (0.07%).

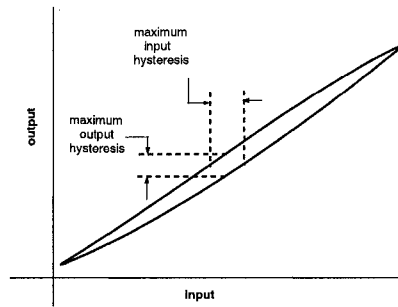


Figure 5.18 Numerical quantification of hysteresis.

Creep is another undesirable nonlinear effect common in piezoelectric actuators. It is related to the effect of the applied voltage on the remnant polarization of the piezo ceramics. If the operating voltage of a (open loop) piezo-actuator is increased (decreased), the remnant polarization (piezo gain) continues to increase (decrease), manifesting itself in a slow creep (positive or negative) after the voltage change is complete. This effect is approximately described by the equation,

$$y(t) \approx y_0(1 + \gamma \log(t/t_0)),$$

where t_0 is the time at which the creep effect is discernible, y_0 is the value of the signal at t_0 and γ is a constant, called the creep factor, that characterizes this nonlinear effect. To measure this effect, we studied the steady state step response of the device in open and closed loop configurations. The

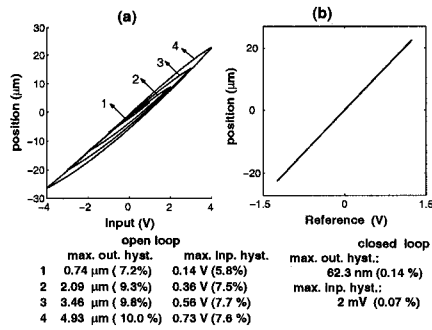


Figure 5.19 Hysteresis in (a) the open loop configuration, (b) its elimination in the closed loop configuration.

response $y(t)$ in the open loop was found to approximately satisfy the creep law with a creep factor of 0.55. The same experiment conducted in the \mathcal{H}_∞ closed loop (see Figure 5.20) shows that the feedback laws virtually eliminates this effect and the system tracks the reference signal.

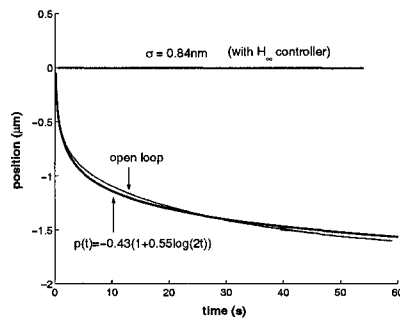


Figure 5.20 The elimination of creep using \mathcal{H}_∞ controller.

A significant adverse effect of the nonlinearities is that of non repeatability. This was seen clearly in the calibration experiment described in the previous section. In this case, the grooves that were observed when travelling in one direction were not concomitant with those in the other direction. This is shown in Figure 5.21(a). The corresponding hysteresis curve is shown in (c). These effects were removed with \mathcal{H}_∞ design and in (b), we see that the grooves in the forward and reverse directions are aligned with each other (The PI performance is not provided as the scan speed was well beyond the PI bandwidth). The corresponding hysteresis plot is shown in (d). The mismatch in the open loop is more

clearly seen in Figure 5.22(b), where the image obtained in one direction is positioned behind the one obtained in the other direction for the sake of comparison. In (c), the near perfect match with the \mathcal{H}_∞ design is demonstrated. This non repeatability can lead to gross errors when the images are averaged over many scans (say to remove the effects of noise). For example, the plot in Figure 5.23 (bottom-left) shows the scan of grooves obtained by averaging over the forward and the backward directions. It can be seen that it has no semblance with the actual calibration sample (top). However, the averaged scan in the closed loop case, (bottom-right), matches very well with the sample.

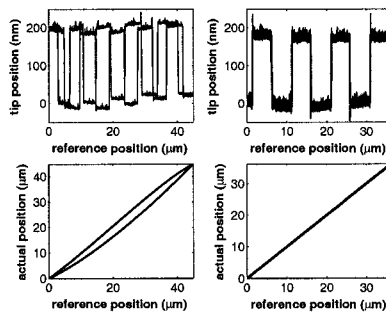


Figure 5.21 Evaluation stage results: (a),(c) mismatch in the position of grooves between the forward and the backward traverses in the open loop and the corresponding hysteresis cycle. (b),(d) a good match in the closed loop configuration and the corresponding hysteresis cycle.

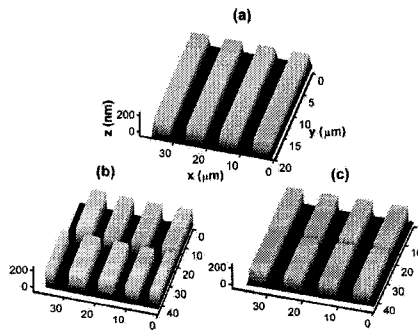


Figure 5.22 (a) The reference (calibration sample) geometry. (b) The mismatch in the position of grooves between the forward and the backward traverses in the open loop. (c) a good match in the closed loop configuration.

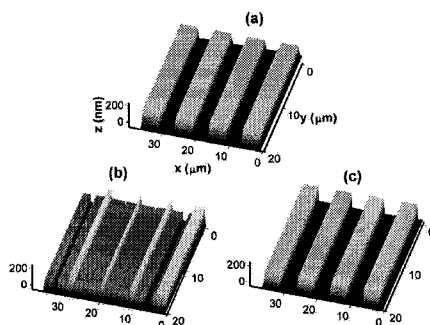


Figure 5.23 (a) The calibration sample (top) (b) Its distorted image obtained by averaged data in the open loop configuration (bottom-left). (c) Its faithful image obtained by averaging in the closed loop (bottom-right).

5.5 Conclusions

Most of the traditional nanopositioners operate in open loop with possible compensation for nonlinearities like hysteresis. In closed loop designs traditional controllers like proportional integral controllers are widely used. The traditional controllers are inadequate to meet the bandwidth and resolution requirements that arise in nanopositioning applications. Moreover it is difficult to incorporate bandwidth and resolution requirements in a streamlined fashion in classical design schemes. Design of those controllers involve searching and tuning over a wide range of parameters and significant technical expertise is needed.

In the presented design methodology, the bandwidth and resolution requirements can be incorporated in a straight forward fashion in terms of sensitivity and complementary sensitivity functions. Engineering requirements on bandwidth and resolution are translated to requirements on the shapes of sensitivity and complementary sensitivity functions. By formulating the control design problem as an optimization problem it is possible to know if the design requirements are achievable by the positioner. This is particularly useful in the design stage of the nanopositioner. If the design requirements on bandwidth and resolution are achievable, the corresponding controller is obtained as a solution to the optimization problem.

The experimental results on the nanopositioner presented in this chapter clearly demonstrate the efficacy of this approach. There is significant improvement in bandwidth and resolution compared to classical design schemes.

In this design, robustness is not explicitly addressed. In most nanopositioners robustness is a key requirement primarily due the nonlinear characteristics of piezo actuation. Moreover nanopositioners are operated under different operating conditions for varied applications. In Chapter 6, design schemes to address the robustness aspect of nanopositioning is presented.

CHAPTER 6 Design methodology for robustness

In this chapter, a large range nanopositioner capable of positioning in two dimensions is presented. Flexure stages serve as the sample positioners and is actuated by piezoelectric actuators. The primary emphasis on the control design in this chapter is to achieve robustness of the closed loop device. In these large range scanners, the robustness requirement is motivated by many reasons: the repeated use of flexure stages leads to time varying changes in their stiffness - thus having uncertain pole locations; the unmodeled nonlinear effects are significant; and these devices are used in diverse operating conditions. Here we present two *robust* control designs motivated by different requirements. First, we present the Glover-McFarlane \mathcal{H}_∞ design with the goal of increasing robustness of *existing industrial* control designs without significantly compromising device performance. Many of the existing controllers are designed to achieve specific tracking requirements (such as zero steady state tracking) commonly needed imaging applications. The Glover-McFarlane loop shaping scheme provides a framework to robustify any existing design with a quantifiable compromise on the performance. In this methodology it is possible to separate the designing task of meeting performance specifications (such as tracking requirements, bandwidth and resolution) and robustness into two modular steps. We demonstrate the robustness induced by this design with a little compromise (sometimes improvement) on performance by comparing results with the existing designs. Second, we present robust \mathcal{H}_∞ design to *simultaneously* achieve performance and robustness in these devices for those applications where there is no specific tracking requirement and a characterization of uncertainty is available a priori.

The chapter is organized in the following way. In Section 6.1, a description of the device is given. This is followed by frequency domain based system identification described in Section 6.2. The control design and the experimental results are presented in Section 6.3. The device characterization is presented in Section 6.4.

6.1 Device description

The nanopositioning system studied in this article is described in Figure 6.1 (developed in *Asylum Research*, Santa Barbara, California).

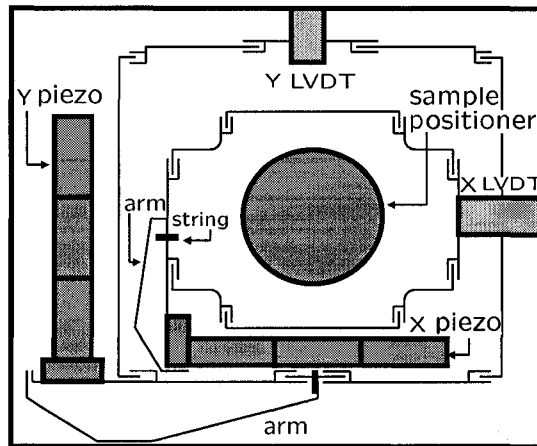


Figure 6.1 A schematic of the nanopositioning device. There are two stages 'X' and 'Y' with 'X' sitting on top of 'Y'. Each stage is actuated by piezo-electric stacks and the resulting motion is sensed by LVDT sensors.

The flexure stage consists of two stages, 'X' seated on 'Y' (see Figure 6.1), with the sample holder on the 'X' stage. Each stage, by virtue of the serpentine spring design deforms under the application of force providing motion. These forces are generated by stack-piezos. As shown in Figure 6.1, there are three piezo-actuators in series for each axis. The motion of each stage is measured by the respective LVDT (Linear Variable Differential Transformer) and the associated demodulation circuit.

Besides being cheaper, the piezostacks have longer travel ranges compared to their cylindrical counterparts used more often in industry. These actuators lead to a travel range of approximately $100\ \mu\text{m}$ in both directions. The modified LVDT sensors used in this design have resolution in the order of $2\ \text{\AA}$ over $1\ \text{kHz}$ bandwidth which gives a vast advantage over more common optical sensors. The control laws are implemented on a *Analog Devices ADSP-21160* digital signal processor.

6.2 Identification

The complex structural design makes physical modeling of the device difficult. The model has been inferred using frequency response based techniques. The device is viewed as a two-input two-output system where the low voltage signals to the ‘X’ and ‘Y’ amplifiers (u_x and u_y) are the inputs and the motion of ‘X’ and ‘Y’ stages measured by the respective LVDT sensors, (x and y) are the outputs. This results in four input-output transfer functions, $G_{ij}, i, j \in \{x, y\}$. Here G_{ij} represents the transfer function from the input u_j to the output i . Figure 6.2 depicts the different blocks constituting the mapping between u_x and x .

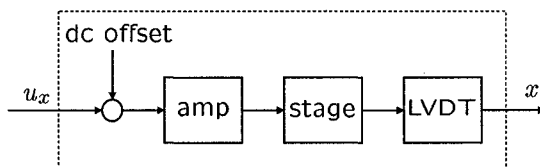


Figure 6.2 u_x is the input to the amplifier which drives the stack piezo. The motion of the stage is sensed using an LVDT sensor whose output is x .

These maps can be assumed to be linear over a small region of operation about an operating point. A DC offset is applied to maintain a particular operating point (see Figure 6.2). The nominal operating point is chosen to be the *null position*, i.e. where the LVDT outputs read zero. Frequency responses are obtained about this operating point to obtain the nominal model (that maps $(u_x \ u_y)'$ into $(x \ y)'$) denoted by,

$$G = \begin{bmatrix} G_{xx} & G_{xy} \\ G_{yx} & G_{yy} \end{bmatrix}.$$

The responses are obtained using a *HP3536A* signal analyzer with 10 mV amplitude forcing and averaged over 200 measurements for a bandwidth of 1.25 kHz . Note that the forcing signal is small since the total input range is 10 V which corresponds to around $100 \text{ }\mu\text{m}$ travel range. Rational transfer functions are fit to responses. $G_{xx}(s)$ is a 7th order transfer function with the first resonance frequency at approximately 390 Hz . $G_{yy}(s)$ is 5th order with the first resonance frequency at 235 Hz . $G_{xx}(s)$, $G_{yx}(s)$ and $G_{yy}(s)$ are given below,

$$G_{xx}(s) = \frac{4.29 \times 10^{10}(s^2 + 631.2s + 9.4 \times 10^6)(s^2 + 638.8s + 4.5 \times 10^7)}{(s^2 + 178.2s + 6 \times 10^6)(s^2 + 412.3s + 1.6 \times 10^7)(s^2 + 209.7s + 5.6 \times 10^7)(s + 5818)}$$

$$G_{yx}(s) = \frac{-28.7(s - 5094)}{s^2 + 94.7s + 6.48 \times 10^6},$$

$$G_{yy}(s) = \frac{1.38 \times 10^{10}(s^2 + 1006s + 1.625 \times 10^7)}{(s + 6165)(s^2 + 101.7s + 2.18 \times 10^6)(s^2 + 708.1s + 2.7 \times 10^7)}.$$

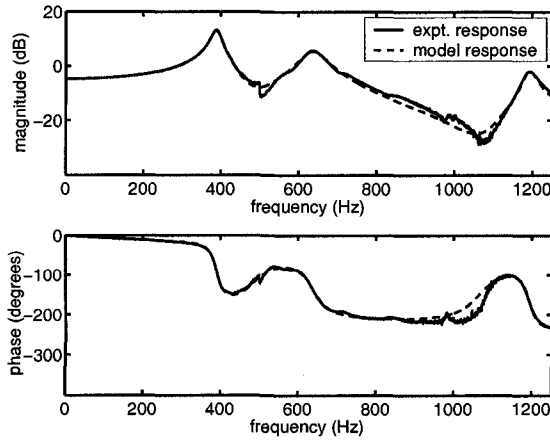


Figure 6.3 Experimental frequency response is compared with the response of the model $G_{xx}(s)$.

G_{xy} and G_{yx} were found to be relatively small compared to G_{xx} and G_{yy} . Figures 6.3, 6.4 show how well the frequency responses obtained from these models agree with those obtained experimentally.

In order to further validate the models, step responses obtained experimentally are compared with the model responses. In Figure 6.5, a comparison of the step responses shows agreement between the experimental and model response for G_{xx} . The slight variation in gain could be attributed to hysteresis since the models are obtained using low amplitude (10 mV) signals whereas the step response in this experiment has a magnitude of around 200 mV.

Due to the piezo-actuation and the changing flexure dynamics these models were found to vary with different operating points and with time. To study the variation of these models with respect to

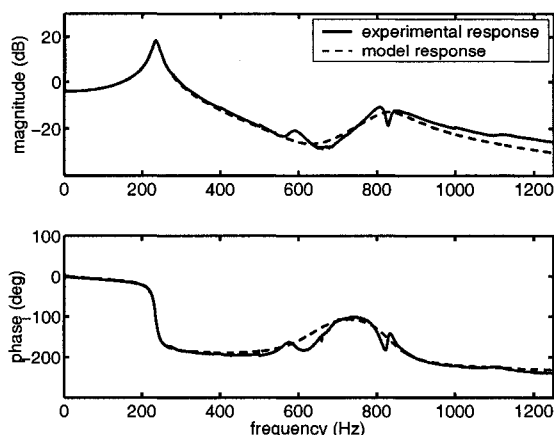


Figure 6.4 Experimental frequency response is compared with the response of the nominal model $G_{yy}(s)$.

operating points, frequency responses are obtained at different operating points. A considerable variation was observed in these responses. Figure 6.6 shows the responses obtained at different operating points spread over a range of approximately $80 \mu m$, separated by approximately $20 \mu m$. Further it was observed that the frequency response at the same operating point varies when obtained at different times. This time varying uncertainty typically manifests as a change in the resonance locations. This is again an artifact of the flexure stage. Repeated cycling at significant strains (like in the case of the nanopositioner discussed in this chapter) could lead to changes in the Young's modulus of the flexure through effects such as strain hardening. This translates to changes in the spring constants and hence the change in the pole positions. The mass of the objects which are being positioned could also affect the frequency response of the positioner. However due to the relatively large mass of the flexure stage, this effect is not very pronounced. All these uncertainties make robustness of the closed loop system a key requirement.

6.3 Controller design and implementation

In the design of the feedback laws, the coupling transfer functions G_{xy} and G_{yx} are neglected in order to simplify the design process. This is reasonable as the coupling terms are relatively small. The mode of operation of this device is such that higher bandwidth requirements are made on the smaller

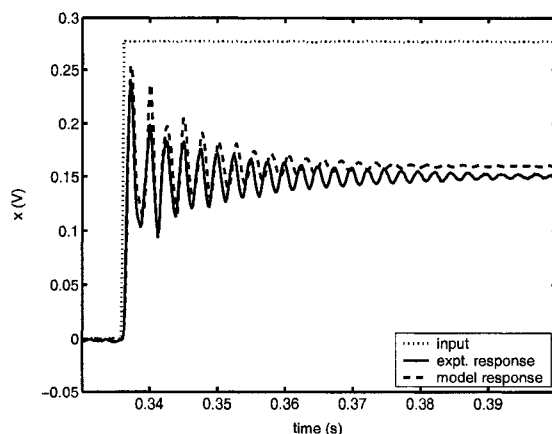


Figure 6.5 The experimental step response is compared with the response of G_{xx}

stage ‘X’ where as ‘Y’ stage is made to move relatively slow. Hence, there is a greater emphasis on the control designs for the ‘X’ stage which is presented in this chapter. Designs were also done for G_{yy} and the resulting diagonal controllers were implemented, the details of which are not presented in this chapter. Figure 6.7 shows the unity feedback loop for the ‘X’ stage.

In this figure, x_r is the reference signal, the output signal is x and K_{xx} is the control transfer function that needs to be designed. The error e_x is given by, $e_x = x_r - x = Sx_r - Tn_x$, where S is the sensitivity function and T is the complementary sensitivity function. The closed loop bandwidth of the nano-positioner is defined to be the frequency at which $|S(j\omega)|$ crosses -3 dB. Since T is the transfer function between e and the noise n , the complementary sensitivity function is a measure of the resolution. As mentioned earlier, the primary emphasis of this chapter is on robustness. $\|T\|_\infty$ and $\|S\|_\infty$ are good measures of the robustness of device (for appropriate uncertainty classes) and will be frequently used in subsequent discussions for comparing the robustness of various design schemes. In particular these values give a lower bound on the gain and phase margins. Lower bounds on gain and phase margins given in terms of $\|S\|_\infty$ are $GM = \|S\|_\infty / (\|S\|_\infty - 1)$ and $PM = 2\sin^{-1}(1/2\|S\|_\infty)$ (see Ref. [48]).

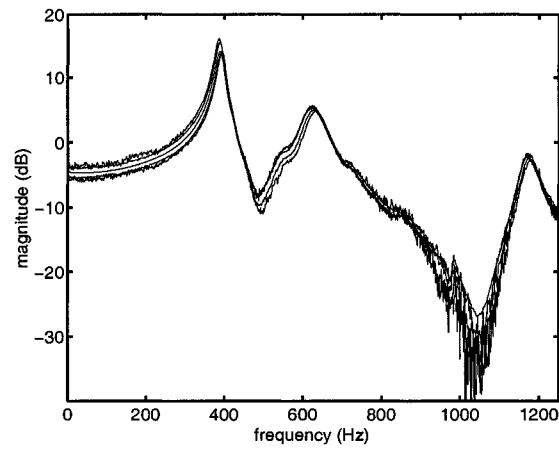


Figure 6.6 Experimentally obtained frequency responses at different operating regions for the X stage.

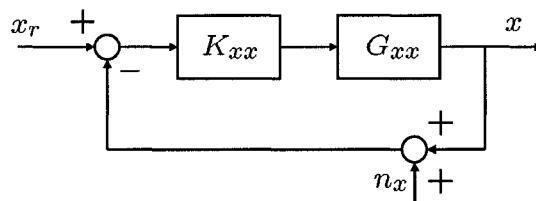


Figure 6.7 A unity feedback configuration for G_{xx} .

Control designs

For robust nanopositioning, two approaches are employed. In the first approach Glover McFarlane robustifying controllers are designed for existing controllers typically employed in nano-positioners. In the second approach robust \mathcal{H}_∞ designs are employed to meet the bandwidth and tracking requirements along with the required robustness.

6.3.0.1 Robustification of existing controllers

Proportional double integral (PII) control design

Proportional integral (PI) and proportional double integral (PII) controllers are the most common forms of controllers currently used for nanopositioning in the scanning-probe industry. Their popularity stems from the fact that they are simple to implement. Moreover an attractive feature of these controllers is that they can track ramp signals (common in imaging applications) with zero steady state errors. The PII controller has the structure $k_p + k_i/s + k_{ii}/s^2$. Here a PII design is presented which has been obtained after considerable search and tuning over the parameter space. It is given by $K_{pii}(s) = \frac{0.001s^2 + 450s + 10^5}{s^2}$. A plot of $S(j\omega)$ is shown in Figure 6.8. Besides having a low closed loop bandwidth of 31 Hz, this design has poor robustness properties. The $\|S\|_\infty$ for K_{pii} is 15.5 dB which is highly unsatisfactory and leads to sustained oscillations and instability while performing large range scans.

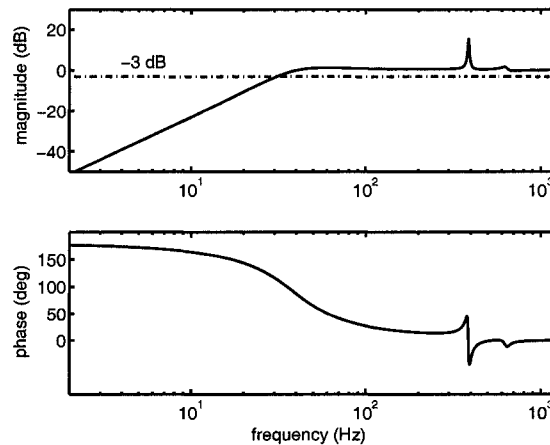


Figure 6.8 The bode plot of the sensitivity function is shown for a PII controller. The peaks in the magnitude plot indicate lack of robustness.

The PII controller was implemented and Figure 6.9 shows the tracking of 1 Hz and 5 Hz triangular waves. The tracking errors at turn around points are large since these contain higher harmonics which the device does not track. However, this is not a significant problem as the data corresponding to this region is discarded in typical imaging applications. But it is important that in the mid regions, the

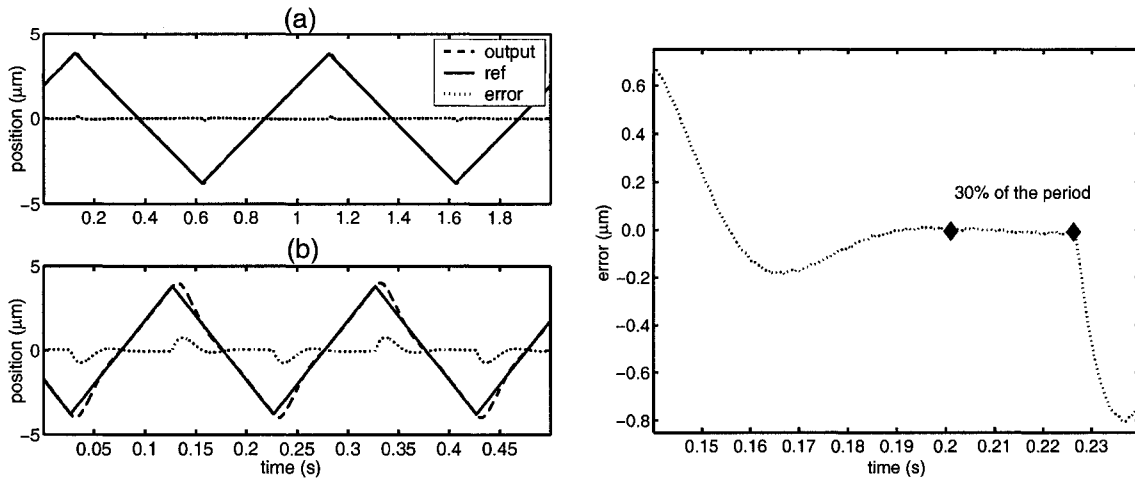


Figure 6.9 This figure shows the tracking of triangular reference signals using K_{pii} . (a) The tracking of a 1 Hz triangular signal is shown. (b) At 5 Hz, oscillatory behavior is observed. (c) This reduces the region of the trajectory which can be used for scanning purposes.

triangular wave is tracked satisfactorily. The 5 Hz tracking is unsatisfactory as the error is substantial over the whole trajectory. Figure 6.9 shows that the usable region of the trajectory is only 30% of the total period. The oscillatory behavior is due to the peaks present in $|S(j\omega)|$ (see Figure 6.8). Due to the low phase margin, attempts to introduce a low pass filter within the loop to improve the resolution results in instability. Moreover it is commonly observed that the PII controller goes unstable or starts showing oscillatory behavior while scanning over large scan ranges.

Glover-McFarlane control design

The PII designs are non-robust and they fail to achieve large closed loop bandwidths. Moreover, the designs are tedious requiring tuning over multiple parameters. These parameters are designed to shape the open loop transfer function $L = GK$ so that it has high gains at low frequencies and low gains at high frequencies. The resulting high gains at low frequencies imply better tracking of reference signals and the low gains at high frequencies give better device resolution by ensuring noise attenuation in the feedback signals. Moreover the PII controllers ensure that the device tracks ramp signals with zero steady state error. However, these designs do not account for uncertainties in the plant model

and therefore do not guarantee robustness. These control laws are highly sensitive to these model uncertainties (as seen from the large values of $\|S\|_\infty$) and therefore the closed loop performance in actual experiment deviates considerably from that predicted by the design.

The elegant control design introduced by Glover and McFarlane (see Ref. [50] and Ref. [51]) addresses both the performance and robustness requirements. In this design, the model uncertainties are included as perturbations to the nominal model and the robustness is guaranteed by ensuring that the stability specifications are satisfied for the *worst-case* uncertainty. A remarkable feature of this design is that it achieves robustness with marginal reduction in performance. In fact, it is able to quantify the reduction by determining explicit bounds on how much it changes the loop gains at low and high frequencies. This design process consists of two steps:

1. Design for performance: In this step, a shaping transfer function K_s is designed to meet the performance requirements like high loop gain in low frequencies and low loop gain in high frequencies. At this stage the requirements for robustness and even stability are not considered. In the design presented in this chapter, K_s is set equal to PII/PIID controllers. This is done to retain the closed loop property of tracking ramp signals with zero steady state error. Another reason is the prevalent use of such controllers in nanopositioning to realize performance specifications.
2. Design of a robustifying controller: In this step, a robustifying controller K_r is obtained which gives good robustness properties to the closed loop system obtained from the shaped plant $G_s = K_s G_{xx}$ of the previous step.

More specifically let $G_s = \frac{N}{M}$ be the normalized coprime factorization of the nominal shaped plant. The normalized coprime factor uncertainty characterization is given by,

$$\left\{ \frac{N + \Delta_N}{M + \Delta_M} : \left\| \begin{bmatrix} \Delta_N & \Delta_M \end{bmatrix} \right\| \leq \epsilon \right\},$$

The robustifying controller should stabilize all the plants belonging to the above set for a specified ϵ . For a shaping controller K_s , the maximum possible ϵ , ϵ_{max} can be calculated a priori as shown below. The robustness margin ϵ is chosen to be slightly less than ϵ_{max} .

The following steps yield the optimal controller that assume a state space model (A, B, C, D) available for the transfer function $G_s = K_s G_{xx}$.

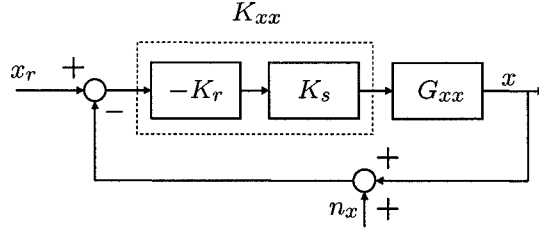


Figure 6.10 The shaping controller is denoted by K_s and the robustifying controller is denoted by K_r .

1. Let $\gamma = 1/\epsilon$. Obtain Z by solving the algebraic Riccati equation (ARE),

$$(A - BS^{-1}D^TC)Z + Z(A - BS^{-1}D^TC)^T - ZC^TR^{-1}CZ + BS^{-1}B^T = 0$$

where $R = I + DD^T$ and $S = I + D^TD$.

2. Obtain X by solving the ARE,

$$(A - BS^{-1}D^TC)^TX + X(A - BS^{-1}D^TC) - XBS^{-1}B^TX + C^TR^{-1}C = 0$$

3. The state space realization of the robustifying controller is given by,

$$K_r = \left[\begin{array}{c|c} A + BF + \gamma^2(L^T)^{-1}ZC^T(C + DF) & \gamma^2(L^T)^{-1}ZC^T \\ \hline B^TX & -D^T \end{array} \right]$$

where $F = -S^{-1}(D^TC + B^TX)$ and $L = (1 - \gamma^2)I + XZ$. The control loop to be implemented is provided in Figure 6.10.

The maximum possible ϵ is given by $\epsilon_{max} = (1 + \rho(XZ))^{-1/2}$ where ρ denotes the spectral radius.

As mentioned earlier an important feature of the Glover McFarlane design is that the loop transfer function before and after robustification is not significantly different. In fact in Ref. [51] it is shown that when $|G_s(j\omega)| > \sqrt{1/\epsilon^2 - 1}$,

$$|K_r(j\omega)| \geq \frac{|G_s(j\omega)| - \sqrt{1/\epsilon^2 - 1}}{\sqrt{1/\epsilon^2 - 1}|G_s(j\omega)| + 1},$$

and when $|G_s(j\omega)| < 1/\sqrt{1/\epsilon^2 - 1}$,

$$|K_r(j\omega)| \leq \frac{|G_s(j\omega)| + \sqrt{1/\epsilon^2 - 1}}{1 - \sqrt{1/\epsilon^2 - 1}|G_s(j\omega)|}.$$

The above inequalities show that in the frequency regions where $|G_s(j\omega)|$ is big and in the frequency regions where $|G_s(j\omega)|$ is small, there is a bound on the extent to which the robustifying controller changes the loop shape.

Robustification of K_{pii}

The design process was applied to G_{xx} with K_s set to K_{pii} from section 6.3.0.1. A 9th order robustifying controller K_r was obtained given by,

$$K_r(s) = \frac{5227.6(s + 5818)(s + 31.45)(s^2 + 160.3s + 5.98 \times 10^6)}{(s + 2797)(s + 5684)(s + 294.8)(s^2 + 386.2s + 6.6 \times 10^6)} \\ \times \frac{(s^2 + 209.6s + 5.6 \times 10^7)}{(s^2 + 397.3s + 1.66 \times 10^7)(s^2 + 203.3s + 5.62 \times 10^7)}$$

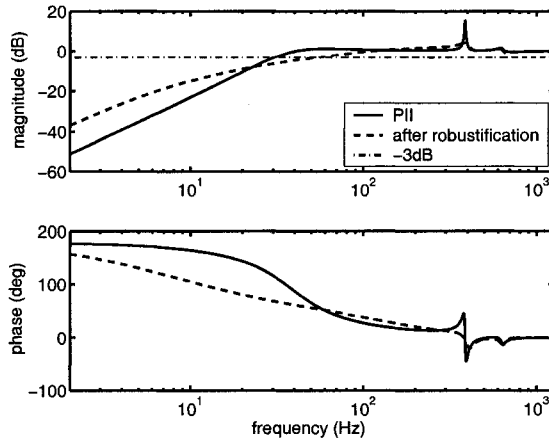


Figure 6.11 This plot illustrates the reduction in $\|S\|_\infty$ value due to Glover McFarlane robustification.

Figure 6.11 compares the simulated sensitivity functions for a design with K_s before and after robustification. The much lower $\|S\|_\infty$ value indicates higher robustness. A careful examination of the sensitivity functions of PII controllers indicate the presence of two distinct peaks. One low frequency peak and one near the resonance of the plant. The low frequency peak arise from the Bode integral formula,

$$\int_0^\infty \ln|S(j\omega)|d\omega = 0$$

to be satisfied by a loop transfer function, L with relative degree two and no poles in the open RHP. Assume that for some $\alpha > 0$, $|S(j\omega)| \leq e^{-\alpha}$ in the frequency region $[0, \omega_1]$. The parameter α is a measure of the tracking performance. From the Bode integral formula the following condition needs to be satisfied,

$$\int_{\omega_1}^{\infty} \ln|S(j\omega)|d\omega \geq \alpha\omega_1$$

Moreover it can be shown that there exists $k > 0$ and ω_2 such that the loop transfer function satisfies, $|L(j\omega)| \leq k/\omega^2$ for all $\omega \in [\omega_2, \infty]$. This added roll off condition which is essential for good resolution, makes the Bode integral effectively a “finite” integral which results in the appearance of the low frequency peak in the S frequency response.

It can be seen that an increase in k_i primarily results in an increase in the magnitude of the high frequency peak where as an increase in k_{ii} results in an increase in the magnitude of the low frequency peak as seen in Figure 6.12(a). Both these peaks are unsuitable for nanopositioning as they introduce low and high frequency oscillations while tracking. As Figure 6.12(a) shows, varying k_i and k_{ii} does not reduce the peaks significantly without substantial compromise on bandwidth. But the robustifying controller with the added model information shapes the sensitivity function in such a way that the low and high frequency peaks are reduced in magnitude simultaneously with marginal compromise on bandwidth.

Figure 6.12(b) compares the experimentally obtained $|S(j\omega)|$ for K_{pii} before and after robustification. There is substantial reduction in the peak of $|S(j\omega)|$ due to the robustifying controller. Note that the bandwidth is comparable for both in spite of the significant difference in robustness.

Designs for higher bandwidth

In step 1 of the proposed two part design, the controller being designed for performance *does not have to result in a stable closed loop map*. Thus for example, considerably more aggressive PII controllers can be implemented with the help of robustification.

Figure 6.13 depicts the experimentally obtained $S(j\omega)$ of a high bandwidth Glover McFarlane design. The design corresponds to a PII controller $\frac{0.001s^2+600s+6 \times 10^5}{s^2}$. The PII controller if used without robustification results in instability of the closed loop. However with robustification, the design is stable and it guarantees good robustness margins with the added benefit of increased performance.

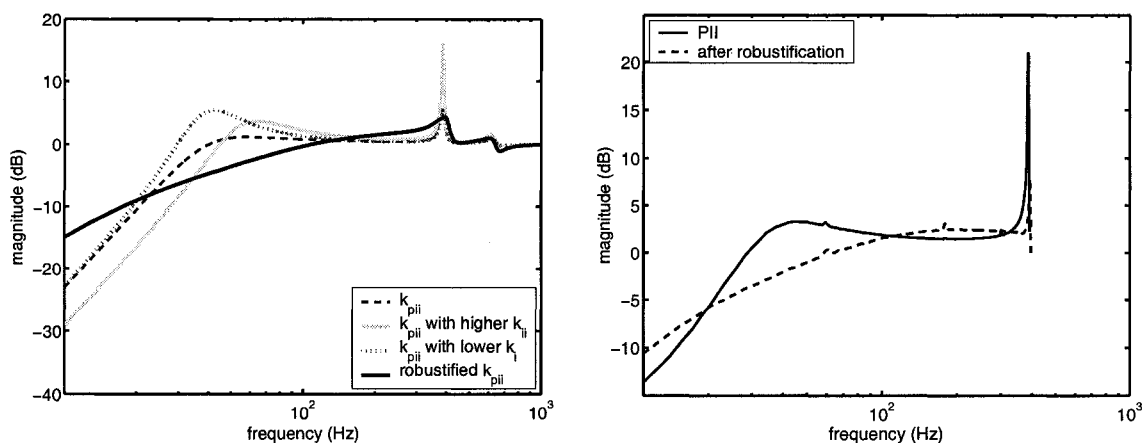


Figure 6.12 (a) The control design can be viewed as shaping of the sensitivity function while satisfying the Bode integral formula. An increase in the gains of the PII controller results in two significant peaks appearing in the plot of $|S(j\omega)|$. Without any model information, it is not possible to reduce the two peaks by varying the PII coefficients without compromising on the bandwidth significantly. The robustifying controller with its model information shapes S in such a way that both the peaks are reduced in magnitude at the expense of marginal performance (b) Experimentally obtained $S(j\omega)$ of K_{pii} before and after robustification.

This plot shows significant increase in bandwidth ($> 55 \text{ Hz}$) without much loss in robustness ($\|S\|_{\infty} = 1.7$).

Triangular signals are tracked using the implemented Glover McFarlane designs. Figure 6.14 illustrates the tracking of 5 Hz and 10 Hz signals using the aggressive Glover McFarlane design. Except for the turn around points the tracking error is small. For the 5 Hz triangular signals, approximately 70% of the period is usable in this case compared to 30% for K_{pii} in spite of the larger amplitude of the reference waveform. Moreover these controllers are remarkably robust allowing the use of filters inside the loop to improve resolution.

Since the performance and robustness requirements are decoupled, Glover McFarlane controllers can be used to robustify commonly used controllers like PII which have features like zero steady state error for ramp tracking. This is a significant advantage particularly when the nano-positioner is used for scanning applications. But in applications where robustification of existing controllers is not required,

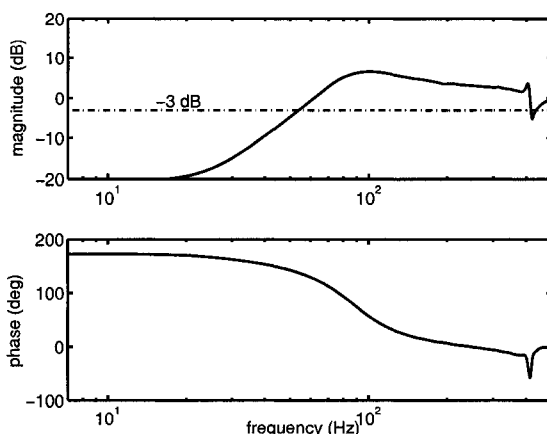


Figure 6.13 Experimentally obtained sensitivity function of an aggressive (high bandwidth) Glover McFarlane design

particularly in applications like nanolithography where zero steady state error ramp tracking is not essential single step designs like \mathcal{H}_∞ can be employed which is addressed next.

6.3.0.2 Robust \mathcal{H}_∞ control design

Nominal \mathcal{H}_∞ control design

One of the disadvantages of classical control design processes is that exhaustive search over the space of controller parameters is needed to meet bandwidth and resolution requirements. Also, in these designs, the open-loop transfer function is shaped even when these requirements are made on the closed loop transfer function. In the nominal \mathcal{H}_∞ design, the control law is obtained as a solution to an optimization problem which incorporates the performance objectives in its cost function. In this design the performance requirements are imposed directly on the closed loop transfer functions S , T and KS using appropriate weighting functions. Since the error $e_x = Sx_r - Tn_x$, the bandwidth requirement is imposed on S . The requirement of high resolution is translated to rolling off of T at high frequencies. A bound on KS can be used to limit the control effort, u_x since $u_x = KSx_r$. In this design, a controller

transfer function is obtained through an iterative process (see [48]) such that

$$\left\| \begin{array}{c} w_p S \\ w_T T \\ w_u KS \end{array} \right\|_\infty \leq 1, \text{ where}$$

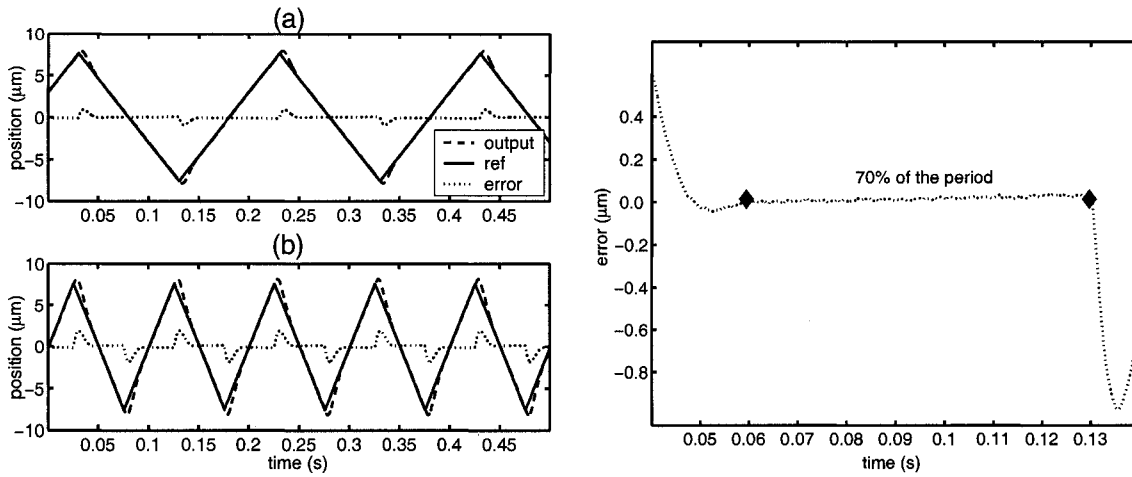


Figure 6.14 (a) Tracking of 5 Hz triangular signals using a Glover McFarlane controller. (b) Tracking of a 10 Hz signal using the Glover McFarlane controller. Except for the turn around regions, the tracking is very good. (c) For the 5 Hz triangular signals, almost 70% of the period is usable in this case.

w_p , w_T and w_u are the weighting functions that we design. Such a controller guarantees $\|w_p S\|_\infty \leq 1$, $\|w_T T\|_\infty \leq 1$ and $\|w_u K S\|_\infty \leq 1$. These weighting functions are designed to specify the frequency information of the performance objectives and system limitations. The transfer function, w_p , was chosen such that it has high gains at low frequencies and low gains at high frequencies. This scaling ensures that the optimal feedback law is such that the sensitivity function is small at low frequencies, thus guaranteeing good tracking at the concerned frequencies. More precisely, w_p was chosen to be $\frac{0.67s^2+769.5s+2.2 \times 10^5}{s^2+9.425s+22.1}$. This was done to achieve a closed loop bandwidth of 75 Hz and to induce a 40 dB slope for S which approximates a double integrator (to have better ramp tracking). The weighting function, $w_T = \frac{s+571.2}{0.01s+628.3}$ was chosen so that it has low gains at high frequencies and high gains at low frequencies. This was done to ensure rolling off of the complementary sensitivity function at high frequencies to have noise attenuation and thereby have better resolution. Figure 6.15 depicts $|w_p(j\omega)|$ and $|w_T(j\omega)|$.

The weighting function for the control, w_u was chosen to be a constant given by $w_u = 1/10$. This ensured that the piezo signals were within saturation limits. A 10th order controller was obtained from

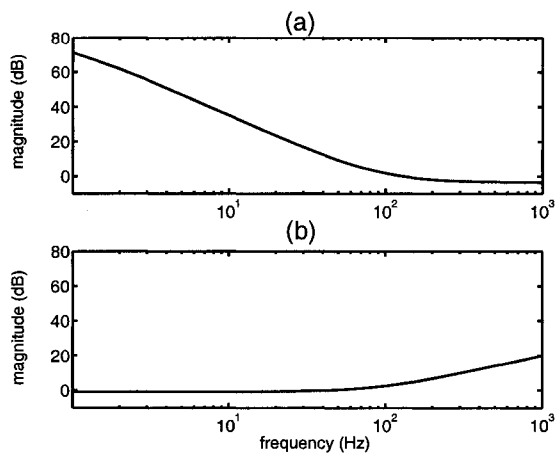


Figure 6.15 a) The weighting function for the sensitivity function. The 40 dB roll off is to approximate a double integral action which enables steady state ramp tracking. b) The weighting function for the complimentary sensitivity function.

this design which has a bandwidth of 104 Hz .

The controller was found to be non-robust and was found to have poor noise characteristics after implementation. The reason for this behavior is that the nominal \mathcal{H}_∞ design does not account for pole uncertainties which are crucial for G_{xx} which has lightly damped poles. The nominal \mathcal{H}_∞ controller has zeros at 389 Hz which is a dominant pole of G_{xx} which is also lightly damped. See Ref. [52] for a detailed description of these pole-zero cancellations in nominal \mathcal{H}_∞ designs. Nominal \mathcal{H}_∞ design without consideration for robustness is found to be inappropriate for the nano-positioner. Robust \mathcal{H}_∞ designs which account for pole uncertainties is one way of tackling this problem at the expense of bandwidth.

Robust \mathcal{H}_∞ design

In this design, The pole uncertainty in G_{xx} is characterized using multiplicative uncertainty. The poles (those corresponding to the primary resonances) are varied over a certain regime and their corresponding frequency responses are plotted. $w_i(s)$ is obtained such that these responses are captured by the perturbed plants $G_{xx}(s)(1 + w_i(s)\Delta)$ where |

$\Delta\|_{\infty} < 1$. It can be shown that if a controller has to satisfy $\|w_p S\|_{\infty} \leq 1$ for plants belonging to a class $\mathcal{G}_{xx} = \{G_{xx}(1 + w_i \Delta) : \|\Delta\|_{\infty} \leq 1\}$, then it is sufficient that, $\left\| \begin{array}{c} w_p S \\ w_i T \end{array} \right\|_{\infty} \leq 1/\sqrt{2}$ is satisfied (see Ref. [48]). So in the original nominal \mathcal{H}_{∞} problem, the selection of $w_T = w_i$ fetches robust performance instead of just nominal performance. For G_{xx} , w_i was selected to be,

$$w_i(s) = \frac{0.84s^2 + 2214s + 5.3 \times 10^6}{s^2 + 575.5s + 6.12 \times 10^6}.$$

In the original \mathcal{H}_{∞} problem, w_T was chosen to be w_i to incorporate the added robust performance requirement. The resulting controller was 11th order.

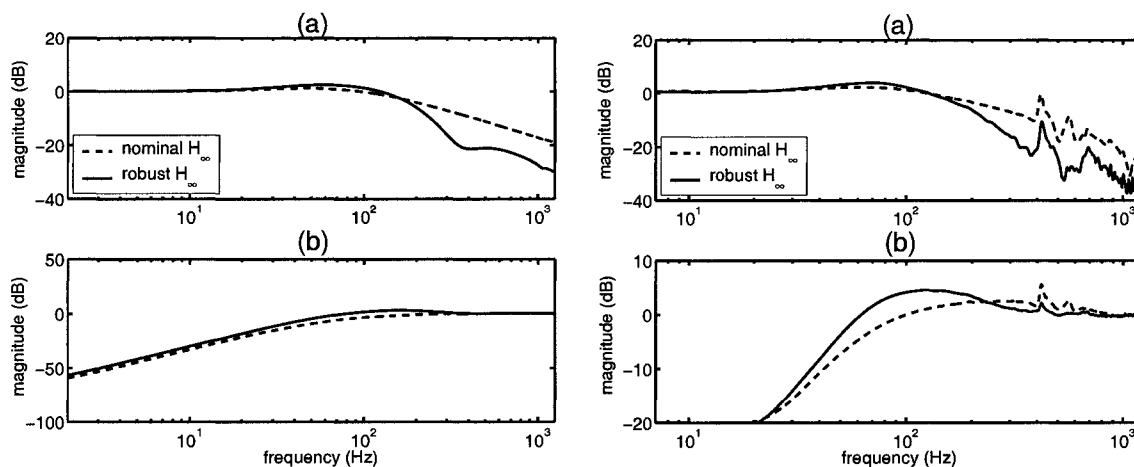


Figure 6.16 (a) Analytical S and T frequency responses for nominal and robust \mathcal{H}_{∞} designs. (b) The experimentally obtained sensitivity and complementary sensitivity functions are compared for nominal and robust \mathcal{H}_{∞} designs.

A comparison of the analytical closed loop transfer functions of the two designs are shown in Figure 6.16(a). The experimental plots are compared in Figure 6.16(b). It can be seen that the experimental closed loop transfer function plots have some features absent in the analytical plots. This is due to uncertainty in the plant model, particularly pole uncertainty. Figure 6.16(b) shows the experimental result of how the robust design introduces a dip in this frequency region thus reducing the magnitude of these unwanted peaks (Figure 6.16(b) shows a 5 times reduction in the unwanted peak at near the

dominant pole location due to the robust design).

Implementation of the controllers

The controllers designed in section 6.3 were discretized and implemented on an *Analog Devices* ADSP-21160 Digital Signal Processor. A schematic of the control system is shown in Figure 6.17. The analog signals were sampled at 100 kHz .

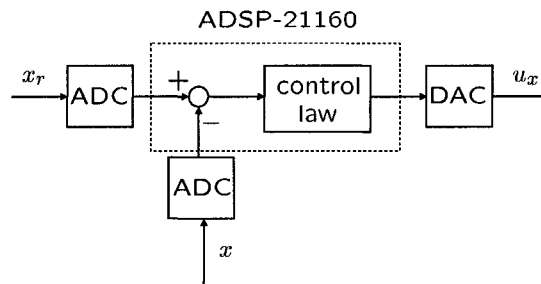


Figure 6.17 A schematic of the controller hardware.

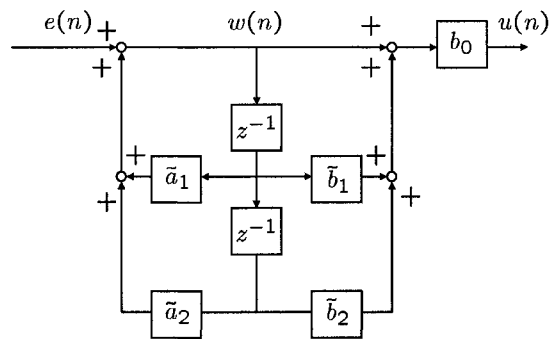


Figure 6.18 The controllers were split into second order sections (biquads) and each of them was implemented in a direct form II IIR structure depicted above. The computational time for one biquad is $24ns$. $\tilde{b}_1 = b_1/b_0$, $\tilde{b}_2 = b_2/b_0$, $\tilde{a}_1 = -a_1$ and $\tilde{a}_2 = -a_2$.

The discretized controllers were split into biquad sections (second order sections) and each biquad was implemented in a Direct Form II IIR structure. This cascade implementation allows optimum

pole-zero pairing and ordering which can be used to counter finite word length effects (see Ref. [53]).

Figure 6.18 shows the direct form II realization of a single biquad given by, $\frac{b_0+b_1z^{-1}+b_2z^{-2}}{1+a_1z^{-1}+a_2z^{-2}}$.

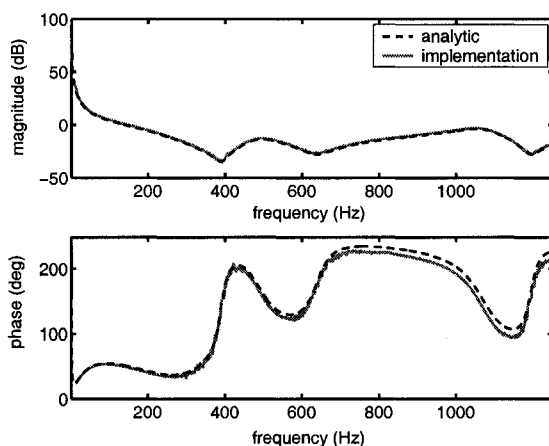


Figure 6.19 The experimentally obtained frequency response of an implemented robust \mathcal{H}_∞ controller is compared with the analytical response. The minor difference in phase is attributed to delay in the circuitry.

The frequency response of an implemented controller (robust \mathcal{H}_∞) is compared with the analytical response in Figure 6.19. The slight difference in phase is due to delay in the loop.

6.4 Characterization of the device

The range of the X stage was obtained to be $110 \mu\text{m}$ and the sensitivity of X LVDT was found to be $6.76 \mu\text{m}/\text{V}$.

Since this device has no backlash (as there are no sliding parts) or any other such design restrictions, the resolution of the device is primarily determined by noise. However, this makes the comparison of resolution between the open and the closed loop configurations difficult. Theoretically, since in the closed loop designs, the noise is fed back to the actuator, they cannot achieve better resolutions than the open loop configurations. However, the open loop devices are plagued by nonlinear effects such as drift and creep which make it very difficult to attain these theoretical values in a repeatable and predictable manner. On the other hand with these nonlinear effects being practically absent, the closed loop designs give much better access to accurate positioning. We emphasize here that though theoretically the open-

loop resolutions are better (which may possibly be realized with very rigorous experiments and post data processing), it is much easier to predict and *realize* accurate positioning in the closed loop designs.

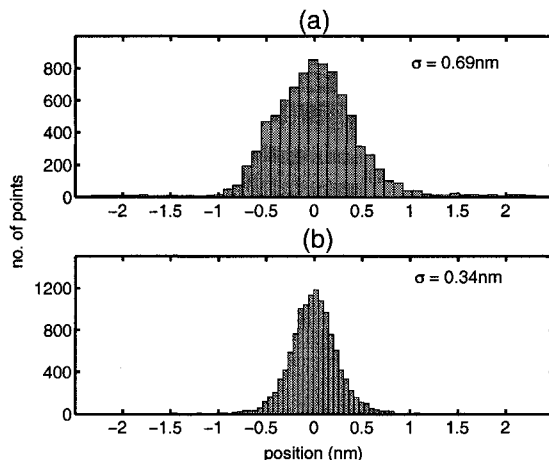


Figure 6.20 a) LVDT measurement without the controller. b) LVDT measurement while a controller is stabilizing at 0V.

Since the transfer function between x and the noise, n is T , ($x = Tx_r - Tn$) this transfer function forms a good basis to characterize resolution and compare different designs. This transfer function brings forth the trade off that exists between the resolution and the bandwidth. This is seen from the fact that higher bandwidth implies bigger error signals and therefore worse resolutions. The resolutions can be characterized by associating appropriate metrics to the error signals $e_x = Tn$ if enough statistics describing n is available. This presents us the other problem we have with the characterization of the resolution. It is the fact that our measurements are limited by the resolution of the LVDT sensors, i.e., the device is capable of motions that are smaller than which LVDT can detect. However, to get a quantitative feel of how small these error signals can be, the following experiment was done. The LVDT signals for both the open-loop and the closed-loop (Glover McFarlane) designs were measured when the system is at the nominal operating point. The measurement is taken over a small time window since in open loop the mean varies with drift, creep etc. Figure 6.20 shows that the variance of the sensor output while in open loop is higher than that in closed loop. This illustrates the improvement in 'resolution' due to feedback. It should be remembered that the closed loop resolution depends on the bandwidth and the shape of the corresponding complementary sensitivity functions. Better resolutions

can be achieved by reducing the bandwidths.

As mentioned earlier, the application of the piezoactuated devices are greatly limited by nonlinear effects such as hysteresis and creep. However these effects are nearly eliminated by the feedback designs described earlier.

6.5 Conclusions

In large range nanopositioners along with bandwidth and resolution, robustness assumes great significance. A highly robust linear controller is needed to tackle the nonlinearities associated with piezoactuation and the changing flexure dynamics without having to design specific nonlinear controllers. The design goals of robustness, bandwidth and resolution can be quantified in a straight forward manner in the framework of modern robust control. Two approaches are employed to build controllers which provide high robustness while maintaining or bettering the stringent bandwidth and resolution requirements. The Glover McFarlane design is particularly attractive when the need is to robustify an existing controller with specific tracking requirements like having to track ramp signals with zero steady state error. It also has the advantage of not having to characterize the uncertainty explicitly. If there is no specific tracking requirement and if an a priori characterization of uncertainty is available, then a robust \mathcal{H}_∞ design is found to be attractive for robust nanopositioning. These design methodologies are experimentally demonstrated on a two dimensional large range nanopositioner. The analytic and experimental sensitivity and complementary sensitivity functions along with some tracking results are shown to demonstrate the merits of the design. The infinity norm of S is chosen to be the measure of robustness while comparing the various design schemes.

CHAPTER 7 Nanopositioning approach to contact mode AFM imaging

The design schemes developed for robust broadband nanopositioning described in Chapters 5 and 6 were applied to the imaging problem in an Atomic Force Microscope. The problem of imaging is viewed from a modern control perspective. A similar approach has been pursued in Ref. [43]. In this chapter, I present some new insights and a few preliminary ideas and results on improving the quality of imaging. In section 7.1, a brief description of the device is presented. The modern control framework for imaging is developed in section 7.2. Section 7.3 describes the new control strategies employed and the experimental results.

7.1 Device description

The schematic of the AFM (*Asylum Research, Santa Barbara, California*) used in the research is shown in Figure 7.1. The cantilever deflection is measured using an optical detection system. The sample to be imaged is placed on an X-Y nano-positioning stage. In a typical imaging operation, the cantilever deflection is maintained at a set point while scanning the sample surface using the nano-positioner. This is achieved using a feedback controller which moves a Z positioner to which the cantilever is attached. The control effort is typically considered to be a good measure of the sample profile.

7.2 Formulation of the imaging problem

Figure 7.2 describes the resulting feedback loop when the AFM imaging is viewed from a systems perspective. Let G_z denote the transfer function between the control effort and the Z positioner's movement (in nanometers) and let G_c be the map between the Z movement and the cantilever deflection. The sample profile is filtered by a system G_d and enters the loop as a disturbance. The output is the

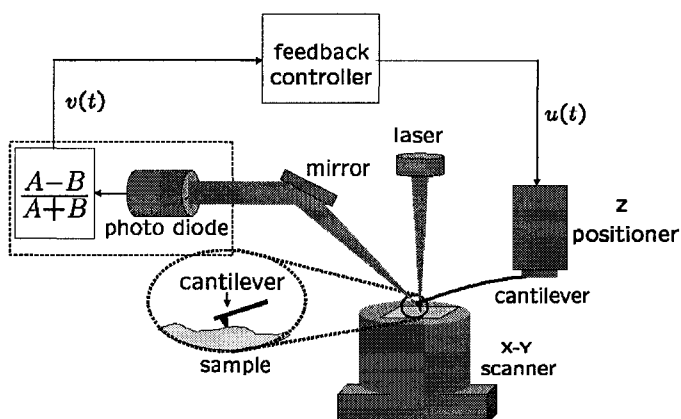


Figure 7.1 The principal components of the AFM are a micro-cantilever, an optical detection system, an X-Y sample positioner, a Z positioner and a feedback controller. The Z positioner is moved up and down to maintain a constant cantilever deflection while the sample is being scanned.

signal from the optical detector. Assuming the photodiode has no dynamics and is linear, S_D is a constant which is the sensitivity of the optical detector. It can be easily seen that G_c and G_d are the

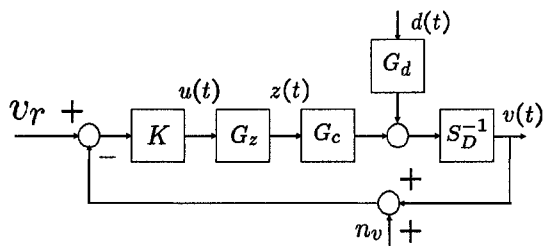


Figure 7.2 Systems perspective to AFM imaging. $v(t)$ is the output of the optical detector and the disturbance $d(t)$ is the sample profile. The control effort is $u(t)$ and the resulting motion of Z positioner is $z(t)$. The controller is trying to maintain a constant deflection in the presence of the disturbance entering the loop.

same. Assuming linearity about an operating point Figure 7.2 can be reduced to Figure 7.3. Here \bar{d} is assumed to be a scaled version of d if G_c is assumed to be a constant S_c . $G_{zv} = G_z S_c S_D^{-1}$ is the map between the input to the Z positioner and the optical detector's output.

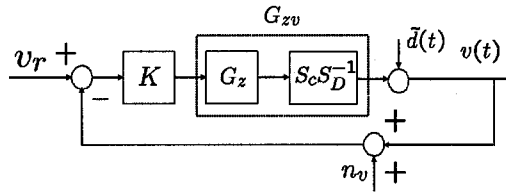


Figure 7.3 G_{zv} is the transfer function between the input to the Z positioner and the output of the optical detector. \tilde{d} is a scaled version of the sample profile.

The imaging problem can be stated as the problem of measuring $\tilde{d}(t)$ while maintaining $v(t)$ near v_r and in the presence of the detector noise n_v .

G_{zv} was identified using frequency domain identification techniques. Figure 7.4 depicts the experimental frequency response and the response of a model used to fit the experimental response. The identified $G_{zv}(s)$ is fourth order and is given by,

$$G_{zv}(s) = 9.5 \times 10^8 \frac{s^2 + 4.76s + 8.67 \times 10^6}{(s^2 + 58.68s + 8.53 \times 10^6)(s^2 + 1467s + 1.2 \times 10^8)}$$

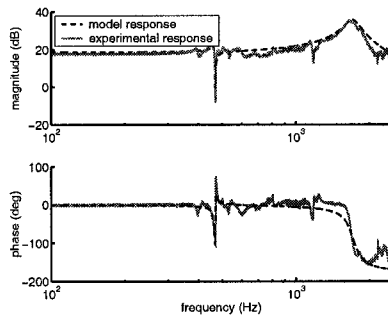


Figure 7.4 Experimental frequency response of G_{zv} versus that of its model. This figure shows that the fourth order model captures the response accurately

7.3 Control design

As stated in section 7.2, the imaging problem is observing $\tilde{d}(t)$ while maintaining a set point deflection. It is important not to have substantial error while maintaining this deflection value. A big error could result in tip and sample damage. It is also important to maintain the cantilever tip in a linear regime of operation. This translates to a requirement on the bandwidth. High bandwidth enables the measurement of \tilde{d} with higher frequency content which leads to faster imaging speeds. There are stringent requirements on the resolution in Atomic Force Microscopy. The cantilever sensor has sub-nanometer resolution over a kilo Hertz bandwidth in open loop. There is a bandwidth versus resolution tradeoff which needs to be addressed. Robustness is another important requirement. The Z positioner is piezo driven and hence is highly nonlinear. Since G_{zv} is modelled as a linear system, it is imperative that the controller designed should be robust to model uncertainties. Diverse operating conditions and the fact that the end users of the AFM are people with limited knowledge in control theory further necessitates high robustness.

Currently only proportional-integral controllers are used in commercial Atomic Force Microscopes. These non-model based controllers have severe bandwidth limitations. The robustness of these controllers are very poor. Moreover the control effort is used as a measure of the sample profile. From Figure 7.3, it is seen that when G_{zv} is a constant with no dynamics, the control effort can be used as a measure of the sample profile. This approximation fails especially at high frequencies when the dynamics of the Z positioner become prominent.

Two approaches are taken for the control design problem. The first one involves the design of Glover McFarlane \mathcal{H}_∞ loop shaping controllers. This design is particularly attractive since the design can be done on existing PI controllers as depicted in the next section. In the second approach, requirements on bandwidth, resolution and robustness are translated to constraints on the loop shapes of the appropriate closed loop transfer functions. Mixed sensitivity \mathcal{H}_∞ controllers are designed to obtain the required loop shapes. Moreover properties of these controllers allow the use of a better signal as a measure of the sample profile.

7.3.1 \mathcal{H}_∞ loop shaping design for robust imaging

Integral controllers are widely used in industry since they can track step signals with zero steady state error. But there are severe bandwidth limitations as well as poor robustness. Glover McFarlane loop shaping design (see Ref. [50] and Ref. [51]) robustifies the system while maintaining the integral structure of the controller. The design involves two steps:

1. The selection of an integral controller as the shaping controller K_s
2. Obtain a robustifying controller K_r to robustify the shaped plant $G_{zv}K_s$

Figure 7.5 depicts the resulting closed loop. Another significant advantage of the Glover McFarlane design is that instead of using $u(t)$ as a measure of the sample profile, $\tilde{u}(t)$ could be used as a measure of the sample profile. $\tilde{u}(t)$ is found to be a better measure of the sample profile. As a result of extensive

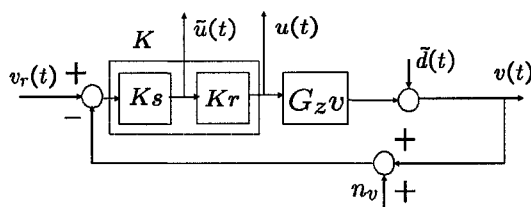


Figure 7.5 This figure depicts the design of a Glover McFarlane \mathcal{H}_∞ loop shaping controller for imaging. K_s is an integral controller. A robustifying controller K_r is designed based on the model information. $\tilde{u}(t)$ is found to be a better measure of the sample profile $\tilde{d}(t)$.

tuning of the system, an integral controller of $K_i(s) = 136/s$ was obtained. Any further increase in the gain of the integral controller results in severe lack of robustness and sustained oscillations. In the design of Glover McFarlane robustifying controllers the shaping controller, K_s could be chosen such that it makes the closed loop unstable if used without robustification. Hence an aggressive integral controller $K_s(s) = 500/s$ could be chosen as the shaping controller. A robustifying controller for the shaped plant was obtained given by,

$$K_r(s) = \frac{2.9 \times 10^4 (s^2 + 98.03s + 8.55 \times 10^6)}{(s + 1.9 \times 10^4)(s^2 + 10.58s + 8.74 \times 10^6)} \\ \times \frac{s^2 - 1562s + 9.25 \times 10^7}{s^2 + 1.2 \times 10^4 + 2.473 \times 10^8}$$

Figure 7.6 shows the sensitivity plots for K_i and $K_s K_r$. The integral controller provides a bandwidth of 181 Hz while the Glover McFarlane controller gives a bandwidth of 301 Hz. The improvement in robustness is evident from the values of $\|S\|_\infty$. For the integral controller, $\|S\|_\infty$ is 4.46 while that for the robustified controller is 1.4. Note that $\|S\|_\infty$ is a direct measure of robustness. Lower bounds on the gain and phase margins can be derived from $\|S\|_\infty$ (see Ref. [48]). While imaging, S is a measure of

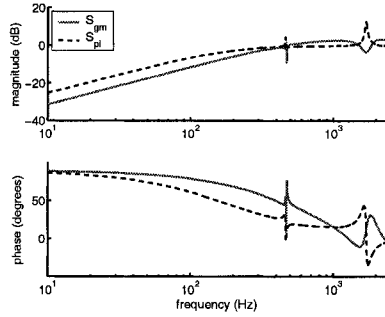


Figure 7.6 The sensitivity function obtained using the integral controller is compared with that obtained using the Glover McFarlane design. There is remarkable improvement in the bandwidth and robustness.

the effectiveness of maintaining the set point deflection. So S should be small in the frequency region of the disturbance signal which is the sample profile. Besides rejecting the disturbance signal it is also necessary to observe the signal. Currently in commercial AFMs $u(t)$ is used to observe $d(t)$. With the model information it is possible to design an observer to obtain $\tilde{d}(t)$ from $u(t)$. In the case of Glover McFarlane controller and also in the subsequent stacked \mathcal{H}_∞ controller, it is seen that by looking at a new intermediate signal $\tilde{u}(t)$, a good estimate of $\tilde{d}(t)$ can be obtained without having to build an extra observer. Thus with the design of a single robustifying controller over an existing integral controller, the twin objectives of robustness and a better observation of the disturbance signal (sample profile) could be achieved. Figure 7.7 compares the normalized KS (transfer function between $u(t)$ and $\tilde{d}(t)$) of the K_i controller with the normalized $K_s S$ (transfer function between $\tilde{u}(t)$ and $\tilde{d}(t)$) and normalized $K_s K_r S$ (transfer function between $u(t)$ and $\tilde{d}(t)$) of the Glover McFarlane design. Experiments were performed using these controllers. A 2 μm calibration grating with 250 nm depth was imaged using the controllers. Since there is no independent measure of the sample profile, an experiment was done where the sample is imaged across a length of $\approx 80 \mu\text{m}$ and then it is imaged in the other direction.

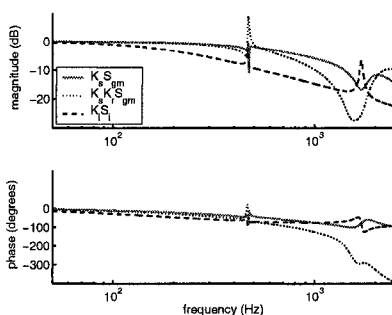


Figure 7.7 This figure compares the transfer functions from the sample profile $\tilde{d}(t)$ to $u(t)$ of the integral controller, $u(t)$ of the Glover McFarlane controller and $\tilde{u}(t)$ of the Glover McFarlane controller. It is evident that the normalized transfer function between $\tilde{d}(t)$ and $\tilde{u}(t)$ is closer to unity which is needed for a faithful observation of $\tilde{d}(t)$.

Let these be the trace and retrace signals. If the tracking is good, the trace and retrace signals should coincide. Figure 7.8 shows the tracking using K_i while Figure 7.10 depicts the tracking using the Glover McFarlane controller. There is a significant improvement in tracking.

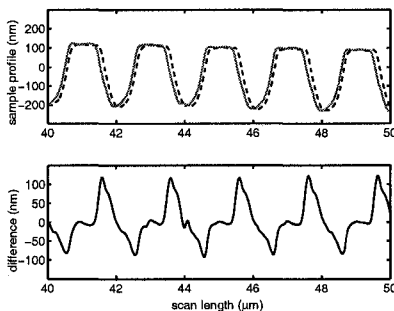


Figure 7.8 A calibration sample with triangular grooves of depth 250 nm and width 2 μm is imaged using the integral controller, K_i . There is significant error between the trace and retrace signals.

7.3.2 Robust imaging as a stacked sensitivity problem

In the second method employed the requirements of imaging are translated into requirements on the loop shapes of the closed loop transfer functions of the interconnection given in Figure 7.3. The

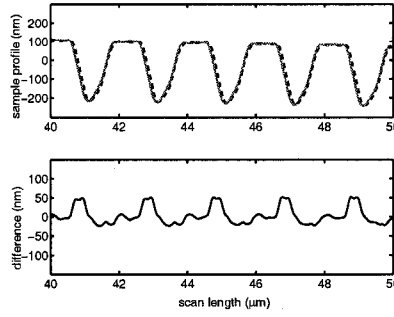


Figure 7.9 Imaging is done using the Glover McFarlane controller using $u(t)$ to observe the profile. There is an improvement in the quality of imaging compared to the integral controller.

bandwidth requirement can be posed a loop shaping problem for the sensitivity function S since S is the transfer function between the error signal $v_r - v(t)$ and the sample profile $\tilde{d}(t)$. In order to minimize the effect of noise, the transfer function between noise and $v(t)$, T has to roll off at high frequencies. There should also be a bound on the control effort since the amplifiers have limits on the voltage input range. Robustness requirements are captured by upper bounds on the infinity norms of the close loop transfer functions. These requirements on robustness and performance can be translated into weighting functions W_S , W_T and W_u as shown in Figure 7.11. The control design problem reduces to finding a stabilizing controller such that,

$$\left\| \begin{bmatrix} W_S S \\ W_T T \\ W_u K S \end{bmatrix} \right\|_{\infty} < 1 \quad (7.1)$$

This is the \mathcal{H}_{∞} stacked sensitivity problem (see Ref. [48]).

Here again it is important to have a new signal to “observe” $\tilde{d}(t)$ instead of using $u(t)$ as a measure of the sample profile. To simulate an integral action the weighting function for S is chosen such that it has a 20 dB slope in low frequency region. This forces the weighting function W_S to have a pole near zero. From Ref. [52] and Ref. [54] the controller obtained by solving 7.1 has the poles of W_S as its own poles and the poles of G_{zv} as its own zeros. This allows one to split the controller into two $K_{1\infty}$ and $K_{2\infty}$ with $K_{1\infty}$ containing the pole of W_S and $K_{2\infty}$ containing those zeros of the controller which are the poles of G_{zv} . The $\tilde{u}(t)$ as seen in Figure 7.12 is a better measure of $\tilde{d}(t)$, the sample profile.

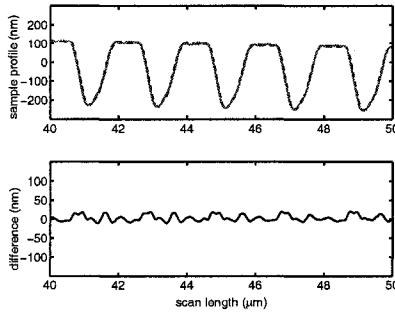


Figure 7.10 Imaging is done using the Glover McFarlane controller using $\tilde{u}(t)$ to observe the profile. There is a significant improvement in the quality of imaging over both the integral controller and the case where $u(t)$ is used to observe the profile.

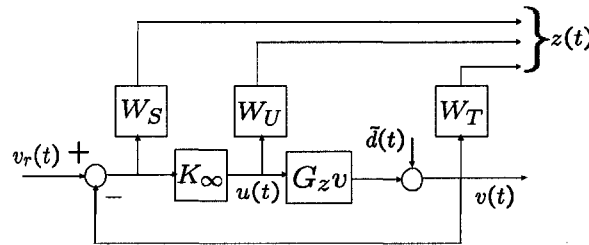


Figure 7.11 Weighting functions W_S , W_U and W_T are used to specify the requirements of imaging. This is followed by designing a stabilizing controller such that the \mathcal{H}_∞ norm of the operator between $v_r(t)$ and $z(t)$ is less than one.

This is because the transfer function between $\tilde{u}(t)$ and $\tilde{d}(t)$ is $K_{1\infty}/(1 + K_{1\infty}K_{2\infty}G_{zv})$ and $K_{2\infty}$ cancels off the poles of G_{zv} . Here is an instance of taking advantage of the pole zero cancellations in stacked \mathcal{H}_∞ problems. Since the G_{zv} poles are not lightly damped, minor shifts in the pole positions shouldn't cause significant errors. The resulting $K_{1\infty}$ is given by,

$$K_{1\infty}(s) = 0.0011 \frac{s + 9.43 \times 10^5}{s + 0.6283}$$

and $K_{2\infty}$ is given by,

$$\begin{aligned} K_{2\infty}(s) &= 7.28 \times 10^{10} \frac{s^2 + 58.68s + 8.53 \times 10^6}{s^2 + 4.682s + 8.674 \times 10^6} \\ &= \frac{s^2 + 1467s + 1.155 \times 10^8}{(s^2 + 1.69 \times 10^6s + 9.7 \times 10^{11})(s + 9 \times 10^6)} \end{aligned}$$

$K_{1\infty}$ and $K_{2\infty}$ were implemented and the $2 \mu m$ grating was imaged. The resulting trace and

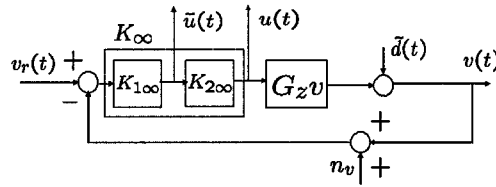


Figure 7.12 The stacked \mathcal{H}_∞ controller K_∞ is split into two, $K_{1\infty}$ and $K_{2\infty}$ such that $K_{1\infty}$ resembles an integrator and $K_{2\infty}$ resembles an inverse of the plant G_{zv} .

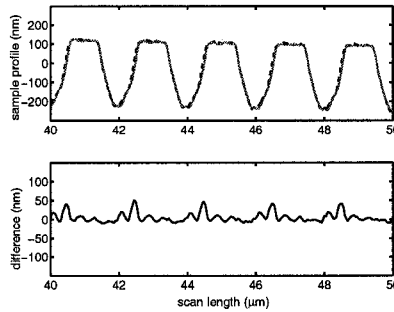


Figure 7.13 Imaging of the $2 \mu m$ grating is done using the \mathcal{H}_∞ controller K_∞ . The sample profile is estimated using $\tilde{u}(t)$.

retrace signals are shown in Figure 7.13. There is a significant improvement in imaging compared to the integral controller. Figure 7.14 compares the deflection signals, $S_D v(t)$ for the integral, Glover McFarlane and the stacked \mathcal{H}_∞ controllers. The root mean square error in the deflection signal for the integral controller is 29.1 nm compared to 21 nm for the Glover McFarlane design and 10.24 nm for the stacked \mathcal{H}_∞ controller.

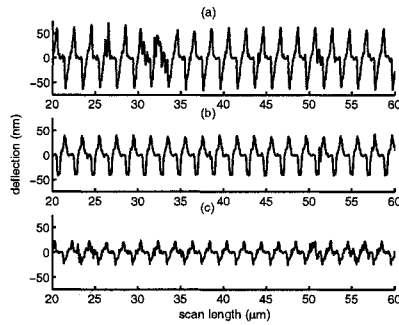


Figure 7.14 This figure compares the deflection signals for K_i , $K_s K_r$ and K_∞ while imaging. The error is significantly lower than that of K_i for both the Glover McFarlane and \mathcal{H}_∞ controllers.

7.4 Conclusions

The contact mode imaging problem using an Atomic Force Microscope is formulated in the framework of modern control. The requirements of imaging namely bandwidth, resolution and robustness are addressed using two design approaches. The Glover McFarlane \mathcal{H}_∞ loop shaping design is particularly attractive when the existing integral control structure of the commercial AFM controllers is to be maintained. In the second approach, the requirements of imaging are imposed as constraints on the loop shapes of appropriate closed loop transfer functions. Stacked \mathcal{H}_∞ controllers are designed. In both designs, it is possible to extract a signal which is a good “observer” of the sample profile which is modelled as a disturbance. The designed controllers were implemented and imaging was performed on a $2 \mu m$ calibration grating to compare the performance of the controllers. The ideas presented in this chapter has led to the development of a few novel results reported in Ref. [55].

CHAPTER 8 Conclusion

Systems concepts and control theory have a significant role to play in the rapidly emerging field of nanoscience and nanotechnology. This thesis demonstrates this by addressing two of the primary enabling tools of nanotechnology: interrogation of matter at the nanoscale and nanoscale positioning of materials at high bandwidth and high precision.

In Part I of the thesis, the dynamics of the Atomic Force Microscope (the foremost tool in the manipulation and interrogation of matter at the atomic scale) is investigated. The systems approach presented in Chapter 2 significantly complements the physical studies performed and gives valuable insights into the salient features and limitations of the tapping-mode operation of the AFM. Conditions for the existence and stability of periodic solution are obtained for the tapping-mode operation. The commonly observed near sinusoidal nature of the periodic solution is explained by obtaining a priori bounds on the higher harmonics. In Chapter 3, the systems perspective is further exploited to identify the tip sample interaction forces. A simple parametric model is developed for this and experimental results show remarkable agreement with the model. The asymptotic approach developed by Bogoliubov and Mitropolski for weakly nonlinear oscillators can explain some of the distinctly nonlinear features observed in tapping-mode operation. This is presented in Chapter 4.

The second part of the thesis addresses robust broadband nanopositioning. High bandwidth, high resolution and good robustness are identified to be the primary needs of nanopositioning. The commonly employed open loop schemes and non model based controllers do not meet the current requirements for bandwidth and resolution. They also lack in robustness resulting in instability and sustained oscillations. In this thesis a new paradigm is presented for the systematic design and implementation of controllers for nanopositioners. It consists of two methodologies, a design for bandwidth and resolution and a design for robustness. In Chapter 5, through the design and implementation of a one dimensional nanopositioner, the design for bandwidth and resolution is demonstrated. Unlike traditional design

schemes, the bandwidth and resolution requirements could be specified in a straight forward fashion. The experimental results on the one dimensional nanopositioner show remarkable improvement over traditional designs. Robustness is a significant requirement for nanopositioners since they are operated over a wide range of operating conditions and the piezo-electric actuators which drive them are highly nonlinear. The robustness aspect of nanopositioning is explicitly addressed in Chapter 6, through the design and implementation of a two dimensional nanopositioner. In Chapter 7, the contact mode AFM imaging problem is formulated in the framework of nanopositioning and some novel ideas and results on improving the quality of imaging is presented.

These results clearly show the efficacy of systems tools and ideas in addressing the challenges posed by nanotechnology. Future and ongoing work include a transient signal based scheme for the fast detection of changes in tip-sample interaction in the tapping mode operation of the AFM (see [13] and [11]). Efforts are on to apply this scheme to the problem of detecting biological interactions. A novel static non-contact mode of operation for the AFM is also being developed (see [12]).

BIBLIOGRAPHY

- [1] J. Fritz, M. K. Baller, H. P. Lang, H. Rothuizen, P. Vettiger, E. Meyer, H. J. Gntherodt, Ch. Gerber, and J. K. Gimzewski, "Translating biomolecular recognition into nanomechanics," *Science*, vol. 288, pp. pp. 316–318, 2001.
- [2] M. Benoit, D. Gabriel, G. Gerisch, and H. E. Gaub, "Discrete interactions in cell adhesion measured by single-molecule force spectroscopy," *Nature Cell Biology*, vol. 2(6), pp. pp. 313–317, 2000.
- [3] O. H. Willemsen, M. Snel, A. Cambi, J. Greve, B. G. De Grooth, and C. G. Figdor, "Biomolecular interactions measured by atomic force microscopy," *Biophysical Journal*, vol. 79, pp. pp. 3267–3281, 2000.
- [4] D. Rugar, C. S. Yannoni, and J. A. Sidles, "Mechanical detection of magnetic resonance," *Nature*, vol. 360, pp. 563–566, 1992.
- [5] J. A. Sidles, "Folded stern-gerlach experiment as a means for detecting nuclear magnetic resonance of individual nuclei.," *Physical Review Letters*, vol. 68, pp. 1124–1127, 1992.
- [6] J. A. Sidles, J. L. Garbini, and G. P. Drobny, "The theory of oscillator-coupled magnetic resonance with potential applications to molecular imaging," *Review of Scientific Instruments*, vol. 63, pp. 3881–3899, 1992.
- [7] E. Eleftheriou, T. Antonakopoulos, G. K. Binnig, G. Cherubini, M. Despont, A. Dholakia, U. Durig, M. A. Lantz, H. Pozidis, H. E. Rothuizen, and P. Vettiger, "Millipede-a mems based scanning-probe data storage system," *IEEE Transactions on Magnetics*, vol. 39(2), pp. pp. 938–945, 2003.

- [8] B. Anczykowski, D. Kruger, K. L. Babcock, and H. Fuchs, "Basic properties of dynamic force spectroscopy with scanning force microscope in experiment and simulation," *Ultramicroscopy*, vol. 66, pp. 251, 1996.
- [9] M. Marth, D. Maier, J. Honerkamp, R. Brandsch, and G. Bar, "A unifying view on some experimental effects in tapping-mode atomic force microscopy," *Journal of Applied Physics*, vol. 85 (10), pp. pp. 7030–7036, 1999.
- [10] S. I. Lee, S. W. Howell, A. Raman, and R. Reifenberger, "Nonlinear dynamics of microcantilevers in tapping mode atomic force microscopy: A comparison between theory and experiment," *Physical Review B*, vol. 66, pp. pp. 115409 (1–10), 2002.
- [11] D. R. Sahoo, A. Sebastian, and M. V. Salapaka, "Transient signal based sample detection in atomic force microscopy," *Applied Physics Letters*, vol. 83(26), pp. pp. 5521–5523, 2003.
- [12] A. Gannepalli, A. Sebastian, J. P. Cleveland, and M. V. Salapaka, "Thermal noise based control of tip-sample separation in atomic force microscopy," in *Proceedings of the American Control Conference*, MA, June 2004, Boston.
- [13] A. Sebastian, D. R. Sahoo, and M. V. Salapaka, "An observer based sample detection scheme for atomic force microscopy," in *Proceedings of the IEEE Conference on Decision and Control*, Hawaii, Dec 2003, USA.
- [14] G. Binnig, C.F. Quate, and C. Gerber, "Atomic force microscope," *Physical Review Letters*, vol. 56, no.9, pp. pp. 930–933., 1986.
- [15] R. Wiesendanger, *Scanning Probe Microscopy and Spectroscopy*, Cambridge University Press, 1998.
- [16] M. Ashhab, M. V. Salapaka, M. Dahleh, and I. Mezic, "Dynamical analysis and control of microcantilevers," *Automatica*, 1999.
- [17] N. A. Burnham, A. J. Kulik, G. Gremaud, and G. A. D. Briggs, "Nanosubharmonics: the dynamics of small nonlinear contacts," *Physics Review Letters*, vol. 74, pp. 5092–5059, 1995.

- [18] S. Salapaka, M. Dahleh, and I. Mezic, "On the dynamics of a harmonic oscillator undergoing impacts with a vibrating platform," *Nonlinear Dynamics*, vol. 24, pp. pp. 333–358, 2001.
- [19] A. Sebastian, M. V. Salapaka, D. J. Chen, and J. P. Cleveland, "Harmonic analysis based modeling of tapping-mode AFM," in *Proceedings of the American Control Conference*, California, June 1999, San Diego.
- [20] A. Sebastian, M. V. Salapaka, D. J. Chen, and J. P. Cleveland, "Harmonic and power balance tools for tapping-mode atomic force microscope," *Journal of Applied Physics*, vol. 89, no.11, pp. 6473–6480, 2001.
- [21] A. Sebastian and M. V. Salapaka, "Analysis of periodic solutions in tapping-mode AFM: An IQC approach," in *International symposium on Mathematical Theory of Networks and Systems*, South Bend, IN, August 2002.
- [22] A. Sebastian, S. Salapaka, and M. V. Salapaka, "Systems tools applied to micro-cantilever based devices," in *Multidisciplinary Research in Control*, LNCIS volume. Springer Verlag, New York, 2003.
- [23] A. Sebastian, A. Gannepalli, and M. V. Salapaka, "The amplitude phase dynamics and fixed points in tapping-mode atomic force microscopy," in *Proceedings of the American Control Conference*, MA, June 2004, Boston.
- [24] A. Megretski and A. Rantzer, "System analysis via integral quadratic constraints," *IEEE Transactions on Automatic Control*, vol. 47, no.6, pp. pp. 819–830., 1997.
- [25] H. K. Khalil, *Nonlinear Systems*, Prentice Hall, New Jersey, 2001.
- [26] V. A. Yakubovic, "The matrix-inequality method in the theory of the stability of nonlinear control systems," *Avtomatika i Telemekhanika*, vol. vol.25, no.7, pp. 1017–1029, 1964.
- [27] A. Megretski and A. Rantzer, "Harmonic analysis of nonlinear and uncertain systems," in *Proceedings of the American Control Conference*, Philadelphia, June 1998, Pennsylvania.

- [28] M. V. Salapaka, H. S. Bergh, J. Lai, A. Majumdar, and E. McFarland, "Multimode noise analysis of cantilevers for scanning probe microscopy," *Journal of Applied Physics*, vol. 81(6), pp. 2480–2487, 1997.
- [29] T. R. Rodriguez and R. Garcia, "Tip motion in amplitude modulation (tapping-mode) atomic-force microscopy: Comparison between continuous and point-mass models," *Applied Physics Letters*, vol. 80(9), pp. pp. 1646–1648, 2002.
- [30] U. Durig, "Extracting interaction forces and complementary observables in dynamic probe microscopy," *Applied Physics Letters*, vol. 76, no.9, pp. 1203–1205, 2000.
- [31] J. P. Cleveland, B. Anczykowski, A. E. Schmid, and V. B. Elings, "Energy dissipation in tapping-mode atomic force microscopy," *Applied Physics Letters*, vol. 72(20), pp. pp. 2613–2615, 1998.
- [32] D. G. Luenberger, *Optimization by Vector Space Methods*, John Wiley and Sons, New York, 1969.
- [33] L. Wang, "Analytical descriptions of the tapping-mode atomic force microscopy response," *Applied Physics Letters*, vol. 73 (25), pp. pp. 3781–3783, 1998.
- [34] M. Gauthier, N. Sasaki, and M. Tsukada, "Dynamics of the cantilever in noncontact dynamic force microscopy: The steady-state approximation and beyond," *Physical Review B*, vol. 64, pp. pp. 085409 (1–9), 2001.
- [35] A. San Paulo and R. Garcia, "Tip-surface forces, amplitude and energy dissipation in amplitude-modulation (tapping mode) force microscopy," *Physical Review B*, vol. 64, pp. pp. 041406 (1–4), 2002.
- [36] N. N. Bogoliubov and Y. A. Mitropolskii, *Asymptotic methods in the theory of non-linear oscillations*, Hindustan publishing corporation, New Delhi, India, 1961.
- [37] Y. A. Mitropolskii and N. Van Dao, *Applied asymptotic methods in non-linear oscillations*, Kluwer academic publishers, The Netherlands, 1997.
- [38] R. Koops and G.A. Sawatzky, "New scanning device for scanning tunneling microscope applications," *Review of Scientific Instruments*, vol. 63, no. 8, pp. 4008–9, August 1992.

- [39] H. Kaizuka, "Application of capacitor insertion method to scanning tunneling microscopes," *Review of Scientific Instruments*, vol. 60, no. 10, pp. 3119–3122, 1989.
- [40] R.C. Barrett and C.F. Quate, "Optical scan-correction system applied to atomic force microscopy," *Review of Scientific Instruments*, vol. 62, pp. 1393–1399, 1991.
- [41] D. Croft, G. Shedd, and S. Devasia, "Creep, hysteresis and vibration compensation for piezoactuators: Atomic force microscopy application," *Journal of Dynamic Systems, Measurement and Control*, vol. 123, pp. 35–43, 2001.
- [42] A. Daniele, S. Salapaka, M.V. Salapaka, and M. Dahleh, "Piezoelectric Scanners for Atomic Force Microscopes: Design of Lateral Sensors, Identification and Control," in *Proceedings of the American Control Conference, San Diego, California*, June 1999, pp. 253–257.
- [43] G. Schitter, P. Menold, H. F. Knapp, F. Allgower, and A. Stemmer, "High performance feedback for fast scanning atomic force microscopes," *Review of Scientific Instruments*, vol. 72, no. 8, pp. 3320–3327, August 2001.
- [44] S. Salapaka, A. Sebastian, J. P. Cleveland, and M. V. Salapaka, "High bandwidth nano-positioner: A robust control approach," *Review of Scientific Instruments*, vol. 73, no. 9, pp. 3232–3241, September 2002.
- [45] A. Sebastian and S. Salapaka, " \mathcal{H}_∞ loop shaping design for nanopositioning," in *Proceedings of the American Control Conference, Denver, Colorado*, June 2003.
- [46] A. Sebastian, J. P. Cleveland, and M. V. Salapaka, "Robust control approach to atomic force microscopy," in *Proceedings of the IEEE Conference on Decision and Control, Hawaii*, Dec 2003.
- [47] G.F. Franklin, J.D. Powell, and Emami-Naeni A., *Feedback Control of Dynamic Systems*, Addison-Wesley Publishing Company, 1986.
- [48] S. Skogestad and I. Postlethwaite, *Multivariable Feedback Control, Analysis and Design*, John Wiley and Sons, 1997.
- [49] M. Morari and E. Zafriou, *Robust Process Control*, Prentice-Hall, Englewood Cliffs, 1989.

- [50] K. Glover and D. McFarlane, "Robust stabilization of normalized coprime factor plant descriptions with \mathcal{H}_∞ -bounded uncertainty," *IEEE Transactions on Automatic Control*, vol. 34, no. 8, pp. 821–830, August 1989.
- [51] D. McFarlane and K. Glover, "A loop shaping design procedure using \mathcal{H}_∞ synthesis," *IEEE Transactions on Automatic Control*, vol. 37, no. 6, pp. 759–769, June 1992.
- [52] J. Sefton and K. Glover, "Pole/zero cancellations in the general \mathcal{H}_∞ problem with reference to a two block design," *Systems and Control Letters*, vol. 14, no. 4, 1990.
- [53] S. K. Mitra, *Digital Signal Processing: A computer based approach*, McGraw-Hill, 2nd edition edition, 1999.
- [54] M. C. Tsai, E. J. M. Geddes, and I. Postlethwaite, "Pole-zero cancellations and closed-loop properties of an \mathcal{H}_∞ mixed sensitivity design problem," *Automatica*, vol. 28, no. 3, pp. 519–530, 1992.
- [55] S. Salapaka and T. De, "A new sample-profile estimate for faster imaging in atomic force microscopy," in *Proceedings of the American Control Conference, Boston, MA*, June 2004.